Di-pion and di-electron production in quasi-free np reactions with HADES

Hubert Kuc

Université Paris-Sud

Ecole Doctorale 534 :
MODELISATION ET INSTRUMENTATION EN PHYSIQUE, ENERGIES, GEOSCIENCES ET ENVIRONNEMENT
Laboratoires: Institut de Physique Nucléaire Orsay
Smoluchowski Institute of Physics, Cracovie

Discipline : Physique

Thèse de doctorat

Soutenue le 18 Décembre 2014 par

Hubert Kuc

Di-pion and di-electron production in quasi-free np reactions with HADES

Directeurs de thèse :	Mme Béatrice RAMSTEIN	Institut de Physique Nucléaire (Orsay)
	M. Piotr Salabura	Université Jagellonne (Cracovie)

Composition du jury :

Président du jury :	M. Bachir MOUSSALLAM	Institut de Physique Nucléaire (Orsay)
Rapporteurs :	Mme Hélène FONVIEILLE	LPC (Clermont-Ferrand)
	M. Pawel MOSKAL	Université Jagellonne (Cracovie)
Examinateur :	M. Mikhail BASHKANOV	University of Tübingen

Contents

Chapter 1

Introduction

1.1 Introduction to strong interactions

1.1.1 Standard model

Strong interaction is one of the four fundamental interactions in nature: electromagnetic, weak, strong and gravitation. A description of these interactions, except the gravitation, is provided by the standard model. The principles of the model is the division of all elementary particles into three groups:

- leptons ($e^-\nu_e$, $\mu^-\nu_\mu$, $\tau^-\nu_\tau$ and their antiparticles)
- quarks (ud, cs, tb).
- and gauge bosons (W, Z, γ, g) mediating interactons

The leptons and quarks are grouped into 3 families according to their increasing masses, as indicated. The group of leptons consists of electron with its electron neutrino ($e^-\nu_e$), muon with corresponding neutrino ($\mu^-\nu_\mu$) and tauon with its tau neutrino ($\tau^-\nu_\tau$). There are antiparticles to every, above-mentioned leptons and quarks which have same masses but opposite charges.

Quarks can only be observed in certain combinations not as single particles. These combinations are called in general hadrons. Structures consisting of a quark and antiquark pair ($q\overline{q}$) are called mesons, while a combination of three quarks (qqq) is called a baryon. More complex quark systems like pentaquaks ($qqqq\overline{q}$) and di-baryons ($qqqqqq$) might also exist, although there is no unambiguous experimental signature. The search for particles consisting only of gluons (glueballs) or of a mixture of a ($q\overline{q}$) pair and gluons is also a very active field.

As mentioned above, quarks are divided in three main groups (up,down), (charm, strange) and (top, bottom). Quarks u, c and t have electric charge ($+2/3e$), while charge of the d, s and b is equal to ($-1/3e$). Every quark possess one of the three different possible colors: red, blue or green. This additional degree of freedom is the characteristic charge for strong interactions and the main rule is that the combination of all quarks within hadrons must be colorless. This means that, if we take into consideration the baryons, the three quarks must have different colors (red, green and blue). On the other hand, in mesons, if the quark has red color then the anti-quark must have anti-red color etc.. . The theory which describes the interactions between quarks and gluons is called the Quantum ChromoDynamics (QCD), where the Greek word "chroma" (meaning color) is applied to the theory of color charge dynamics. Due to a phenomenon known as color confinement,

and related to the very intense interaction at large distances, quarks are never directly observed or found isolated. This confinement leads to an ambiguous definition of the quark mass, namely the mass of the quarks can be defined either as a current or a constituent mass. The current mass is the mass of quarks extracted from gluon cloud, for up (u) is $\simeq 2.3$ MeV/c^2 and down (d) quark is $\simeq 4.8$ MeV/c^2. The masses of the next quarks rise very quickly: strange (s) $\simeq 95$ MeV/c^2, charm (c) $\simeq 1.27$ GeV/c^2, bottom (b) $\simeq 4.18$ GeV/c^2 and top (t) $\simeq 173$ GeV/c^2. These masses are generated via interactions with the Higgs Boson, recently discovered at LHC.

On the other hand, the constituent masses of quarks are determined from the mass of the hadrons. These are effective masses of quarks dresssed-up by virtual quark and gluon condensates appearing due to specific features of QCD. The constituent masses are always bigger than the current ones. More details about the origin of mass of the hadrons can be found in the next section of this chapter.

The last family of elementary particles is the group of gauge bosons. These are particles mediating interactions. To this group belongs massless gluons responsible for strong interactions between quarks, heavy W^+, W^-, Z^0 bosons mediating weak interactions and photons which are exchanged in electromagnetic interactions. Quantum gravitation theory expects the existence of the gravitons, which are responsible for the gravitation. Nevertheless gravitons were never observed due to the extremely small strength of this interaction.

1.1.2 The origin of hadron masses

The visible matter surrounding us consists of atoms. Over 99.94% of an atom's mass is concentrated in the nucleus which is composed of protons and neutrons. The mass of the nucleus is equal to the sum of its constituents, however binding energy between its components is strong enough to reduce the mass by a fraction of a percent. Protons and neutrons comprise three valence quarks uud and ddu, respectively. However the mass of the proton amounts to about ~ 1 GeV/c^2 which is ~ 100 times larger than the sum of the current masses of its valence quarks, $2 \cdot m_u + m_d \simeq 10$ MeV/c^2. The formation of massive protons out of almost massless quarks and gluons is a unique feature of QCD.

The issue of particle mass is strictly connected with chiral symmetry breaking. Chiral symmtery guarantees that for massles particles projection of the spin on the direction of motion ("handness") is not changed after interaction ; it will be either right-handed or left-handed. When comparing bare (current) quark masses to the proton mass, one can notice that indeed the masses of the up an down quarks are very small. Therefore, chiral symmetry can be treated as an approximate symmetry of the strong interaction. An introduction of non-zero quark mass to the QCD Lagrangian, called explicit symmetry breaking, has only a negligible impact [1].
Looking into the aforementioned difference between the u,d quarks and the proton mass, one concludes that chiral symmetry of the QCD Lagrangian is spontaneously broken in nature. The non zero expectation value of scalar quark-antiquark pairs ($< q\overline{q} >$ condensate) is the order parameter of the chiral symmetry breaking. Indeed, a left-handed quark q_L can be converted into a right-handed quark q_R by the interaction with a scalar $q\overline{q}$ pair. Due to the condensate, the chiral symmetry is spontaneously broken and hadron masses are determined by the existence of this chiral condensate $< q\overline{q} >$. Since the nucleon consists of three quarks, the quark mass should approximately be one third of the mass of the nucleon, i.e. about 300 MeV/c^2. Such quark states, which are dressed by a virtual

cloud of quark-antiquark pairs and gluons are also called constituent quarks. The mass of the quarks depends then on the distance over which it is probed by another quark. The shorter the distance between quarks, the weaker the interaction and the smaller the mass. Furthermore, predictions based on the Nambu-Jona-Lasino model [2] indicates that at higher nuclear densities and/or temperatures chiral symmetry can be partially restored due to a decrease of the amount of $q\bar{q}$ condensate (see Fig. 1.1, [3]). It has been proposed that this symmetry restoration can be observed in experiment as a reduction of the short-lived light vector mesons ρ, ω and ϕ in dense nuclear matter. On the other hand, calculations based on QCD sum rules indicate that the connection between the meson masses and the quark condensates is much more evolved. They relate energy weighted integral of the meson spectral function with series of quark and gluon condensates (also of higher order). Consequently, the QCD sum rules provide constraints on both the WIDTH and MASS of the meson at a given density, but do not fully answer the question about in-medium masses [4].

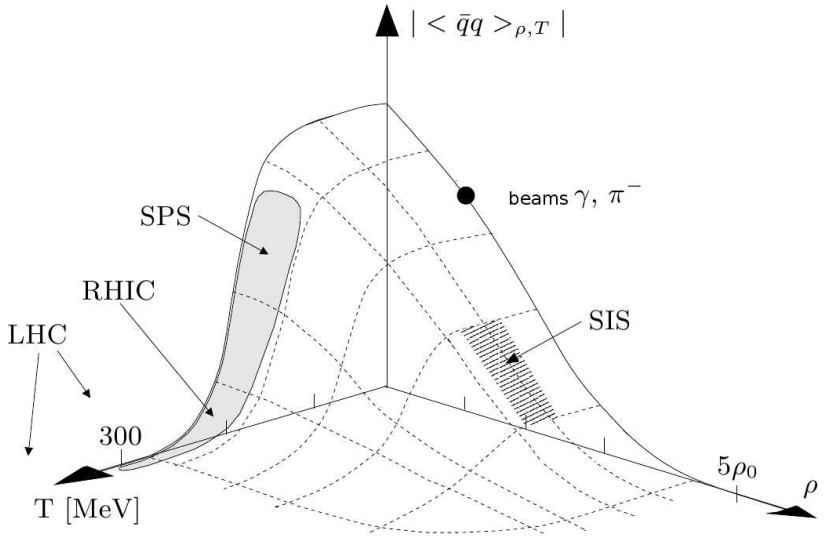

Figure 1.1: Value of two quark condensate as a function of the density and temperature, based on the NJL model [3].

1.1.3 The electromagnetic structure of hadrons

The common method of studying subatomic structures with electromagnetic probes dates back to the Rutherford experiment in which the atomic nucleus was discovered by the analysis of scattering α particles in Coulomb field of the heavy atoms. The differential cross section for the scattering of an electron by a particle with a specific spacial structure can be written in the form:

$$\frac{d\sigma}{d\mathbf{q^2}} = [\frac{d\sigma}{d\mathbf{q^2}}]_{point\ like}[F(\mathbf{q^2})]^{\mathbf{2}}, \tag{1.1}$$

where $\mathbf{q}$ is the momentum transferred to the electron. The function $F(\mathbf{q^2})$ is the form factor of a particle and describes the deviation of the differential cross section for the case of a point-like charge distribution. Since electrons are carrying a charge and spin the form factor has a electric and the magnetic contribution, respectively. The form factors gives an exhaustive characterization of the spatial distribution of the charge and the currents of an extended object.

Particle	Mass, MeV/c^2	Decay width, MeV/c^2	Lifetime, fm/c	Branching Ratio e^+e^-
ρ	769	152	1.3	4.44×10^{-5}
ω	783	8.43	23.4	7.07×10^{-5}
ϕ	1020	4.43	44.4	3.09×10^{-4}

Table 1.1: Properties of light vector mesons [5].

Particle interactions are commonly represented by Feynman diagrams (see Fig. 1.2). The arrows express the flow of conserved charges like the electric charge or color. Undetectable virtual particles are introduced to explain how energy and momentum are transferred during the reaction. Two interaction processes with an intermediate virtual photon are important in our context: electron-hadron scattering and electron-positron annihilation. Since the virtual photon exists for an exceedingly short time, there is, according to Heisenberg's uncertainty principle, a correspondingly large uncertainty in its energy. Within this uncertainty, momentum and energy need not balance each other. Therefore, the virtual photon can have nonzero mass during this short interaction period. In the relativistic description of particle scattering, it is convenient to use the 4-momentum transfer squared, defined as $q^2 = (\Delta E_e)^2 - (\Delta p_e)^2$. In case the virtual photon transfers essentially momentum but not energy ($q^2 < 0$), the messenger of the interaction is called space-like photons. The corresponding electromagnetic form factors for nucleons or pions can be obtained from e^-p, e^-n and $\pi^\pm e^-$ scattering experiments. Another method for producing virtual photons is particle-antiparticle annihilation (see Fig. 1.2). Annihilation experiments offer the possibility to study the form factor in the time-like region where the virtual photon has energy but no momentum. Annihilation and scattering experiments are complementary and allow to measure properties of hadronic states, in Time-Like and Space-Like regions respectively.

Figure 1.2: **Left**: Diagram for $e^+e^- \to \pi^+\pi^-$ annihilation; this process is caused by one-photon exchange in the time-like momentum-transfer region. The total cross section for the annihilation reaction is modified by the internal structure of the pions. **Right**: The same diagram for the one-photon exchange process in the VMD model.

The elementary particles are classified by the quantum numbers assigned to them. The neutral vector mesons have the same quantum numbers as the photon: spin 1 and negative parity ($J^P = 1^-$). Three light, neutral vector mesons are known, the ρ^0, the ω and ϕ meson, whose properties are presented in Table 1.1.

The first prediction that the vector mesons might exist were made by Y. Nambu in 1957. A particularly useful model of photon-hadron interactions, called the VMD (Vector Meson Dominance) model, was introduced by J.J. Sakurai in 1960 [6]. It essentially states, that energetic photons acquire a hadronic character by fluctuating into $q\bar{q}$ pairs with the quantum numbers of the photon, i.e. into neutral vector mesons. In this picture, the in-

teraction of a virtual photon with a hadron is mediated by a vector meson. This type of photon-hadron interaction is shown in Fig. 1.2 (right panel). The Gell-Mann and Zweig quark model based on flavour SU(3) symmetry predicts that the photon should behave as if it was composed of 75% ρ-meson, 8% ω-meson and 17% ϕ-meson. Thus, the ρ is the most important of the vector mesons in mediating photon-hadron interactions [7].

The cleanest method for studying the vector meson composition of the photon is e^+e^- annihilation into pions which isolates the production of vector mesons from other interactions. The annihilation of a positron and an electron into a virtual photon is purely electromagnetic and can be calculated with much confidence and precision using QED. The pion form factor in the time-like region predicted from Wilsonian matching [8] is in a good agreement with experimental data obtained from $e^+e^- \rightarrow \pi\pi$ measurements [9]. Experimental points are satisfactorily described by the ρ-meson excitation curve with $\rho-\omega$ interference taken into account. Detailed experimental data on the pion form factor in the time-like region permit a very accurate determination of the properties of the ρ-meson.

As discussed in previous section, it is expected that hadrons embedded in nuclear matter change their properties. Nuclear matter with increased density and temperature can be created in heavy ion collisions. In such reactions, nucleons are excited into baryonic resonance states (Δ, N*) which themselves decay by emission of mesons, particularly ρ. Hence, the presence of baryons may influence the vector meson spectral function in the medium. This is discussed in more details in next section.

1.1.4 In-medium modifications of ρ meson

At SIS18 energies in heavy ion collisions, a hadronic matter made of interacting mesons and baryonic resonances is formed [10]. Although quarks and gluons remain confined, sizeable modifications of the properties of hadrons are predicted [4]. Phenomenologically, these in-medium effects associated with the intermediate ρ meson can be classified according to the following extreme scenarios:

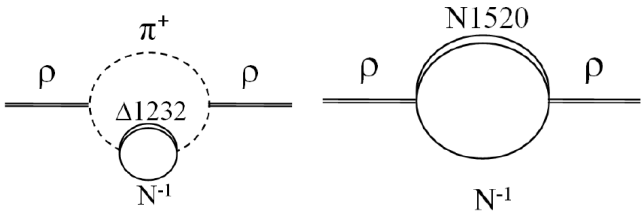

Figure 1.3: Dressing of the ρ in the nuclear medium by coupling to baryonic resonances. **Left**: $\Delta(1232)$-nucleon-hole polarization; **Right**: The modification of the ρ self-energy through its coupling to resonance-hole states.

- in a "dropping" mass scenario, the ρ mass essentially changes proportionally to changes of the quark condensate in the nuclear matter as a function of density and/or temperature, while the width is not affected. This model, introduced by Brown and Rho [11], is based on scale invariance of QCD and predicts scaling of the vector meson masses with density. It predicts a decrease of the vector meson masses of the order of 20% already at normal density.

- "broadening" of the ρ spectral function without substantial variations of the pole mass is predicted by hadronic models (e.g. Rapp, Wambach et al: [12]). In this scenario, a broadening of the ρ -meson mass comes from the interactions with the other hadrons present in the medium. However, the main effect comes from the excitation of baryon resonance-nucleon hole states (ΔN^{-1}, $N^* N^{-1}$; see Fig. 1.3) and the result is mainly a broadening of the spectral function with respect to the free meson (Fig. 1.4).

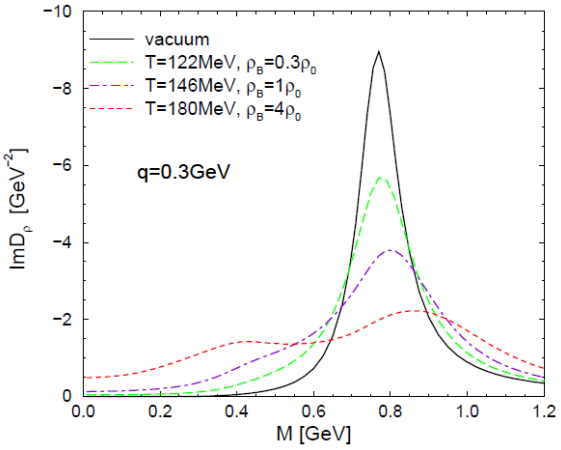

Figure 1.4: ρ -meson spectral function at fixed three-momentum q = 0.3 GeV in hot and dense hadronic matter at the temperatures and densities indicated in the figure (from Ref. [12]).

It is currently debated to which extend these effects are independent of each other and whether they are more driven by baryonic density or by temperature (i.e. pion density). Experimentally, one can address this question by comparing in-medium ρ -decay in cold and hot/dense matter as obtained in $p+A$ and $A+A$ collisions, respectively, at different energies. A review on experimental results can be found in ref. [4]. The experimental results indicate significant broadenning of the ρ meson and major role played by baryons.

1.1.5 Dilepton probes

Direct detection of the vector mesons is not possible due to their short life time (see table 1.1). On the other hand, considering heavy ion collisions such a short life time is an advantage since these particles decay still inside the nuclear fireball formed in the collision. Meson reconstruction is based on reconstruction of the invariant mass distribution of the decaying mother particle from the momentum vectors of identified decay products. Kaonic or pionic decay channels are characterises by high branching ratios (BR of the order of tens of %), however decay products interact strongly with the medium loosing information about its source. This problem does not exist in leptonic decay channels (here e^+e^-) which do not interact strongly and thus carry undistorted information about the source into the detector.

Dileptons, however, are a very rare probe. While the production of real photons is suppressed relative to hadrons by about one power of the electromagnetic coupling constant, $\alpha = 1/137$, dilepton emission (i.e. virtual photons with subsequent decay $\gamma^* \rightarrow e^+e^-$) is further suppressed by an additional power of α. The branching ratios for hadronic decays of vector mesons are thus typically 4 orders of magnitude larger than for dilepton decays,

unless they are suppressed by phase space factors. The measurement is additionally complicated by combinatorial background originating from neutral pion decays. Method of removing di-electron pairs coming from different sources is described in chapter 3 concerning the data analysis methods.

In the 1-2 AGeV energy range, the main di-electron sources can be separated into following sources:

- The vector meson decays (see table 1.1)
- The Dalitz decay of mesons:
  - $\pi^0 \rightarrow \gamma e^+ e^-$ with branching ratio 1.2%.
  - $\eta \rightarrow \gamma e^+ e^-$ with branching ratio $7 \cdot 10^{-3}$.
  - $\omega \rightarrow \pi^0 e^+ e^-$ with branching ratio $8 \cdot 10^{-4}$.
- The Dalitz decay of baryonic resonances:
  - $\Delta \rightarrow N e^+ e^-$ with branching ratio $4.2 \cdot 10^{-5}$.
  - $N^*(1535), N^*(1520), .. \rightarrow N e^+ e^-$,
- The nucleon-nucleon bremsstrahlung: $NN \rightarrow NN e^+ e^-$.

1.2 Results from the HADES experiment

1.2.1 General motivations

One of the central topics of contemporary hadron physics is the investigation of hadronic matter under extreme conditions. Theoretical models based on non-perturbative Quantum Chromo-Dynamics indicate that the properties of hadrons are modified, if they are embedded in a strongly interacting medium. The High-Acceptance DiElectron Spectrometer[13] (HADES) in operation at the GSI Helmholtzzentrum für Schwerionenforschung has been specifically designed to study medium modifications of the light vector mesons ρ, ω, ϕ. Experimentally, these probes are well suited for two reasons. The vector mesons are short-lived with lifetimes comparable to the duration of the compression phase of heavy-ion reactions. In particular, in the 1 to 2 AGeV regime of the heavy-ion synchrotron SIS18, the average life time of the fireball created in Au+Au collisions is in the order of 10-15 fm/c. Equally important is their electromagnetic decay branch into e^+e^- pairs. The e^+e^- channel is not subject to strong final state interaction and thus provides an undistorted signal of the matter phase. The goal of the HADES experiments is to measure the spectral properties of the vector mesons such as their in-medium masses and widths.

The HADES heavy-ion program is focused on incident kinetic energies from 1 to 3.5 AGeV. One specific aspect of heavy-ion reactions in this energy range is the important role played by the baryonic resonances, which propagate and are regenerated (i.e $\Delta N \rightarrow NN\pi \rightarrow \Delta N$ due to the long life-time of the dense hadronic matter phase. A detailed description of the resonance excitation and their subsequent decays to pseudo-scalar and vector mesons is important for the interpretation of the di-electron spectra in this energy regime. In order to study more selectively these contributions, the HADES program also comprises elementary reactions (pp and quasi-free np) which are used as a reference to the heavy ion experiments.

1.2.2 Results from nucleon-nucleon collisions

The special character of e^+e^- production in the HADES energy regime is related to the strong contribution of baryonic sources [14]: Dalitz decays of nucleon resonances $R \rightarrow Ne^+e^-$ (mainly $\Delta(1232)$) and NN bremsstrahlung, and strongly rising excitation function of the η meson production [15]. The baryonic sources completely determine the e^+e^- invariant mass distribution above the π^0 mass at beam energies below η meson production threshold (E^{thr}_{beam}= 1.257 GeV) [16]. The latter contributes via its Dalitz decay channel at the same level as baryonic sources already beam kinetic energies of 1.6 GeV. The vector meson production is small because of the high production threshold (E^{thr}_{beam}= 1.88 GeV for ω) and adds an important contribution to the invariant mass spectrum at $M_{e^+e^-} > 0.6$ GeV/c^2. While the exclusive ω and η production in $p+p$ reactions close to the threshold is very well known, the data on ρ are scarce. Furthermore, in contrast to the ω and ϕ production mechanisms, which essentially do not show any strong resonance contributions, a strong coupling of the ρ meson to the low-mass baryonic resonances ($D_{13}(1520)$, $P_{13}(1720)$,...) has been predicted (see for example [17, 18]). Since the ρ meson is a broad resonance, these couplings lead to a spectral function very different from a simple Breit-Wigner distribution even in elementary reactions. One should underline that a detailed understanding of the resonance decays into ρ meson and related resonance-meson coupling mechanism is a prerequisite for any conclusions on in-medium mass modifications in nuclear matter. One should also stress that decay processes like $R \rightarrow Ne^+e^-$ (Dalitz) and $R \rightarrow \rho(\rightarrow e^+e^-)N$ should not be in general treated as a two separate decay channels. A natural connection should be provided by a structure of the electromagnetic transition form factors in time-like region, i.e its dependence on the virtual photon (or e^+e^-) mass. Calculations performed within the extended Vector Meson Dominance (VMD) model [19] indeed show the importance of the vector mesons in such transitions. However, new precise data from proton and in particular, pion induced reactions on such decays are needed to provide more constraints for calculations.

The other silent feature of the di-electron production in NN reactions in this energy range is a very strong isospin dependence. This feature was already demonstrated by DLS experiment [20] measuring excitation functions of the pair production in $p+p$ and $d+p$ collisions in the beam energy range $E_{beam} = 1-4$ GeV.

Though the statistics gathered in these experiments is limited and the systematic errors related to the normalization are large, a strong increase of the non-trivial pair yield (in $M_{e^+e^-} > M_{\pi^0}$ range) can be observed in $d+p$ reactions over the one measured in $p+p$ below beam energy of 2 GeV, with maximum around $E = 1.25$ GeV. The new data obtained by HADES stimulated a significant progress in the understanding of this phenomenon. Fig. 1.5 shows the e^+e^- invariant mass distributions obtained in $p+p$ and, for the first time, in quasi-free $n+p$ reactions, the latter one selected by tagging the proton spectator from $d+p$ collisions, at E_{beam}=1.25 GeV. While the $p+p$ data can be described rather well by the incoherent superposition of the π^0 and $\Delta(1232)$ Dalitz decays, the $p+n$ data shows a large excess over these two contributions at $M_{e^+e^-} > M_{\pi^0}$. The situation is not changed by adding a small η contribution in the $p+n$ case, appearing because of the finite neutron momentum distribution inside the deuteron. The latter effect is very well constrained by the known η meson production cross section and nucleon momentum distribution inside the deuteron (see for details [15]).

The important challenges in studying baryonic electromagnetic transitions are the relevant electromagnetic transition form-factors and the treatment of the non-resonant contributions. The shaded area shows the uncertainty related to the form-factor of the

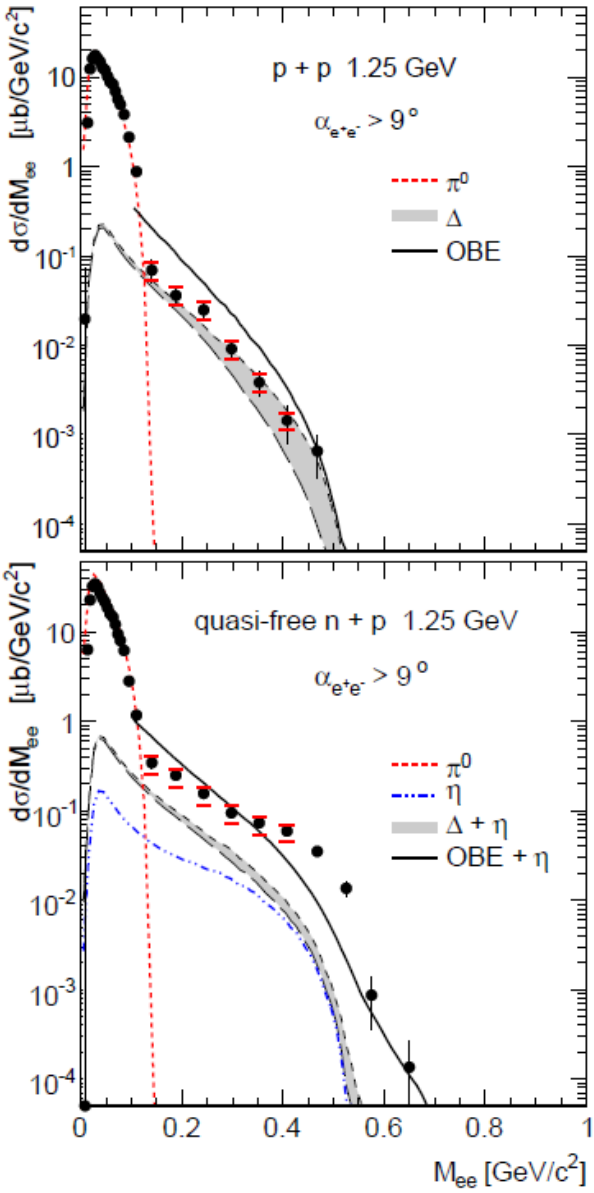

Figure 1.5: Electron pair differential cross section as a function of invariant mass (full circles) measured in $p + p$ reactions (upper panel) and quasi-free $n + p$ reactions (lower panel) at 1.25 GeV. Systematic errors indicated by (red) horizontal bars, statistical errors by vertical bars. Expected contributions from π^0, $\Delta(1232)$ and η Dalitz decays obtained by PLUTO event generator are shown separately [15]. Solid curves show predictions from One Boson Exchange Model [21].

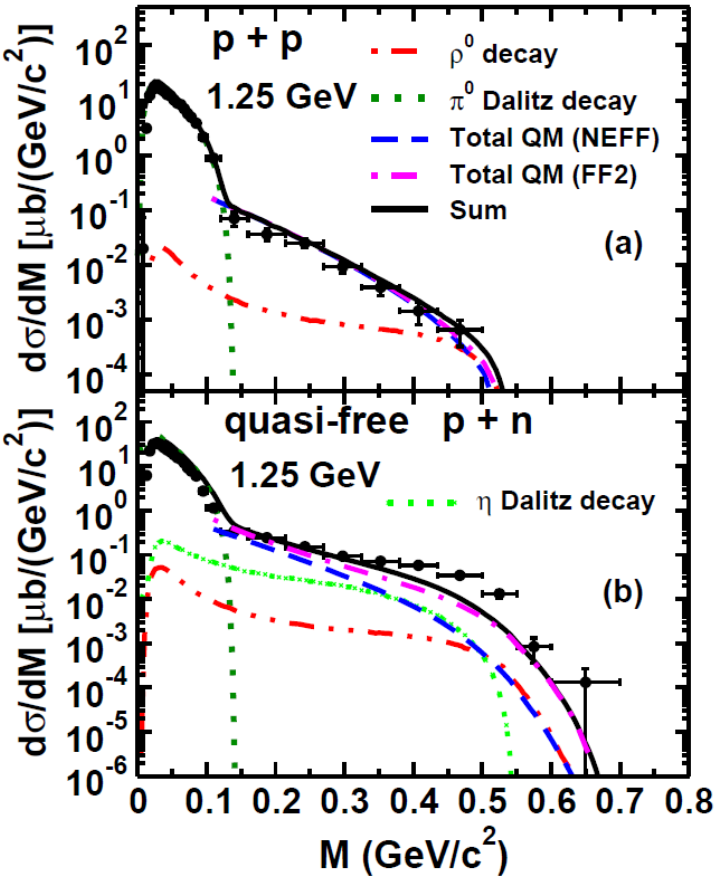

Figure 1.6: Experimental data (same as in Fig. 1.5) compared to the One Boson model [22]. Results without (NEFF) and with (FF2) incorporation of the electromagnetic form factor of charged pions are shown speparately. Solid curves show sum of these contributions with the subthreshold ρ production.

$\Delta(1232) \rightarrow Ne^+e^-$ decay calculated here within the two-component (direct and VDM electromagnetic couplings) model [23]. The solid curve shows predictions of [21] based on One-Boson Exchange model taking into account the coherent sum of resonant ($\Delta(1232)$) and non-resonant (so called "quasi- elastic" bremsstrahlung) contributions [21]. In Fig. 1.6 recent results of OBE calculations [22] are compared to HADES data. Obviously, these calculations provide a better description of data. In particular, the very diferent shape of the $p + n$ data is better accounted for, due to the incorporation of the electromagnetic form factor of the charged pion. This contribution is possible since, in contrast to the $p+p$ reaction, a charged pion can be exchanged. Although, the theoretical description of the $p + n$ data is not yet finally settled, the data allow to construct, together with the $p + p$ data, the $N + N$ reference spectrum, which can be used in heavy-ion reactions to search for in-medium effects.

1.2.3 Results from nucleus-nucleus collisions

In the $1 - 2$ AGeV energy range, particle production in heavy-ion collisions [14] is dominated by pion production which originates mainly from the $\Delta(1232)$ resonance [16]. Multiplicities of heavier mesons, mainly η, are already very low (of order $1 - 2\%$). Production multiplicities for π^0 and η mesons are known from their decay into real photons from former TAPS measurements at GSI [26]. They provide an important constraint on

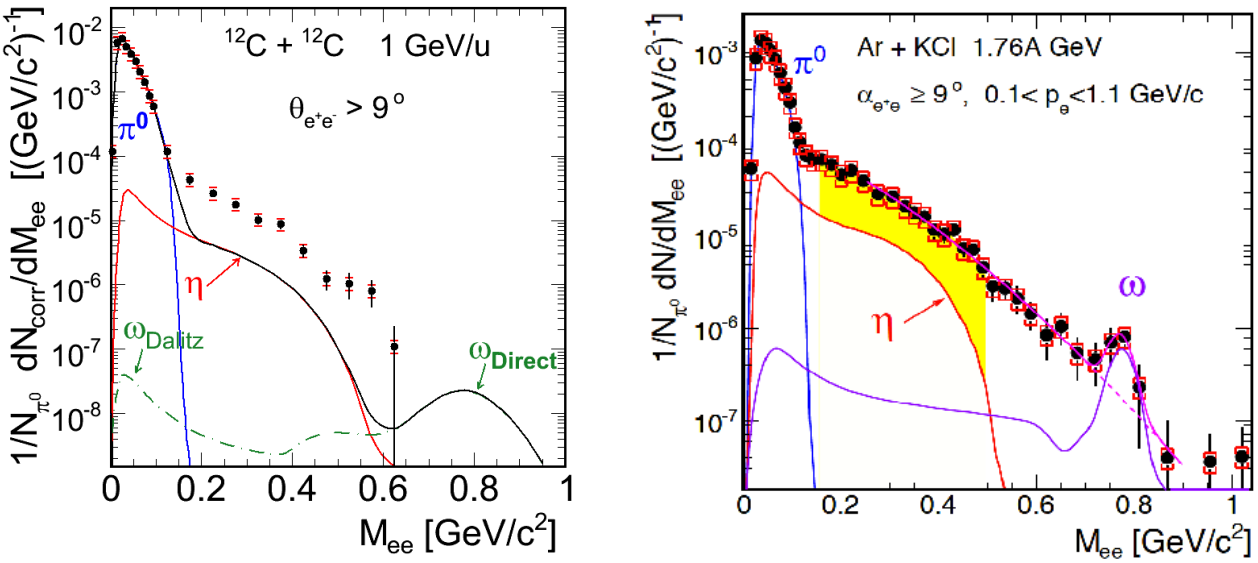

Figure 1.7: **Left**: e^+e^- production rates normalized to π^0 yield as function of the invariant-masses distribution measured in C+C collisions at 1 AGeV compared to thermal dielectron cocktail of mesonic sources (π^0, η, ω) after freeze-out [24]. **Right**: Similar distributions but obtained for $Ar + KCl$ collisions at 1.756 AGeV [25] Shaded area shows invariant mass region where the pair excess from in-medium radiation has been identified. Different widths of ω peak in simulated cocktails accounts for different mass resolution in both experiments.

e^+e^- contributions resulting from these mesons Dalitz decays.

The dielectron invariant-mass distributions measured with HADES in light C+C (at 1 AGeV) [24] and the medium-heavy $Ar + KCl$ (at 1.75 AGeV) [25] systems are shown in Fig. 1.7. The spectra are normalized to the mean of charged pion (π^+, π^-) yields, measured independently by HADES, and extrapolated to the full solid angle. At this energy and for these collision systems, it is a good measure of neutral pion multiplicity. The differential distributions obtained in such a way are compared to the expected mesonic e^+e^- cocktail from π^0, η Dalitz and ω decays according to the measured (for π^0 and η) and extrapolated (from the m_T scaling for ω) multiplicities. Sum of these distributions accounts from long-lived sources and accounts for the e^+e^- emission after the freeze-out.

One should underline that the ω peak visible in the invariant mass distribution in $Ar + KCl$ collisions is the first measurement of the meson production at such a low energy (below its free N-N threshold). As one can see, the e^+e^- cocktail composed from the meson decays does not explain the measured yields for both collision systems and leave room for a contribution expected from the baryonic sources discussed above: resonance Dalitz decays (mainly $\Delta(1232)$) and nucleon-nucleon bremsstrahlung. This conclusion is also supported by our analysis of the shape of excitation function of the missing contribution that appears to be very similar to the one measured for pions, governed by $\Delta(1232)$ creation, but very different from the one established for the η meson [25].

In order to search for true in-medium radiation off the dense nuclear phase of collisions, e^+e^- production rates found in nucleus-nucleus reactions has to be compared with a proper superposition of the production rates measured in elementary collisions. For this purpose the ratio of the pair multiplicities measured in A-A collisions from Fig. 1.7 to the average $1/2(M_{pp}^{e^+e^-} + M_{np}^{e^+e^-})/M_{\pi^0}$ obtained from the e^+e^- (see Fig. 1.5) and the π^0 cross sections

measured in NN collisions are presented on Fig. 1.8. One should mention that, before computing these ratios, the contribution of the respective η Dalitz decays were subtracted, due to the very steep excitation function of the η meson. The normalization to the M_{π^0} takes into account the beam energy dependence of the baryonic sources discussed above and also the dependence of particle production on system-size via scaling with an average number of participants A_{part}, which holds at SIS18 energy range (for details see [25]).

As one can see, all distributions agree in the π^0 mass range, which confirms the normalization procedure. Furthermore, the ratio is consistent, within statistical and systematic errors, with the one for the $C+C$ collisions at 1 and 2 AGeV. It means that indeed, pair production in the mass range $M_{e^+e^-} < 0.6$ GeV/c^2 in $C+C$ collisions can be described as the sum of contributions stemming from (i) baryonic resonances, extracted from $N+N$ collisions, which yield scales as pion production and (ii) the η, π^0 meson accounting for the radiation after freeze-out. This observation explains the long standing "DLS puzzle" [27] of the unexplained yield measured in $C+C$ collisions by not correctly accounted baryonic contributions in $p-n$ reactions. In this context, it should be emphasized that the DLS and HADES data agree within errors bars as shown by a dedicated analysis [24].

A significant excess $(2.5-3)$ with respect to the $N+N$ reference is visible for the $Ar+KCl$ system above the π^0 mass, signalling an additional contribution from the dense phase of the heavy ion collision. This means that going to the larger collision system $Ar+KCl$ a stronger than linear scaling of the pair production with A_{part} is observed. This observation can be interpreted as a signature of the onset of a contribution of multi-body and multi-step processes in the dense phase created in collisions of nuclei of sufficiently large size. In this context, the propagation and regeneration of short -lived baryonic resonances seems to play a main role. The penetrating nature of the dilepton probe allows to observe an effect of "shining" of this baryonic matter also from multi-collision steps integrated over the whole collision time. In contrast, pions observed in the detector are emerging only from the freeze-out time. A further important test of this scenario will be provided by the collisions of heavier system $Au+Au$ at 1.25 AGeV also collected by HADES.

1.2.4 Double-pion production in elementary collisions

In previous sections, it has been shown that dilepton production from processes involving baryons play a very important role in 1-2 AGeV energy range. In particular, a strong isospin dependence has been observed leading to an excess of e^+e^- yield at $M_{e^+e^-} > M_{\pi 0}$ in $p+n$ over the one measured in $p+p$.

The HADES spectrometer was designed for detection of the dielectron probes with high accuracy and high acceptance. However, the detector is also suited for charged hadron (π^+, π^-, K^+, K^-, p) detection. The possibility to measure simultaneously di-electrons and pion production with HADES is a great advantage, since pion production allows to constrain the hadronic cocktail used to describe the dilepton production. More generally, these complementary data provide quantitative information on hadronic interactions, as well as resonance excitations and resonance properties.
For instance, one and double-pion production in nucleon-nucleon collisions is of particular interest for studies of excitation of the baryon resonances [28, 29, 30]. The $\pi+\pi-$ production channel is particularly interesting for studies of ρ meson production. A number of low statistic experiments on pion production in NN interactions has been performed

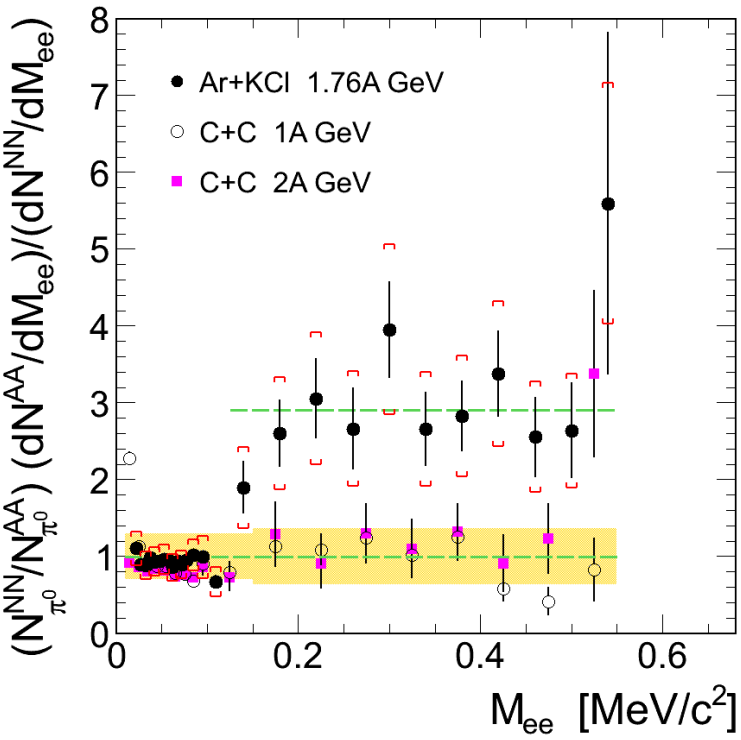

Figure 1.8: Ratio of e^+e^- invariant mass distributions measured in $Ar + KCl$ and $C + C$ with subtracted η meson contribution to the $N + N$ reference spectrum, obtained as described in text. Total errors, statistical and systematic are added quadratically and indicated by the shaded band [25]

in the past spanning the energy region from the threshold to a few GeV's by using bubble chamber techniques. The bulk of the experimental data originate from pp collision. In contrast the data on np interaction in the low and medium energy regions are scare. Recently, double-pion production in NN collisions has been accurately measured at CELSIUS [31], COSY [32], KEK [33] facilities. The differential cross section for $pp \to pp\pi^+\pi^-$ and $pp \to pp\pi^0\pi^0$ reactions have been obtained at CELSIUS and COSY for the beam energies from the threshold up to 1.4 GeV [31, 32]. The total cross section of $pn \to pn\pi^+\pi^-$ and $pn \to pp\pi^-\pi^0$ channels have been measured at KEK in the beam energy range from 0.698 GeV up to 1.172 GeV [33]. Very recently, the WASA collaboration also measured the quasi-free $pn \to pp\pi^0\pi^-$ [34] $pn \to pp\pi^0\pi^-$ [35].

On the theoretical side, the double pion production in NN collisions has been the subject of many investigations. The effective Lagrangian models (Valencia [36], XuCao [37] and modified Valencia [38]) predict that at energies near threshold the $\pi\pi$ production is dominated by the excitation of one of the nucleons into the Roper resonance $N^*(1440)P11$ via σ-exchange. At higher energies, the double $\Delta(1232)$ excitation is expected to be the dominant reaction mechanism for $\pi\pi$ production. The OPER model [39] based on the exchange of reggeized π have been successfully used to describe bubble chamber data on $np \to np\pi^+\pi^-$ reaction at momenta above 3 GeV/c. This model can be applied for description of $np \to np\pi^+\pi^-$ reaction at the momenta below 3 GeV/c by taking into account the mechanism of one baryon exchange (OBE).

The $pp \to pp\pi^0\pi^0$ reaction was intensively studied by the WASA collaboration. Modifications to the Valencia model have been proposed in so called modfied Valenica model

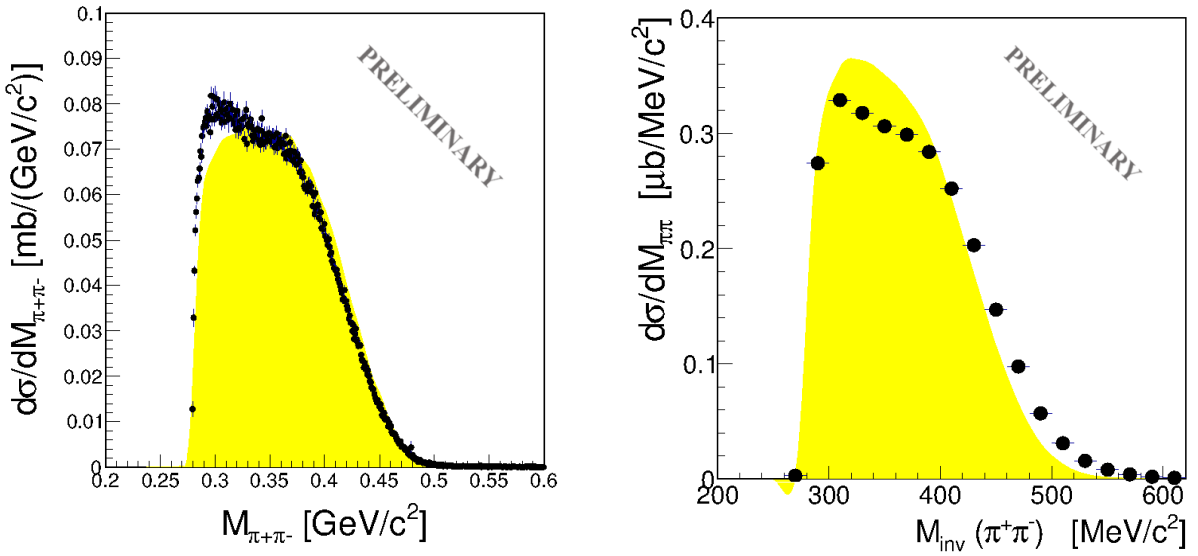

Figure 1.9: Differential cross section of $\pi^+\pi^-$ production as a function of invariant mass from $pp \to pp\pi^+\pi^-$ (**Left**) and $pn \to pn\pi^+\pi^-$ (**Right**) exclusive channels. Black points represent experimental data, the yellow region shows distributions expected from phase space simulation normalized to the integrated experimental yield. Presented data are inside the HADES acceptance.

[38], which allows for a good description of the differential spectra measured by WASA.

The HADES collaboration also started a study of $\pi^+\pi^-$ production in pp and np collisions. The measured differential distributions are compared to predictions from the different models [36, 39, 37, 38], which were briefly described above. The analysis is still on-going, but the preliminary results show that the modified Valencia model provides the best description of the data, hence confirming the WASA analysis. Figure 1.9 presents experimental distributions of the di-pion invariant mass from *pp* and *np* experiments inside HADES acceptance in comparison to simulation assuming pion production with uniform phase-space distributions. The data have been converted to cross sections by means of the elastic $pp \to pp$ yield measured in the same experiment. For this analysis, the detection of all charged particles in the HADES detector has been requested (exlusive analysis). The exclusive analysis of the two-pion production with a deuteron in final state deserves a separate discussion because of the so called "ABC effect". This topic will be addressed in the next section of this chapter together with recent results from $d\pi\pi$ of the WASA collaboration.

1.3 Motivations for the study of the $pn \to d\pi^+\pi^-$ channel with HADES

1.3.1 History of the "ABC effect"

The history of the "ABC" is dated back to 1960, when a paper of Alexander Abashin, Norman E. Both and Kenneth M. Crowe [40] presented results on cross sections of $pd \to {}^3He + X$ reaction obtained with single arm magnetic spectrometer in Berkeley. The cross sections were measured for four beam energies (624 MeV, 648 MeV, 695 MeV, 743 MeV), at a single polar angle of 11.7°. The mass of the X system was reconstructed

from the measured momentum of ^3He. Figure 1.10 shows the reaction cross section, for one of the energies, as a function of the missing mass. The spectrum shows an unexpected enhancement, placed just at the two-pion threshold.

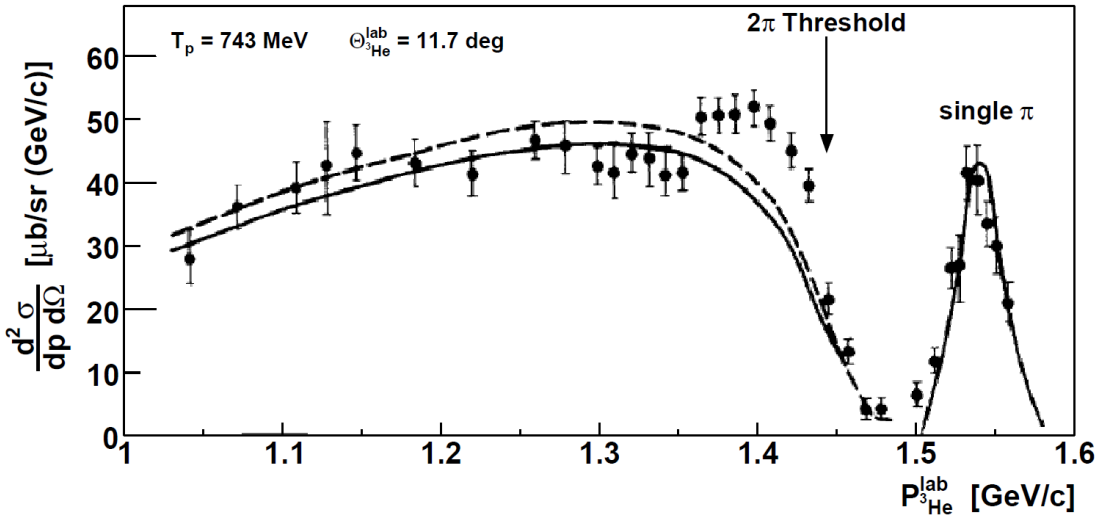

Figure 1.10: First results on the ABC effect in the reaction $pd \to {}^3He + X$ [40]. The solid and dashed lines correspond to calculations according to uniform phase space distributions with different normalizations, the strong peak at the right is single pion production. The enhancement with respect to phase space around 1.4 GeV/c is the so-called ABC effect.

These results were confirmed by other groups with similar experiments in Birmingham and Saclay [41, 42, 43, 44, 45]. All these experiments measured in the energy range around $150 - 400 MeV$ above the $\pi\pi$ threshold. The common feature of these measurements was the reconstruction of the missing mass in inclusive measurements with the production of a heavy ejectile (d,^{3}He ,^{4}He.,...). Hence there was no way to distinguish between 2π, 3π and even η production channels. Nevertheless, in all cases, an enhancement around 2π threshold was observed if the X system was electrically neutral and isoscalar.

A first suggestion to explain the effect was a strong $\pi\pi$ interaction leading to the formation of a new meson. However, the deduced s-wave $\pi\pi$ scattering length of $a_s = 2.4$ fm was an order of magnitude larger than the one obtained from the channels with unbound nucleons in the final state. Later, the t-channel $\Delta\Delta$ production was proposed to be responsible for the apparent enhancement at low di-pion invariant masses. After the pionic decay of the Δ resonances, the nucleon fuse together forming a deuteron. The Feynman diagram for this process is presented in Fig. 1.11.

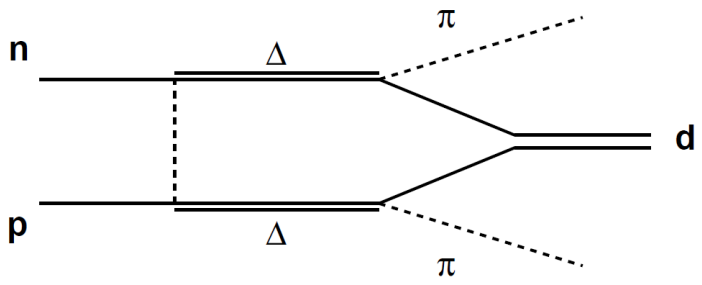

Figure 1.11: Feynman diagram of the t-channel $\Delta\Delta$ model for the ABC effect in the reaction $pn \to d\pi\pi$

In 1973, Risser and Shuster calculated [46] that in the case of the double delta decay channel followed by formation of a bound nuclear system, there are two preferred configurations which leads to an enhancement at low and high di-pion invariant masses. The first one corresponds to pions flying in the same direction, hence with a low relative momentum (enhancement at low invariant masses). Second preferred configuration is when pions move back-to-back (high relative momentum), which create high 2π invariant masses. Furthermore, at center of mass energies ($\sqrt{s}$) below the double delta pole mass, the low-mass peak should be preferred. These calculations described the inclusive data on a qualitative level.
Exclusive measurements of the ABC effect were performed for the first time by the CELSIUS-WASA collaboration at Uppsala. In 2005, measurements on the fusion of pd to ^3He in both the $\pi^0\pi^0$ and the $\pi^+\pi^-$ channel were performed [47]. Results were rather unexpected: The enhancement occured only at low 2π mass, not at higher masses. Next, in 2005, the "golden" ABC reaction $pn(p_{spec}) \rightarrow d(p_{spec}) + \pi\pi$ [48] was investigated. Results from this experiment, performed at five different energies, confirmed the bump at low $\pi\pi$ invariant masses, furthermore, the energy dependence of the total cross section was measured and a narrow peak appeared. The observed peak could not be explained by any existing model. In 2008, after WASA was moved to the COSY facility, the same reaction was measured with much better statistics at several different energies and the same peak was seen (fig. 1.12).

1.3.2 Recent WASA studies of the "ABC effect" and signs of possible di-baryon resonance

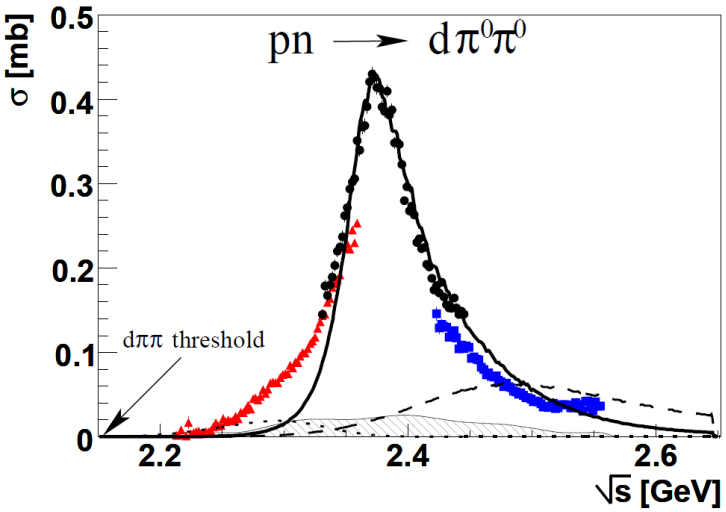

Figure 1.12: Total cross sections obtained from experiment on $pd \rightarrow d\pi^0\pi^0 + p_{spectator}$ for the beam energies $T_p = 1.0$ GeV (triangles), 1.2 GeV (dots) and 1.4 GeV (squares) normalized independently. The hatched area indicates systematic uncertainties. The drawn lines represent the expected cross sections for the Roper excitation process (dotted) and the t-channel $\Delta\Delta$ contribution (dashed) as well as a calculation for a s-channel resonance with $m = 2.37$ GeV and $\Gamma = 68$ MeV (solid) [49].

In order to investigate the unexpected results from two-pion production in a comprehensive way, the WASA collaboration measured the isoscalar double-pionic fusion process $pn \rightarrow d\pi^0\pi^0$ exclusively [49] over the almost complete phase space with one order of magnitude higher statistics than previously at CELSIUS. The experiment was carried out at

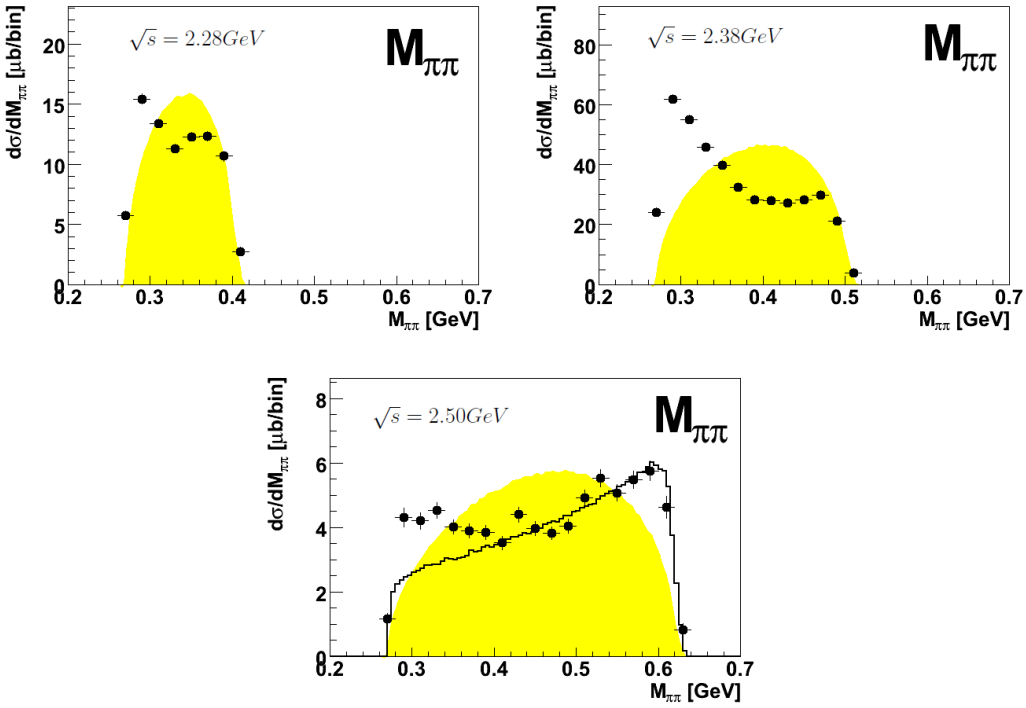

Figure 1.13: $M_{\pi^0\pi^0}$ distribution at three different $\sqrt{s}$ regions. **Top left:** $\sqrt{s} = 2.28$ GeV; **Top Right:** $\sqrt{s} = 2.38$ GeV (i.e. peak maximum); **Bottom:** $\sqrt{s} = 2.5$ GeV. The solid black line on the bottom picture represents t-channel $\Delta\Delta$ prediction. Black points in all pictures stands for experimental data and the yellow area represents phase-space simulations [50].

the COSY facility via the reaction $pd \to d\pi^0\pi^0 + p_{spectator}$. Due to the finite momentum distribution of the nucleons in the target deuteron, three different energies of the proton beam were sufficient to scan center of mass energies in the range 2.22 GeV $< \sqrt{s} <$ 2.56 GeV. Results are presented on the figures 1.12 and 1.13.

Fig. 1.12 shows the energy dependence of the total cross section. It exhibits a very pronounced Lorentzian shaped energy distribution reminiscent of a resonance. The width of this structure is four times smaller than that of a conventional $\Delta\Delta$ excitation process with a width of about $2\Gamma_\Delta$. Also, the peak cross section is about $80MeV$ below the mass of $2\Delta s$. The conventional sources contributing in this energy range are only the t-channel $\Delta\Delta$ process and the $N^*(1440)$ (Roper) excitation. The cross section for the $\Delta\Delta$, derived by the isospin relations from the known $pp \to d\pi^+\pi^0$, is presented on the picture as a dotted line and for the Roper excitation as a dashed line. Although there might be other, non-resonant contributions of relevance, it seems that conventional processes contributing to $pn \to d\pi^0\pi^0$ are much smaller in magnitude, but also at variance with the energy dependence of the data.

On the Fig. 1.13, the two-pion invariant mass is presented, corresponding to three different $\sqrt{s}$ regions. This plot shows that a large enhancement at low di-pion masses, close to the kinematic limit, is associated to the resonance peak. Data points are compared with the results of phase-space simulation (yellow shaded area) normalized to the same area. On the last (bottom) plot the results of calculations with a model assuming double Δ excitation is presented to illustrate the origin of the bump at high invariant masses.

In order to explain the obtained results, it was proposed that the two Δ resonances may be attracting each other and even forming a bound state. This would suppress the

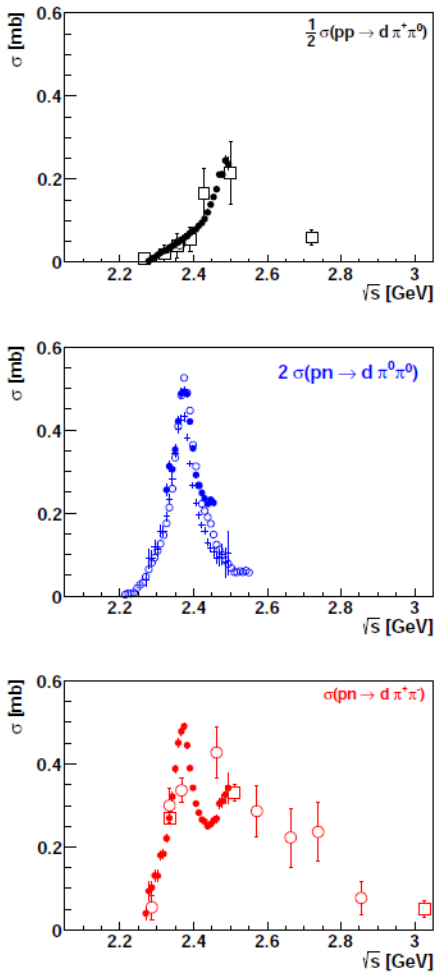

Figure 1.14: Total cross sections [51] of the basic double-pionic fusion reactions pN→dππ of different isopsin systems measured by WASA (full symbols) in comparison with older data (empty symbols). The crosses denote the cross sections for the $pn \to d\pi^0\pi^0$ calculated using the isospin relation in Eq. 1.2 .

configurations responsible for the high di-pion masses. The resonance-like structure in the total cross section of the *pn* data further supports the idea of a ΔΔ bound state with isospin 0. If true, this could possibly be the first solid evidence for a dibaryonic resonance - a true 6-quark state in contrast to a molecule-like object such as the deuteron. This interpretation needs, however, further profound theoretical and experimental investigations. The reaction channel $pn \to d\pi^0\pi^0$ is the most prominent, since the deuteron is in the isospin 0 and the two pions are also in a pure isospin 0 state. The pn pair is therefore also in a pure isospin 0 state. However, the resonance should be also observed in other channels, like $pn \to d\pi^+\pi^-$, which is an admixture of the isospin 0 and isospin 1 states and should be absent from pure isospin 1 states, like $pp \to d\pi^+\pi^0$. Results obtained by the WASA collaboration [51] for these different channels are displayed in fig. 1.14. As expected, no resonant structure is observed in the case of the pure isospin $I = 1$ channel, while it can be seen in the case of $pn \to d\pi^+\pi^-$.

An important consistency check of the cross sections measured in the different channels was made using the following relation, which is driven by the isospin coefficients in the

different channels:

$$\sigma[pn \to d\pi^+\pi^-] = \frac{1}{2}\underbrace{\sigma[pp \to d\pi^+\pi^0]}_{I=1} + 2\underbrace{\sigma[pn \to d\pi^0\pi^0]}_{I=0} \tag{1.2}$$

1.3.3 Interest of the HADES measurement

The main goal of the dipion analysis presented in this PhD is to compare HADES results from the quasi-free $np \to d\pi^+\pi^-$ reaction measured at a deuteron incident energy 2.5 GeV to the one obtained by WASA in the same energy range to provide an independent check of the interpretation based on the dibaryon resonance. As it will be discussed, our measurement covers phase space region not covered by WASA. Results of this analysis also complement data on $pp \to pp\pi^+\pi^-$ and $np \to np\pi^+\pi^-$ channels obtained in complementary analysis by the HADES collaboration and mentioned above [29]. Furthermore, the question of contribution of the channels discussed above to the dielectron production can be raised and is of special interest for the HADES collaboration.

1.4 Motivation for the study of the $pn \to de^+e^-$ channel with HADES

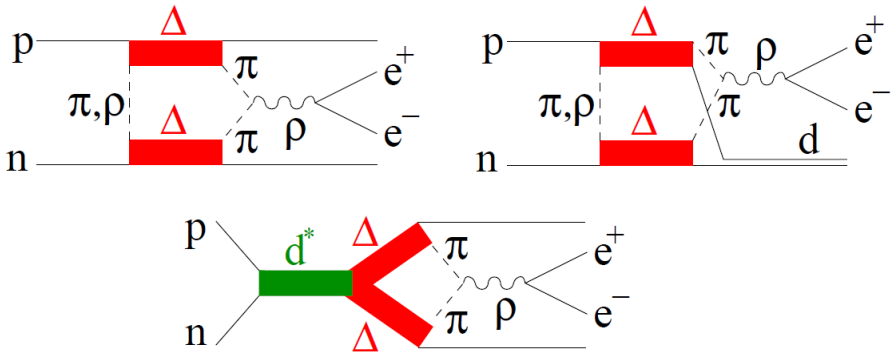

Figure 1.15: Graphs for the e^+e^- production via ρ^0 channel $\pi^+\pi^-$ production in pn collisions. Top: production via t-channel $\Delta\Delta$ excitation leading to pn (left) and deuteron (right) final states. Bottom: production via s-channel d^* formation and its subsequent decay into the $\Delta\Delta$ system [52].

In the discussion of the inclusive e^+e^- production in $n+p$ collisions (sec. 1.2.2), we have not discussed possible contributions to the related to the deuteron formation in the final state.

Recently, M. Bashkanov and H. Clement [52] have pointed out that there might be a strong contribution originating from subthreshold ρ production in $n+p \to \Delta\Delta \to \rho d$ (and/or ρnp) channels. Such production via intermediate $\Delta\Delta$ state can only be realized in $n+p$ collisions due to non-vanishing 9j recoupling coefficients for the intermediate $\Delta\Delta$ and $I = 1(\rho)$ di-pion final state. The importance of $\Delta\Delta$ channel for the $\pi^+\pi^-$ production has been already discussed in previous section.Figure 1.15 presents Feynman diagrams of the most important sources with intermediate rho meson. Results of this calculations are shown on figure 1.16. The authors estimate the total cross section for the ρ meson production in np collisions to be in the order of 310 μb. The main channels are

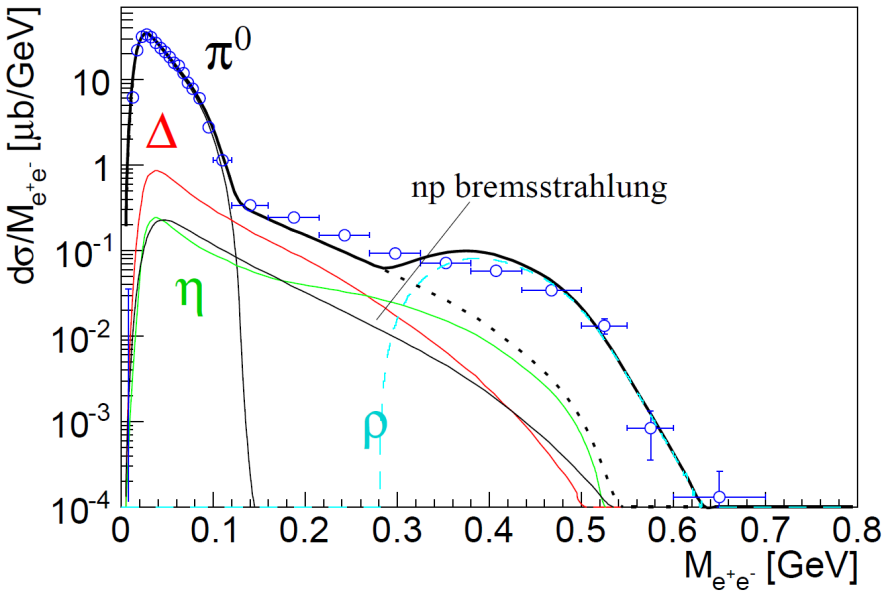

Figure 1.16: Distribution of the invariant mass $M_{e^+e^-}$ produced in pn collisions at $T_p = 1.25$ GeV. HADES data are shown as open circles. Thin black solid lines denote calculations for e^+e^- production originating from π^0 production and bremsstrahlung, single Δ (red) and η (green) production with subsequent Dalitz decay. The dotted curve denotes the sum of these processes. The dashed (cyan) curve gives the contribution from the ρ^0-channel $\pi^+\pi^-$ production and the thick solid line the sum of all these processes [52].

$np \to \Delta\Delta \to np\rho$ with cross section $\approx 170\ \mu b$, $np \to \Delta\Delta \to d\rho$ with cross section $\approx 100\ \mu b$ and finally contribution coming from the dibaryon resonance $np \to d^* \to \Delta\Delta \to np\rho$ with a cross section $\approx 40\ \mu b$. For the transition between ρ into e^+e^- system a Breit-Wigner formula has been used:

$$\mid BR(\pi^+\pi^- \to \rho \to e^+e^-) \mid^2 = \frac{m_\rho^2 \Gamma_{\pi^+\pi^-}\Gamma_{e^+e^-}}{(s-m_\rho^2)^2 + m_\rho^2\Gamma_\rho^2} \tag{1.3}$$

As one can see, results of these calculations describe the experimental data very well and the remaining under-estimation for e^+e^- invariant masses around 200 MeV could be explained by the direct d^* decay $np \to d^* \to de^+e^-$ or $np \to d^* \to np_{[I=0]}e^+e^-$, which were not included in this work, because there is no clear understanding of the di-baryon resonance internal structure and of the related electromagnetic transition form-factors.

A very interesting alternative explanation of the dielectron excess in np collisions was provided by B.V. Martemyanov and M.I. Krivoruchenko in [53]. The authors suggest the radiative capture $np \to d\gamma \to de^+e^-$ as a possible source of e^+e^-. This channel was never considered as a possible source of dileptons in np collisions before. This contribution is large in the region $M > 0.4$ GeV, when a VDM model is assumed for the electromagnetic transition. To estimate the cross section of the $np \to de^+e^-$ reaction, the authors used experimental data on deuteron photo-disintegration $\gamma d \to np$ at a photon energy $E_\gamma = 600MeV$. The conversion of the photon to a dilepton pair included phase space correction, form factor (in the simple VDM form) and conversion factor. The total cross section for this process is expected to be in the order of 41.7 nb. Results of these calculations can be seen on figure 1.17.

The experimental check of this contribution has been a direct motivation for the dilep-

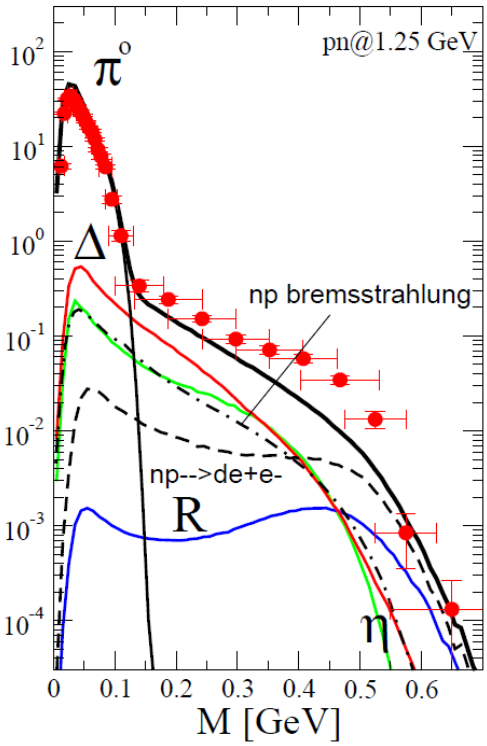

Figure 1.17: Dilepton spectrum of the $np \to e^+e^-X$ reaction. Contributions o π^0-meson, η, $\Delta(1232)$, and other baryon resonances are marked by the symbols π^0, η, Δ and R, respectively. Bremsstrahlung contribution is shown by the dash-dotted line. Also radiative capture $np \to de^+e^-$ is added as dashed line. All contributions are summed up incoherently and presented as thick solid line. [53]

ton analysis presented in this PhD, which will be the subject of chapter 5 In particular, the upper limit for the cross section of the de^+e^- final state has been calculated and compared to the model predictions. The channels with unbound np final state were subject of the complementary analysis by R. Trebacz [54].

Chapter 2

The HADES spectrometer

The HADES detector [13], as shown in figure 2.1, consists of 6 identical sectors covering the full azimuthal range and polar angles from 18° to 84° with respect to the beam direction. Each sector contains: A Ring Imaging CHerenkov (RICH) detector used for electron identification; two sets of Mini-Drift Chambers (MDC) with 4 modules per sector placed in front and behind the magnetic field to determine momenta of charged particles ; Time-Of-Flight detectors (TOF/TOFINO) and Pre-Shower detector improving the electron identification. In addition, a wall of scintillators, the Forward Wall (FW) was placed 7m downstream from the target.

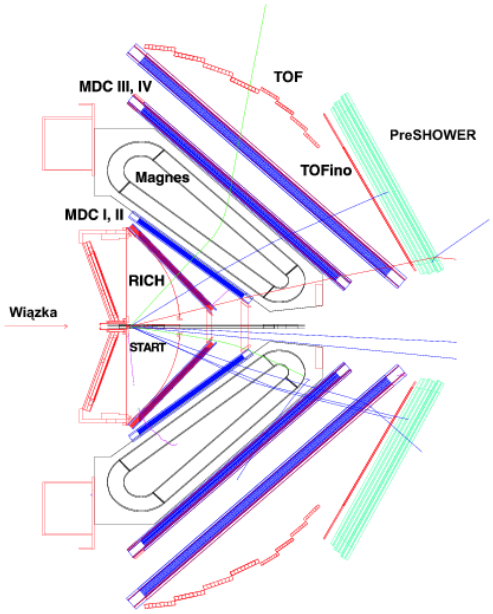

Figure 2.1: Schematic layout of the HADES detector.

A di-electron invariant mass resolution at the ω peak of $\sim$ 2.7% and a momentum resolution for protons of 4% can be achieved. The first level trigger is obtained by a fast multiplicity signal coming from the TOF/TOFINO wall, combined with a reaction signal from the START detector, when vailable. In the case of the dp experiment, a signal from the FW was also required. The second level trigger is made by using the information from the RICH and Pre-Shower to enrich the recorded events with lepton candidates. The HADES detector is designed for di-electron spectroscopy, but because of its large acceptance and good momentum resolution it is also suited for the detection of hadrons. In the following sections, the target used for the $p+p$ and $p+n$ reactions as well as each sub-detector system will be described in more details.

2.1 Target

In the p+$p(n)$ experiment, the liquid-hydrogen (LH2) target, which has been developed at IPN Orsay, was used (see 2.2). The target consists of a 5 cm long cylinder with a diameter of 2.5 cm which is filled with LH2 at atmospheric pressure and a temperature of 20 K. The liquid is contained in a vessel built out of Mylar foils of 100 μm thickness, glued together. The thermal insulation is achieved using a carbon fiber housing, 4 cm in diameter and 0.5 mm in thickness, placed around the vessel and covered by 10 layers of 6 μm thick aluminized Mylar which is super-insulation. The forward endcap is made of a 100 μ thick Mylar foil.

Figure 2.2: The liquid hydrogen target vessel with a diameter of 2.5 cm. The entrance window is glued on a stainless steel cylinder.

2.2 The Ring Imaging Cherenkov detector

The HADES Ring Imaging Cherenkov detector (RICH) (see 2.3) constitutes the innermost part of the spectrometer and is built to identify e^+e^- pairs. The detector is designed based on the Cherenkov effect, which is the electromagnetic radiation emitted when a charged particle passes through a transparent medium of refraction index n at a speed greater than the speed of light in that medium (so $v > c/n$). The opening angle between the emitted cone of light and the particle direction is given by:

$$\begin{aligned} cos\theta &= \frac{1}{n\beta}, \\ \beta &= \sqrt{1 - \frac{1}{\gamma^2}}, \end{aligned} \tag{2.1}$$

where θ is the opening angle, β and γ are the velocity and Lorentz factor of the particle respectively. In the energy range of our experiment, i.e. 1-2 GeV, electrons have velocities close to the speed of light, while most of the hadrons have much lower velocities and don not radiate photons By choosing a dielectric medium (CF_4) with an appropriate refraction index, the Cherenkov effect becomes a reliable tool to discriminate leptons from hadrons.

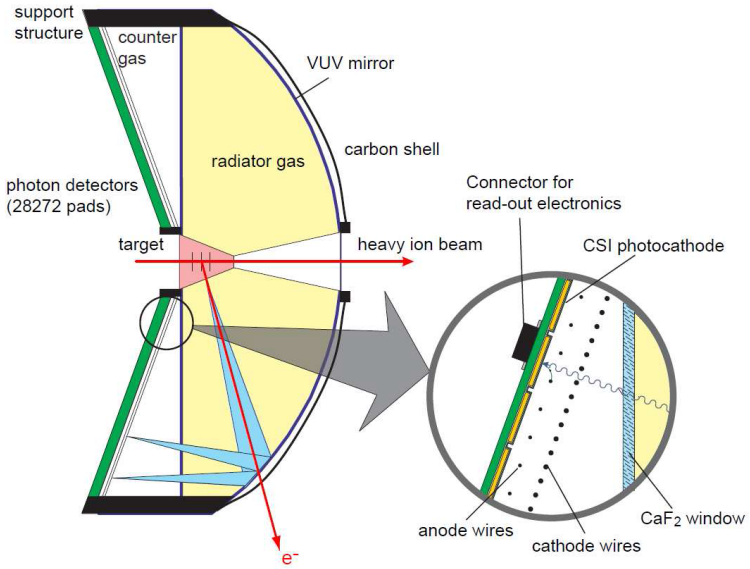

Figure 2.3: Schematic layout of the RICH, consisting of a Carbon shell mirror, a CaF_2 window and a photon detector.

As one of the most important components, the radiator gas in HADES RICH detector is chosen as C_4F_{10}. It has a refraction index of n=1.00151 and the corresponding Cherenkov threshold is $\gamma > 18.2$. It means that, to produce the Cherenkov light, the velocity β of a particle should be greater than 0.9985, which corresponds to: 0.009 GeV/c for an electron, 2.5 GeV/c for a pion and 17 GeV/c for a proton. In the HADES experiment energy range, the momentum of electrons is much higher than the 0.009 GeV/c threshold and most of the protons and pions have momenta significantly below the threshold. Just to give an idea, in $p+p$ collisions at 1.25 GeV, the maximum momenta are about 2 GeV/c for protons and 1 GeV/c for π^+. The radiator gas offers also high transparency to the wavelengths down to $\lambda \geq 145$ nm, which is well suited since the produced photons are mostly at ultra-violet frequencies. The spherical carbon mirror is placed downstream of the gas radiator and reflects the Cherenkov light (average reflectivity is $\sin 80\%$) to the photon detector which is able to detect a single photon providing an information about position. Typically, an electron with a momentum of 0.1 GeV/c produces about 110 photons along its trajectory in the radiator but only about 20 are detected.

2.3 Tracking system

The tracking system of HADES consists of a toroidal field provided by the superconducting coils and four planes of low-mass mini drift chambers (MDC) (see left panel of fig. 2.4). It allows to reconstruct the particle trajectories in a large solid angle (θ from 14° to 86°) and to determine the particle momentum with a resolution of $\Delta p/p \sim 4\%$ for protons.

2.3.1 The superconducting Magnet

The Iron-Less Superconductive Electromagnet (ILSE) [55] consists of 6 superconducting coils, producing an inhomogeneous magnetic field up to a maximum value of 0.7 T

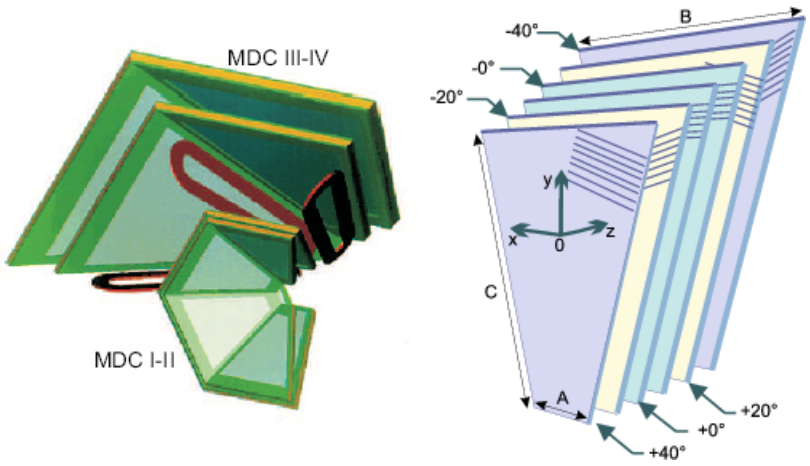

Figure 2.4: Schematic layout of the HADES tracking system. **Left**: Arrangement of the MDC chamber with respect to the magnetic coils. **Right**: View of the six anode wire frames inside a HADES MDC, with the respective wire angles.

within the acceptance region. This value corresponds to

$$\begin{aligned} \int B \cdot dl &\simeq 0.3\,T \cdot m, \ at\,\theta = 20^\circ \\ \int B \cdot dl &\simeq 0.12\,T \cdot m, \ at\,\theta = 70^\circ \end{aligned} \tag{2.2}$$

where $\int B \cdot dl$ is the integrated magnetic field. Moreover, a field free region is required (below $5 \cdot 10^{-3}$ T) at the position of the RICH and the TOF/TOFINO detectors. At the maximum field value, the transverse momentum kick p_k ranges between 0.03 and 0.1 GeV/c, where p_k is the momentum difference between the incoming and outgoing momentum vectors in the plane perpendicular to the field. For example, for a particle of charge ± 1 having momentum p= 1 GeV/c and emitted at $\theta = 20^\circ$, its momentum kick p_k amounts to 0.1 GeV/c (so the deflection angle is $\Delta\theta = 5.7^\circ$).

2.3.2 The MDC detector

The tracking is performed by 24 trapezoidal Mini-Drift Chambers(MDC) divided into 6 identical sectors of 4 planes. The sectors are symmetrically arranged around the beam direction. In each sector, 4 planes are placed, two in front of and two behind the magnetic field with increasing size. All the 24 chambers together provide a polar coverage between 14° to 84° and nearly full azimuthal coverage.
Each chamber is composed of six sense/field wire layers (called anode planes) oriented in different stereo angles from the inner layer to the outer: $+40^\circ$, -20°, $+0^\circ$, -0°, $+20^\circ$, -40° in order to have a maximum spatial resolution (see right panel of fig. 2.4). There are also seven cathode wire layers (called cathode planes), so that each sense/field wire layer is in between two cathode planes. For MDC IV, the gap between anode plane and cathode plane is 5 mm. The space between anode and field wires defines a drift cell. All four chambers contain about 1100 drift cells each with a size in average varying from 5×5 to 14×10 mm^2 from plane I to plane IV to achieve a constant detector occupancy. In each chamber, the windows consist of aluminized Mylar foils. Inside the chamber, a Helium:Isobutane (= 60:40) gas mixture is circulated during operation with an overpressure below 1 millibar. A new gas mixture based on argon (Argon:Isobutane = 84:16) has been tested and was used in following experiments.

When a particle crosses these drift cells, it ionises the gas and produces electron/positive ion pairs along its trajectory. The electrons migrate towards the anode wires and produce further ionisation especially close to the anode wire. The collected charges induce a signal on the anode wires. For each hit wire the corresponding drift times depend on the minimal distance of the particle trajectory from the wire. Note that the relation between drift time and the drift distance is not linear in our case due to the fact that the electric field is not constant in the drift cells and it is calculated by a Garfield simulation [56].

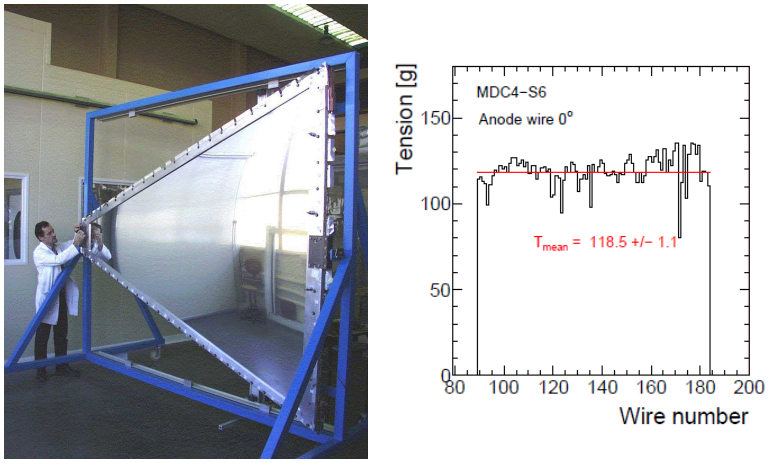

Figure 2.5: **Left**: View of the one HADES Mini-Drift-Chamber, MDC plane IV. **Right**: An example of measured tension of sense wire of anode plane. *right picture to be removed*

The IPN Orsay was responsible for the construction of the MDC plane IV during 2001-2006. Those planes are 280 cm high and 230 cm long from the bottom and are the biggest MDC chambers among the 4 HADES MDC planes (see left panel of fig. 2.5). Due to the unusual big size of the chamber, a lot of difficulties were addressed during construction and finally solved. For example, a careful winding is realized to obtain the designed tension and to make sure in the meantime that even for the longest wire we are well below the instability limit of the wire. The diameter of the gold-plated tungsten sense wire was chosen to be 30 μm in order to reduce the breaking probability of the wires. A carbon bar was added to maintain the wire tension at the value of 110 N after mounting to the frame.

2.4 The Multiplicity Electron Trigger Array system

The Multiplicity Electron Trigger Array (META) system is positioned downstream behind the outer MDCs and used for particle identification and triggering. The system is formed by two sets of time-of-flight detector (TOF and TOFINO) and an electromagnetic shower detector.

2.4.1 The Time-Of-Flight detector

For the time-of-flight measurements in the polar angle region from 44° to 88°, the TOF detector is used. Following the hexagonal geometry of the whole spectrometer, the TOF detector is divided into six sectors (left panel of fig. 2.6. Each sector consists of 64 scintillator rods (384 rods in total) coupled on both ends to photo-multipliers (PMT). The rod length increases while ranging from the smaller to larger polar angles. This geometry allows to have a finer granularity in the forward polar angle region, where the multiplicity

of produced charged particles is higher, to reduce the probability that two particles hit the same rod. The time resolution is about 150 ps.
From the measured signals the following information can be extracted : the time-of-flight (t_{tof}) of particles, the hit position on the rod (x), and the energy deposited in the rod (ΔE) with following formulas :

$$\begin{aligned} t_{tof} &= \frac{1}{2}(t_{left} + t_{right} - \frac{L}{v_{group}}), \\ x &= \frac{1}{2}(t_{left} - t_{right}) \cdot v_{group}, \\ \Delta E &= k \cdot \sqrt{A_{left} A_{right}} \cdot e^{L/2\lambda_{at}} \end{aligned} \tag{2.3}$$

where t_{left} and t_{right} is the time measured on the left and the right side of the rod corresponding to the time between the reaction and the readout of the signal, v_{group} is the group velocity in the rod (average velocity of light in the rod), L is the length of the rod, A_{left} and A_{right} are the signal amplitudes at the left and the right ends of the rod, λ_{at} is the light attenuation length of the rod and k is a constant. The region of polar angle below 45° was covered by a low granularity system called TOFINO. It is divided into six sectors each consisting of four scintillator pads (see right panel of fig. 2.6), arranged radially with respect to the beam axis. The basic principle is the same as for the TOF detector. In the case of the TOFINO detector, only one end is coupled to a PMT, so there is no information about the hit position. But directly behind the TOFINO detector, the Pre-Shower detector (will be described in the next section) is mounted, which provides the coordinate information of the particle hit on the paddle (x). The time-of-flight (t_{tof}) can be calculated using the following equation :

$$t_{tof} = t - \frac{x}{v_{group}}, \tag{2.4}$$

where t is the time interval between the reaction and the arrival of the light pulse at the PMT, v_{group} the light group velocity in the pad and x the distance from the particle hit position to the PMT. The time resolution of TOFINO is about 420 ps, worse than TOF. A Resistive Plate Chamber (RPC) wall has been installed in 2010 to overcome the shortcomings of the TOFINO. The new RPC detector replaces the TOFINO detector and operates since 2011.

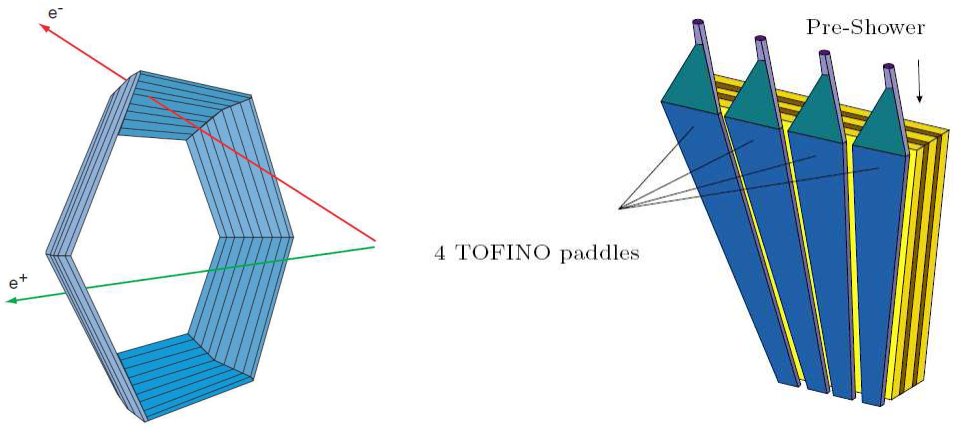

Figure 2.6: Schematic view of the **Left**: TOF and **Right**:TOFINO detector (one sector only).

2.4.2 Pre-Shower

In the lower polar angle region, the separation of electrons from protons by time-of-flight measurements is more difficult, due to the higher momenta of hadrons. In order to improve the lepton/hadron discrimination, a detector of electromagnetic showers (Pre-Shower) is used.

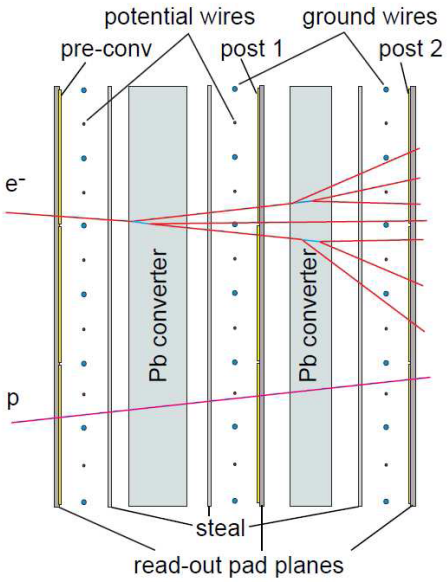

Figure 2.7: Side view of the Pre-Shower detector (one sector) with an example of electromagnetic shower.

The Pre-Shower detector consists of a stack of three trapezoidal wire chambers (pre-chamber, post1-chamber, post2-chamber), separated by two lead converter plates. Each cathode plane is further divided into individual pads. A charged particle passing through the gas chambers produces an ionisation avalanche, with electrons drifting towards the closest anode wire ; the cloud motion induces a positive charge on the nearby cathode pads, connected to charge-sensitive preamplifiers. The integrated charge is proportional to the avalanche charge, and an integration over several pads around the pad with the highest charge value (local maximum) has to be performed, in order to obtain the complete charge of the electromagnetic shower. By comparing the integrated charge of the same track in different layers it is possible to distinguish electromagnetic showers from hadronic tracks, as will be discussed in more detail in sec.3.3.4. The replacement of Pre-Shower detector by a lead glass calorimeter is foreseen for HADES operation at FAIR.

2.5 Forward Wall

The Forward Wall detector is presented in Fig. 2.8. Its main purposes are to detect the spectator particles in deuteron proton reactions and to allow for event plane reconstruction in A+A collisions. It covers polar angles from 0.13° to 7.1°. It consists of scintillators of three different sizes equipped with photomultipliers modules. The size of the modules varies from 40 mm×40 mm for 156 modules, 80 mm×80 mm for 88 pieces to 160 mm×160 mm for 76 on the border of the detector. In total there are 320 scintillator and photomultiplier modules (see Fig. 2.8 top). The thickness of the cells is 2.54 cm. The estimated time resolution of the FW depends on the scintillator size and varies from 550 to 800 ps.

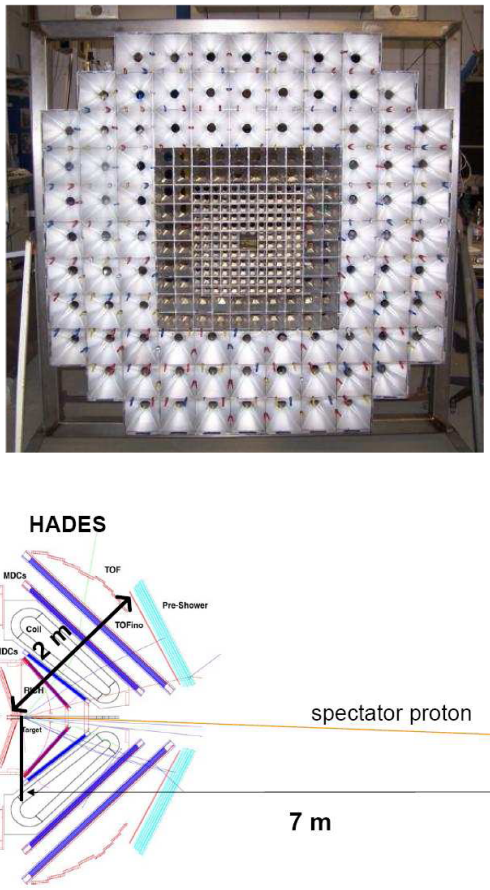

Figure 2.8: **Top**: Front view of the Forward-Wall detector without mounted detectors. The size of the modules increases when going from the inner to the outer area of the detector. **Bottom**: Sketch of the HADES spectrometer and the the Forward Wall detector.

2.6 The trigger system

A two level trigger system is used in the HADES experiments:
– 1st level trigger : The first level trigger (noted as LVL1) consists of a fast hardware selection of central collisions, by measuring the hit multiplicity in META system. It is possible to apply multiplicity selections in TOF and TOFINO separately and sector-wise, in order to select only interesting decay channels, which is used for example for proton-proton elastic events. In the case of the dp experiment, a signal in the FW is also required.
– 2nd level trigger: The second level trigger (noted as LVL2) is based on an online search for lepton candidates in the event. It comprises ring search in the RICH and electromagnetic shower in the Pre-Shower detection. The spatial coordinates of electron candidates are sent to the matching unit for final acceptance in case they are correlated The events accepted by the LVL1 trigger decision are sent to the matching unit board and processes with the following options:
– If the events contain a lepton candidate, they are accepted by the LVL2 trigger and then are all written to the file for di-electron analysis. They are called LVL2 events.
– Disregarding whether the events contain a lepton candidate or not, all the events are sent to a downscaling box which reduces the number of events by a corresponding factor (called LVL1 dsf). They are finally recorded in the files, for hadronic analysis and normalization factors. They are called downscaled LVL1 events.

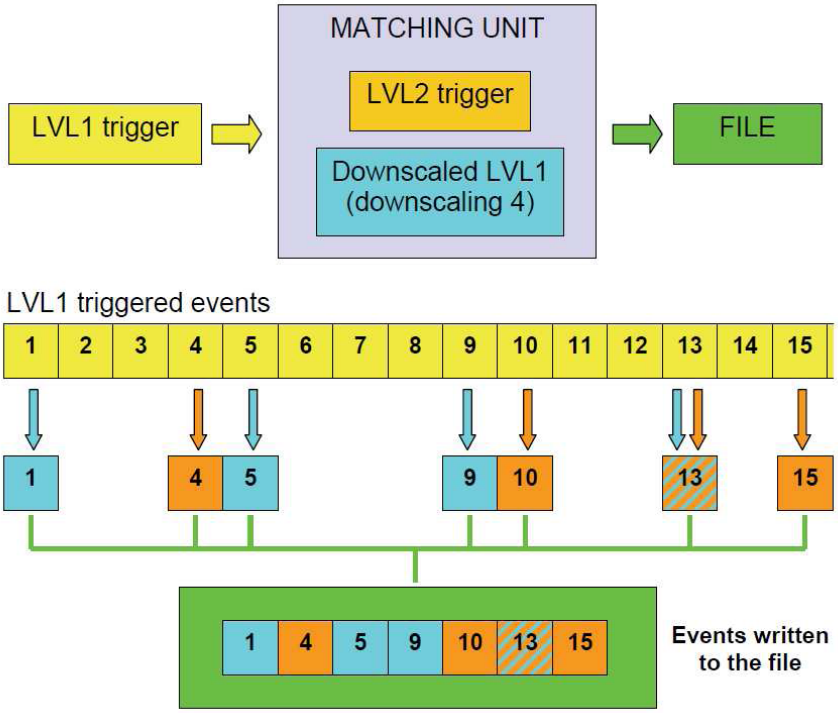

Figure 2.9: Sketch of the event selection used for data acquisition.

The downscaled LVL1 events are recorded because we are also interested in events which contain hadrons. However, the rate of hadronic events is so high that their number has to be reduced. Fig. 2.9 gives a schematic explanation of the event selection used for data acquisition. The first selection of the events is done by the LVL1 trigger (yellow boxes), and they are sent to the matching unit afterwards where the downscaling factor is defined, for example factor 4 was selected for dp experiment. This means that one event out of four is stored (event number 1, 5, 9, 13, ...) (labelled by blue boxes), no matter the LVL2 trigger decision. In the meantime, all the events with a recognized lepton candidate are stored as well (labeled orange boxes). It can happen that an event can be at the same time downscaled by the LVL1 trigger and be accepted by LVL2 trigger, like for instance the event number 13 in the example. If we want to have the total number of the events, we must multiply the number of downscaled LVL1 events (4) by the downscaling factor (4). In this case, we obtain 16 events against 7 which are effectively stored to file. This means that in the example we found 4 events with electron candidates by storing only 7 events instead of 16. In this particular case, we have roughly saved half of the disk space, and half of the time needed for the data processing.

Chapter 3

Data analysis methods

A modern experiment in hadron physics requires spectrometers consisting of many sub-detectors. All HADES sub-systems were described in the previous chapter of this thesis. Each detection system gives specific information about particles passing through. Gathering information from all sub-detectors allows finally for particle identification and reconstruction of momentum vector. Such a complexity of the measuring machinery together with high statistics of selected events requires the use of dedicated tools for the analysis.

In this chapter, the general tools used for the HADES analyses are first introduced. Then, the methods for particle identification and selection of the signals of interest (quasifree $pn \rightarrow d\pi^+\pi^-$ and $pn \rightarrow de^+e^-$) are presented. Finally, the procedures for normalization and efficiency correction are described.

3.1 Analysis framework

The HADES analyses are realized within the HYDRA framework [57], i.e. the **H**ades s**Y**stem for **D**ata **R**eduction and **A**nalysis, based entirely on the C++ class package ROOT [58]. This approach allows full and consistent use of all built-in features of the ROOT software developed and maintained at CERN, and which has become a standard in most high energy and nuclear physics experiments.

A schematic flow diagram of data analysis from simulation and experimental data is shown in Fig. 3.1. The analysis can be divided into steps of raw data processing, calibration, track reconstruction, particle identification and final step of reaction channel selection. The simulation part, in addition to aforementioned steps, contains detailed emulation of detector response including trigger conditions. There is a faster option of analysis of simulation events based on filtering by dedicated acceptance and efficiency matrices, that will be described in details below.

The first step of the experimental data analysis is the DST (**D**ata **S**ummary **T**apes) production which is a common basis of all analyses in the HADES collaboration. On this level, the HYDRA framework is used to translate detector electronic signals to the physical informations like identified hits on RICH, MDC, TOF/TOFINO and Pre-Shower with corresponding parameters like hit coordinates, time of flights values, energy loss etc. and also reconstructed tracks in MDCs.

DST files are input to the PAT (**P**ostDST **A**nalysis **T**ool) framework. On this step, event hypothesis are checked based on pre-defined set of particles which are expected in final state of the given reaction channel. Based on this criteria, only interesting events are selected from whole experimental data. Furthermore, on this level, particle identification (PID) is performed via conditions defined on velocity and momentum correlation. More

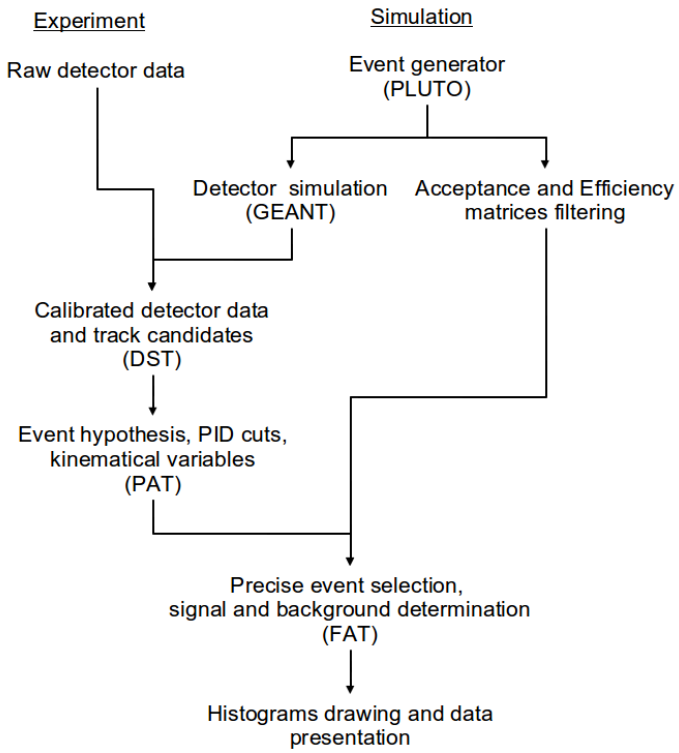

Figure 3.1: Data and simulation analysis flow relevant for this PHD work.

details on these aspects will be given in Sec. 3.3.3.

The output files from PAT include detector specific variables like energy loss, time of flight and also kinematical variables like angles, total momentum, particle type, energy, etc. The next step in the analysis chain is provided by the **F**inal **A**nalysis **T**ool (FAT), where physical information e.g. invariant mass, total energy, distribution angles, etc. is extracted for the previously selected events. Based on this information, the background is also identified and removed. Background subtraction is especially important in case of dilepton production, due to the contribution of γ conversion, as discussed in Sec. 3.3.4.

Finally, the distributions of count rates obtained for a given reaction channel are converted to differential cross sections using normalization factors calculated from simultaneously measured pp elastic scattering events, as described in Sec. 3.6.

The comparison of the experimental differential distributions with model predictions requires the use of simulations, in order to take into account experimental effects. In the analysis of simulated events the same steps are performed as in the case of experimental data. Events are generated, following theoretical distributions, using a comprehensive and modular ROOT-based event generator, called PLUTO++ [59, 60] developed by the HADES collaboration. Then, simulated events are interfaced to the detector simulation package GEANT3 [61] for the detector response calculation. Event overlay, i.e. the embedding of simulated tracks into real events for efficiency and performance investigations, is supported as well. This so called "full chain" simulation is a very time consuming and complex task. Therefore, it is done usually as a final cross check of a more pragmatic approach, based on filtering of events by acceptance and efficiency matrices. These objects are computed with the "full chain" and represent spectrometer acceptance, resolution, and detection efficiency for each particle species (i.e electrons, positrons, pions and protons). The matrices are generated based on simulated single particle "white tracks" uniformly distributed as a function of the momentum, polar and azimuthal (p, θ, ϕ) emission angles. More detailed description and results concerning matrices are the subject of Sec. 3.7

3.2 Reaction channels of interest

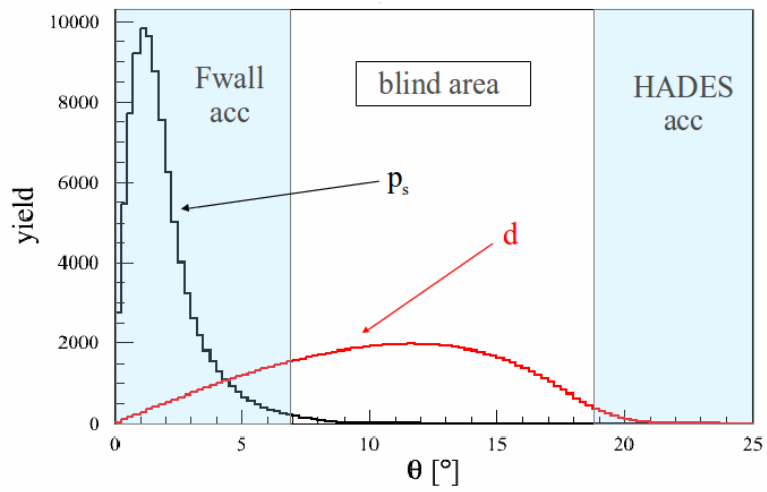

Figure 3.2: The red solid line shows the deuteron polar angle distribution in laboratory rest frame. Deuterons are produced in phase space simulations of the $dp \rightarrow d\pi\pi + p_{spectator}$ reaction channels. The light blue areas show the two acceptance regions (below 7 degrees for the detection in Forward Wall detector and above 18 degrees for the detection in the HADES spectrometer). In comparison, the polar angle of the proton spectator p_s from the quasi-free reaction, is presented as a black solid line. Between angles 7 up to 18 degrees, a blind area exists, where the detection is not possible.

The studies of $np \rightarrow d\pi^+\pi^-$ and $np \rightarrow de^+e^-$ are based on tagging the proton spectator in the Forward-Wall (FW) to select quasi-free np reactions from dp collisions. The main difficulty of the measurement of these channels is the identification of deuterons at small polar angles. This is illustrated in Figure 3.2, where the angular distributions of protons and deuterons from the $dp \rightarrow d\pi^+\pi^- p_{spec}$ reaction is shown with products distributed according to phase space. It is clearly shown that only a very small fraction of the deuterons are detected in HADES, where particle identification based on the measured momentum and velocity is possible. To detect most deuterons, the FW, which only provides a time of flight information with limited resolution (see Sec. 2.5) has to be used. The challenge is therefore to distinguish, in the FW, deuterons produced in the "fusion" reactions:

$$dp \rightarrow d\pi^+\pi^- p_{spec} \tag{3.1}$$

or

$$dp \rightarrow de^+e^- p_{spec} \tag{3.2}$$

both from the spectator protons emitted in the same reaction or from the spectator or emitted protons in the "unbound" processes:

$$dp \rightarrow np\pi + \pi^- p_{spec} \tag{3.3}$$

or

$$dp \rightarrow npe^+e^- p_{spec} \tag{3.4}$$

, which constitute the main background for the signal channel 3.1 or 3.2, respectively. As will be shown in Sec. 3.4.2, the time of flight measurement allows to distinguish deuterons from spectator protons, due to their different velocity (or time of flight) distribution. To reject protons emitted in the unbound process (3.3 or 3.4), an additonnal angular criterium (so-called "coplanarity" see Sec. 3.4.2) can be used sucessfully.

For the $dp \to de^+e^-p_{spec}$ reaction, only the case of deuterons detected in the FW and e^+e^- pair detected in the HADES detector was considered.

In the case of the $dp \to d\pi^+\pi^-p_{spec}$ reaction, the yield of deuterons reaching the HADES detector was still large enough to allow for a dedicated analysis. Studies of the $np \to d\pi\pi$ reaction channel were therefore separated in two distinguished cases :

1) deuteron and pions detected in HADES,

2) two pions detected in HADES and deuteron in Forward-Wall detector.

Particle identification in HADES and Forward-Wall are described respectively in Sec.3.3 and 3.4.

3.3 Charged particle identification in HADES spectrometer

In general, particle identification in HADES is obtained in three steps; (a) momentum determination in tracking system (MDCs and magnet) (b) time of flight calculation and (c) two dimensional graphical selection on the correlation of these two independently measured quantities. Furthermore, only events matched with the hypothesis of having certain particles in the final stage (i.e positron, electron or two charged pions and proton) are selected. In the experiments described in this thesis, it had not been possible to use a START detector because of the too large background induced in the RICH detector by the beam interactions with the detector material. To overcome this disadvantage, a special method to restore time information had been used and is described in Sec. 3.3.2

3.3.1 Momentum determination

The momentum of particles in the HADES detector can be obtained from their deflection in the magnetic field. This requires a measurement of the particle direction before and after the magnetic field. To achieve this, independent inner and outer straight track segments are reconstructed from the hit and drift time information in the pairs of drift chambers in front of and behind the field region, respectively. In next steps, both tracks are merged together and aligned with the TOF or the TOFINO/Pre-Shower hits. For electron identification, in addition, the inner MDC track segments are matched with the rings reconstructed in the RICH detector.

The mechanism of track segment matching with META detectors is presented in Fig. 3.3. The inner MDC track segments are projected to the target area assuming straight line approximation. Segments with best match to the target are selected. For outer segments, all combinations of hits are considered, but, then, both inner and outer MDC track segments are projected and matched on a special plane - the kick plane.

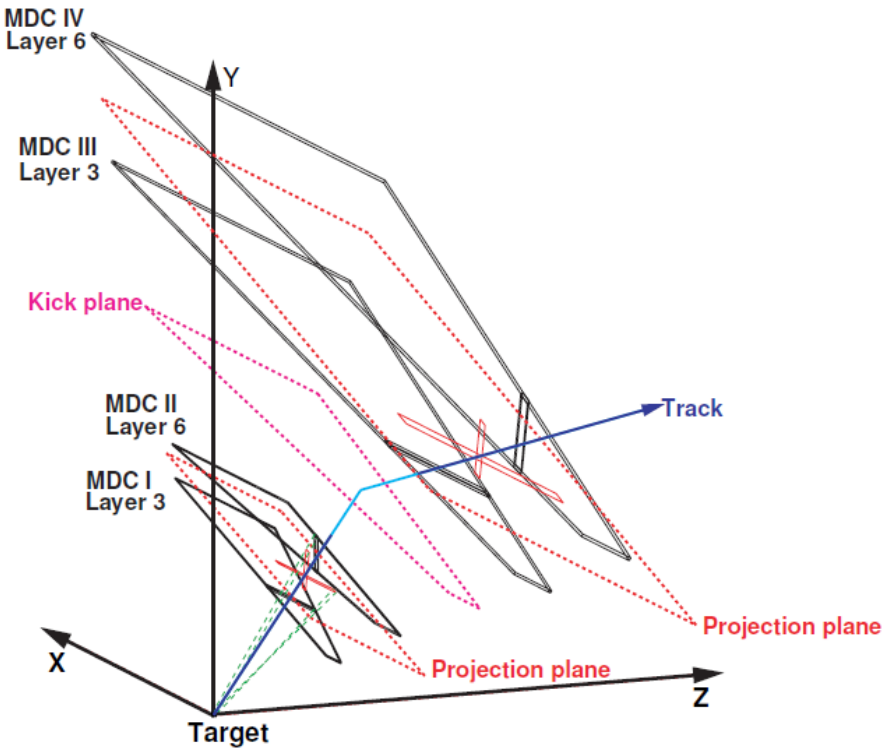

Figure 3.3: Principle of the track candidate search in the track reconstruction procedure. For an easy view, only one layer is shown in each MDC.

The kick plane is in fact a surface, obtained from simulations, which approximates the deflection of charged particles in the HADES magnetic field just by a sudden change - a "kick"- of the trajectory [56] occuring in the kick plane. Knowing the deflection of a particle in the magnetic field of known strength and its charge, one is able to calculate its momentum. This provides a very fast initial value of the momentum, to be used as starting point in the subsequent more refined track fitting algorithm, aiming at a final precise determination of the momentum. The latter consist of two steps. First the cubic spline method [13, 62] is applied to calculate first approximation of the momentum. Second, based on the previous result, a fourth order Runge Kutta algorithm of Nystrom [63] is used. Implementation of this method solves differential equations of motion in the known magnetic field. With such a procedure, the momentum resolutions are of the order of 1-2% for electrons, and 2-3% for pions and deuterons [13].

3.3.2 Time of flight calculation without START detector

Time of flight in HADES are calculated in general using the difference of arrival times between the START detector and TOF/TOFino detector signals. However, for high intensity proton/deuteron beams, it was not possible to use a START detector because too much background is created by beam interactions with detector material, hence making a stable RICH operation impossible. As a consequence, the start time was given for each event, by the trigger signal, which was related to the earliest signal in either TOF, TOFINO or FW detectors. Therefore, there was no common time reference for tracks in the different events.

However, two properties can be used to reconstruct the time of flight. First, since the same signal is used as a reference for time measurements in a given event, the differences between the time measurements in a given event give a useful information about relative

particle times of flight. This difference is written as:

$$\Delta t = \frac{t_1 - t_2}{2} \tag{3.5}$$

where t_1 and t_2 are times measured for a first and a second particle respectively and Δt is the respective time difference.

Second, using an assumption on the identification of the particles in the event, the time of flight can be calculated from the assumed mass and the momentum and track length provided by the tracking algorithm. In practice, the average theoretical time

$$\bar{t} = \frac{t_1^c + t_2^c}{2} \tag{3.6}$$

between both particles is used. Based on this assumption, the time of flight values for the particles can be recalculated as:

$$\begin{aligned} t_1^r &= \bar{t} + \Delta t \\ t_2^r &= \bar{t} - \Delta t \end{aligned} \tag{3.7}$$

The validity of the hypothesis can be checked by comparing the recalculated time t_i^r to the theoretical time t_i^c.

In practice, for more than two candidates in the final state, a matrix constructed from the whole set of possible combinations between available track candidates and particles in the hypothesis. To improve the algorithm and reduce the number of iterations, the relative time is calculated with respect to a pre-defined reference particle, i.e. a particle which can be identified by another, independent method.

The analysis of the $dp \rightarrow d\pi^+\pi^- p_{spec}$ channel consists of two separate hypothesis. One with d, π^+ and π^- detected in HADES and p_{spec} in FW and the second whith only π^+ and π^- detected in HADES and deuteron and p_{spec} being selected by additional conditions in FW.

For dielectron analysis, either electron or positron can be used as are reference particles, because they are identified independently by the RICH detector. For the dipion analysis, the negative particle in the event (i.e negative pion) is used as a reference because it can be uniquely identified using the bending direction in the magnetic field. Results of all combinations are sorted by χ^2 value calculated as below.

$$\chi_i^2 = \sum_j^N \frac{(t_j^r - t_j^c)^2}{\sigma_j^2(TOF, TOFino)} \tag{3.8}$$

where $\sigma_j(TOF, TOFino)$ is the detector time resolution for TOF and TOFino (see Sec. 2.4.1) and the sum runs over all particle species in the event. Finally, the combination with the smallest χ^2 value is chosen.

3.3.3 Time and momentum correlation

The final step in particle identification procedure consists of a check of the correlation between the momentum and time of flight. The time-of-flight is determined as explained in the previous section and the particle velocity is deduced using the track length. It is the checked that the correlation between momentum and velocity is compatible with the event hypothesis.

For the analysis of our channels, we are interested by the detection in HADES of

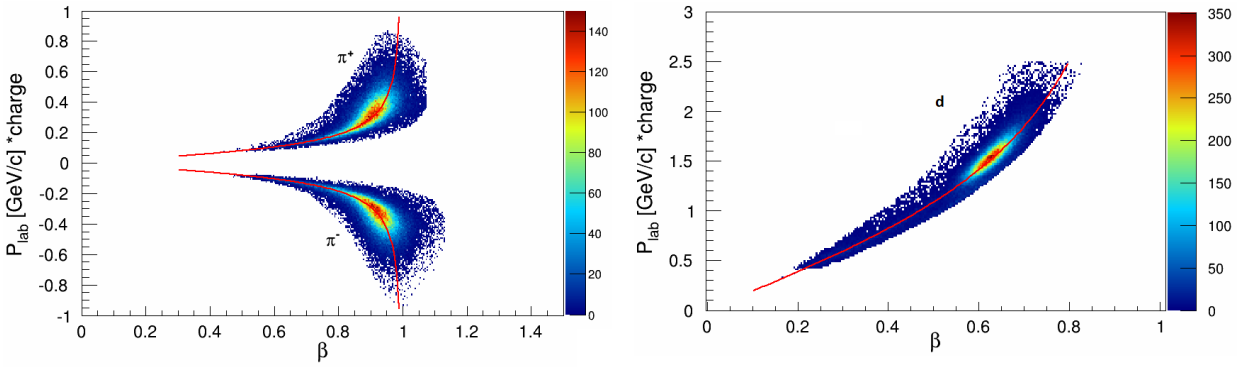

Figure 3.4: Experimental distribution of polarity×momentum vs beta for all particles used in analysis. Red solid lines show theoretical β vs p distribution for corresponding particle mass. Distribution corresponding to **left** charged pions ($\pi^+\pi^-$), **right** deuteron ,in case of the scenario with deuteron detected in HADES.

$e^+, e^-, \pi^+, \pi^-, d$ particles. The correlation between the product of charge and momentum ($q \times p$ and the velocity β is displayed in Fig 3.4 for hadrons and Fig 3.5 for dileptons (e^+e^-). It can be checked that they nicely follow the expected correlation

$$p = \beta * m/\sqrt{1-\beta^2}$$

, where m is the mass of the particle. However in case of the dilepton analysis an additional steps have to be made, as described in Sec. 3.3.4 and 3.3.4, in order to properly select e^+e^- particles.

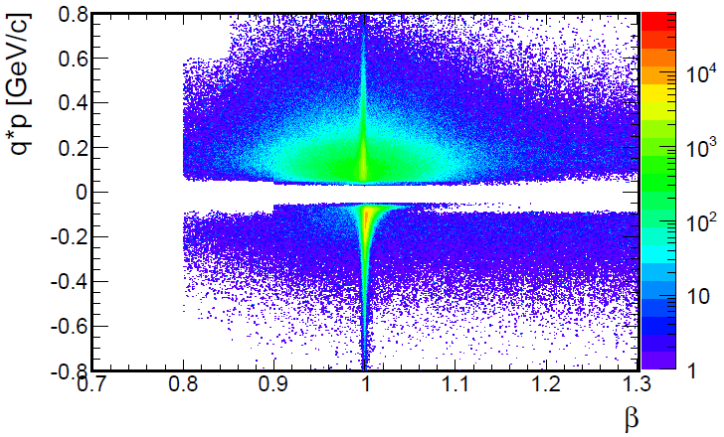

Figure 3.5: Experimental distribution of polarity×momentum vs beta for e^+e^- with additional dilepton identification steps (i.e. RICH-MDC correlation, Electromagnetic shower condition) [10].

3.3.4 Additional steps for lepton identification

When the analysis hypothesis contains leptons, additional steps have to be made to successfully identify and reconstruct electron/positron candidates. The primary criterion for the lepton is a detection of ring in RICH detector, described in chapter 2.2. One ring is identified and a spatial correlation between the track direction estimated from the ring location and the MDC tracks direction is considered. Additionally, if the leptons are

emitted at lower polar angles and pass through TOFINO detector, a pre-Shower detector is used to improve lepton selection. Both selection steps are described below:

RICH-MDC correlation: In order to uniquely identify electron tracks, a spatial correlation between the track directions found by the RICH and the inner MDCs track segments is considered using the difference of respective polar (Θ) and azimuthal (ϕ) angles. In the first step, on the DST level, a broad, momentum independent, window is used:

$$\Delta\Theta = \pm 7^{\circ}; \Delta\phi sin(\Theta) = \pm 7^{\circ} \tag{3.9}$$

where $\Delta\phi$ and $\Delta\Theta$ are the differences in the azimuthal and the polar angles, respectively. The factor $sin(\Theta)$ in $\Delta\phi sin(\Theta)$ is used to keep the same solid angle spanned in the case of azimuthal angles difference. In the next step, i.e. the PAT analysis, a more narrow window was calculated as a function of momentum separately for each sector of the spectrometer. To select good lepton tracks, these matching windows have been derived as:

$$-3\sigma_{\Theta} < \Delta\Theta < 3\sigma_{\Theta}; -3\sigma_{\phi} < \Delta\phi < 3\sigma_{\phi} \tag{3.10}$$

where σ_{ϕ} and σ_{Θ} were carefully calculated as a function of momentum from the gaussian fits to the projections of distributions shown in Fig. 3.6.

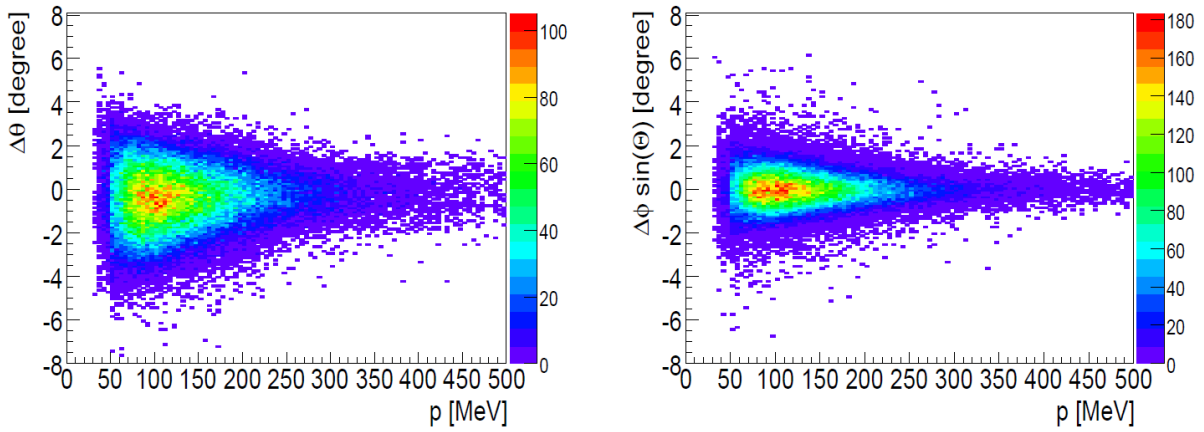

Figure 3.6: Spatial correlation between RICH hits and inner MDCs segment for polar and azimuthal angles.

Electromagnetic shower condition in the Pre-Shower detector

The main task of the Pre-Shower detector is to improve the lepton identification at $\Theta < 45^{\circ}$. It is based on the identification of an electromagnetic shower by comparing the charges in post1-, post2-chambers, For each chamber, these charges are integrated over a matrix of 3×3 pads around a local maximum as shown in Fig. 3.7.

The criterium which is used reads:

$$\sum Q_{post1,post2}(p) - \sum Q_{pre}(p) \geq Q_{th}(p) \tag{3.11}$$

where $Q_{th}(p)$ is the momentum-dependent threshold, based on simulation. Equation 3.11 is the sum of charges measured in the post1- and post2-chambers after subtraction of the pre-chamber charge. $Q_{th}(p)$ was optimized to obtain a constant electron identification efficiency of 80% for momenta larger than 0.1 GeV/c.

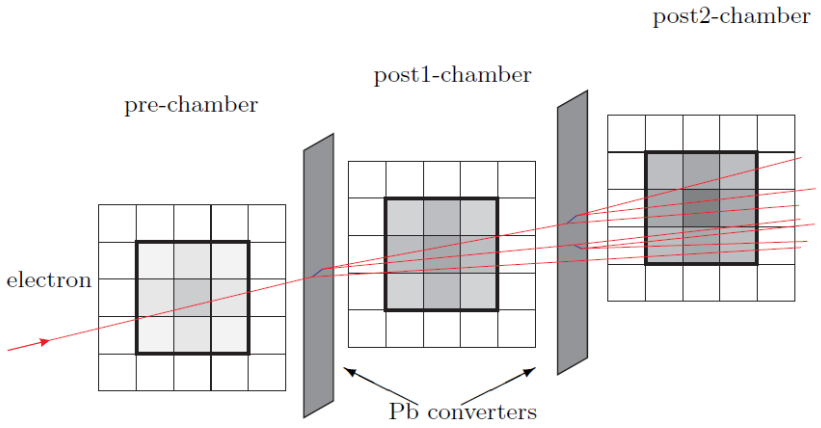

Figure 3.7: Schematic view of the shower algorithm. In each layer the sum of the charge over 3×3 pads is calculated. The larger charge deposition in the post-chambers is the signature of an electromagnetic shower [13] .

In Fig. 3.8, distributions of this sum for electrons and hadrons are presented, together with the pion suppression as a function of electron momentum. The achieved pion suppression for $p > 500 MeV/c$ is on a level of an order of magnitude. Moreover, the information on the energy loss in the pre-chamber is used to eliminate slow hadrons characterized by large energy loss. Finally, after applying all the cuts defined above, the e^+ and e^- regions are isolated, see Fig. 3.5, where the distribution of the momentum as a function of the velocity is shown. The sharp vertical lines are obtained when the particle is used as a reference particle in the reaction time reconstruction.

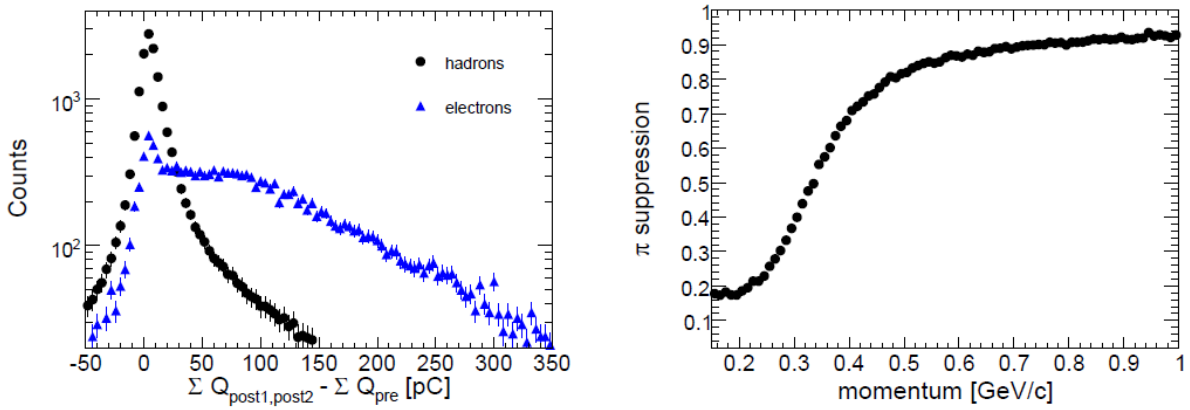

Figure 3.8: **Left:** Sum of charge $\sum Q$, over 3×3 pads, measured on post1- and post2-chamber with subtracted charge measured in the pre-chamber for hadrons (here π^- as black dots) and electrons (blue triangles). Electrons with momenta $p > 0.5$ GeV/c produce electromagnetic showers in the Pb converters which result in a larger charge deposit compared to the one from hadrons, here π^- (dots). **Right:** Pion suppression as a function of momentum: the fraction of pions rejected after the algorithm for lepton recognition (electromagnetic cascade) has been applied [13].

Combinatorial background

A final step of the dielectron analysis, before the signal extraction, is the estimation of the combinatorial background. Below, a short description of these steps can be found. A detailed discussion of the dielectron analysis from np collisions can be also found in ref. [10] and [54].

The main source of background in the e^+e^- final state are pairs produced by a photon conversion. The conversion background originates from external pair conversion of photons mainly from π^0 decay. It is a source of a combinatorial background (CB) arising when dilepton pairs are formed for all possible e^+e^- combinations from the same event. Indeed, a significant part of the reconstructed unlike-sign pairs are those coming from different decay vertex, hence such a fake signal has to be suppressed.

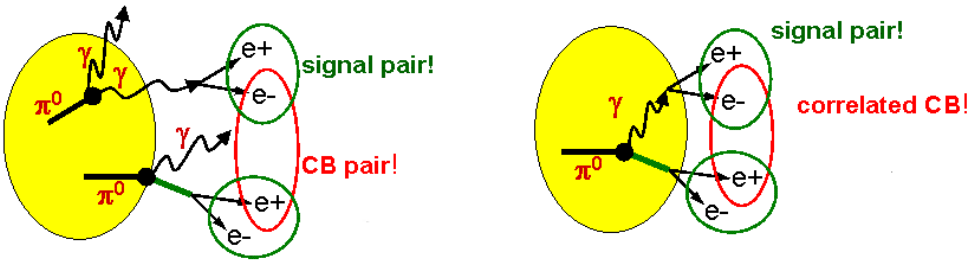

Figure 3.9: Example of sources of uncorrelated (left panel) and correlated (rigth panel) combinatorial background.

In more details, the combinatorial background can be observed as an uncorrelated and a correlated background (Fig. 3.9). Typically, the combination between leptons originating from two independent sources gives a contribution as a smooth background. The correlated background originates mainly from the $\pi^0 \rightarrow \gamma\gamma$ decay or the π^0 Dalitz decay, where positron and electron come either from two conversions or from the Dalitz decay and from the conversion in the same π^0 decay. This correlated background contributes at e^+e^- invariant masses below the π^0 mass.
In the HADES spectrometer, the combinatorial background is produced in the target or in the radiator gas of the RICH detector or in some parts of the target and RICH construction (flange). For example, photons emitted at the beginning of the target and at large polar angles can hit the RICH flange and convert into e^+e^- pair. Such pairs are suppressed using a square cut imposed on lepton tracks with momenta $p < 150 MeV/c$ and emission polar angles $\theta > 65°$ as well as a cut to remove tracks with reconstructed vertex z position smaller than $-50mm$. In subsequent experiments, the target was moved more downstream to suppress this effect.

The unlike-sign combinatorial background can be estimated in two ways. The first one, which is applied in the present analysis, is based on the fact that the yield of same-event (SE) like-sign CB is identical to the yield of unlike-sign CB [13]. Therefore, the combinatorial background can be obtained from the reconstructed like-sign distribution as:

$$N_{CB} = N_{++} + N_{--} \tag{3.12}$$

One should note that this method also provides absolute normalization for the combinatorial background estimated by the event-mixing (EM) approach that can be used for heavy ion data (e.g. in e^+e^- analysis of $C + C$ at $1GeV$ data). Event mixing technique

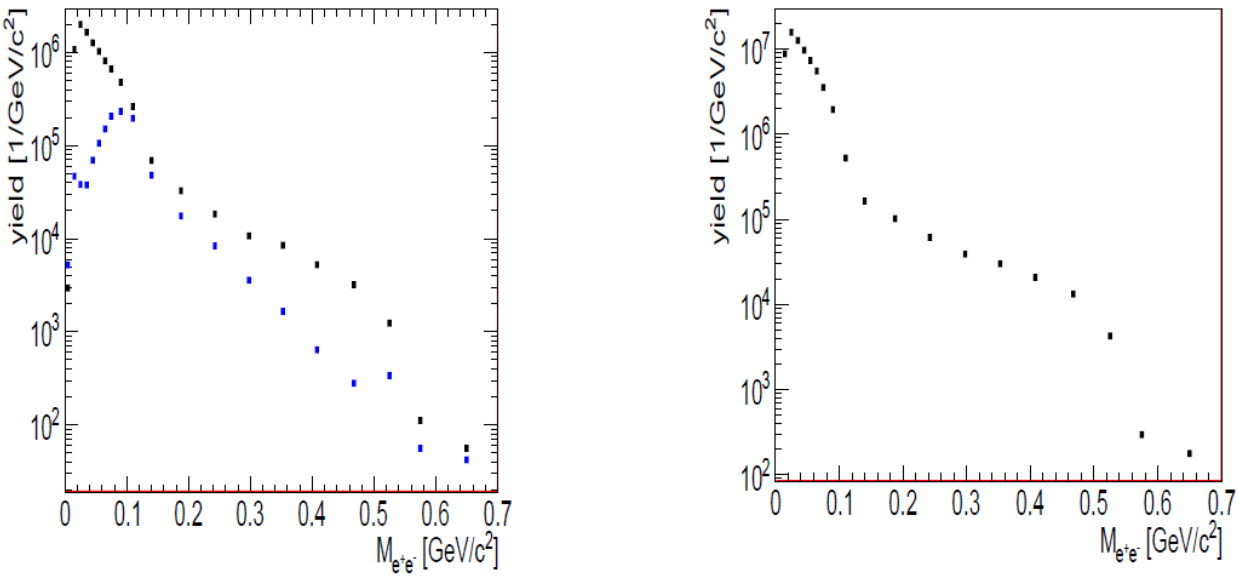

Figure 3.10: Inclusive dielectron invariant mass distribution before normalization to the $p + p$ elastic scattering yield. **Left**: Signal (black dots) and combinatorial background (blue dots). **Right**: Signal after CB subtraction and efficiency correction.

relies on selection of electron and positron from different events and combining them to form a combinatorial background. Thus, the CB obtained by the EM method is purely uncorrelated.

Both methods have advantages and disadvantages. The SE method properly describes correlated and uncorrelated CB, and must be used in the case of elementary reactions due momentum and energy conservation which must be preserved for each collision. In case of heavy ion reactions it can be used when dealing with sufficient statistics. For the latter case, usually the EM method is used since it does not have statistical limitations and conservation laws do not affect the shape of the spectra of uncorrelated background. However, one should still remember that EM properly describes only the shape of uncorrelated CB and it requires a proper normalization which must be provided by the SE method. For $N + N$ reactions SE method must be used since it naturally conserves the total energy in an event which is important for $N + N$ collisions.

3.4 Charged particle identification in Forward-Wall detector

Studying a $n+p$ reaction is a challenging technical issue. It is impossible to create and accelerate a pure mono-energetic neutron beam, neither construct a pure neutron target. To overcome this issue, a quasi free $n + p$ sub-reaction can be selected from the $d + p$ collisions by detecting the specator proton. Such a reaction is schematically presented on left panel of figure 3.11. The most important aspect of this process is that the interaction undergoes only between neutron from the deuteron nucleus and the free proton. In such a case, the proton from the deuteron nucleus moves undistorted after the collision. However, due to the finite momentum distribution of the nucleon inside the deuteron, the spectator properties are smeared around the nominal beam momentum.

In practice, the HADES collaboration used a deuterium beam with a kinetic energy $2.5GeV$, where each nucleon carries in average about half of this energy, corresponding

to a proton momentum $\sim 1.98 GeV$. However, the incident momentum of the nucleon is smeared due to its motion in the deuterium nucleus. To illustrate that, a simulation of the proton spectator momentum distribution for the quasi-free np reaction is shown in the right panel of figure 3.11. The nucleon momentum in the deuterium nucleus was taken into account using a model based on the Paris potential [64] and implemented in the PLUTO event generator. Spectator tagging in the HADES experiments is provided

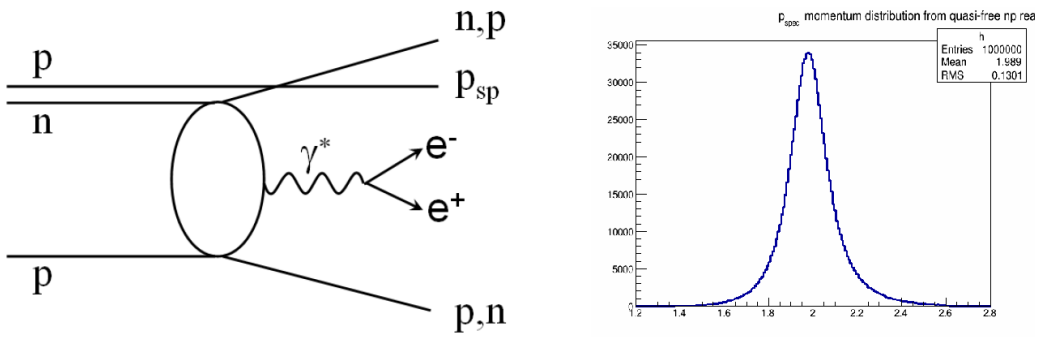

Figure 3.11: Left: Kinematics of the process $d + p \rightarrow pne^+e^-p_{sp}$ within the spectator mechanism. Right: Momentum distribution of the spectator proton p_{sp} from phase-space simulation of quasi free np reaction.

by the Forward-Wall detector, covering forward polar angles up to 7°.

In order to extract the signal corresponding to a deuteron in the FW, a second hit has to be measured. As was mentioned at the beginning of this chapter, the deuteron identification in this detector is a particular challenge. It is crucial to distinguish final states with a deuteron from the ones with an unbound np pair. This task requires additional kinematical constraints to distinguish these particles from the proton background. In this section, a detailed particle identification procedure is described. First, a spectator selection is presented, next, a deuteron selection procedure for the $d + p \rightarrow de^+e^-p_{sp}$ and $d + p \rightarrow d\pi^+\pi^-p_{sp}$ reaction channels.

3.4.1 Proton spectator selection

Spectator selection is based on momentum cut. This information is calculated from the particle time of flight and distance to the detector cell. In addition, it is assumed that spectators are the fastest particles in the reaction because they carry approximately the beam velocity. This assumption leads to the condition that spectator hits are the first hits in the detector. Later, it will be shown that this condition is correct and that in the processes (3.1) or (3.2), the spectators are well separated from deuterons. The momentum is calculated using a proton mass as below:

$$\begin{aligned} \beta &= \frac{L}{T}, \\ p &= M \cdot \sqrt{\frac{1}{\frac{1}{\beta^2} - 1}}. \end{aligned} \tag{3.13}$$

where:
β - particle velocity
L - distance from the target to FW cell

T - particle time of flight measured in FW detector
p - particle momentum
M - particle mass

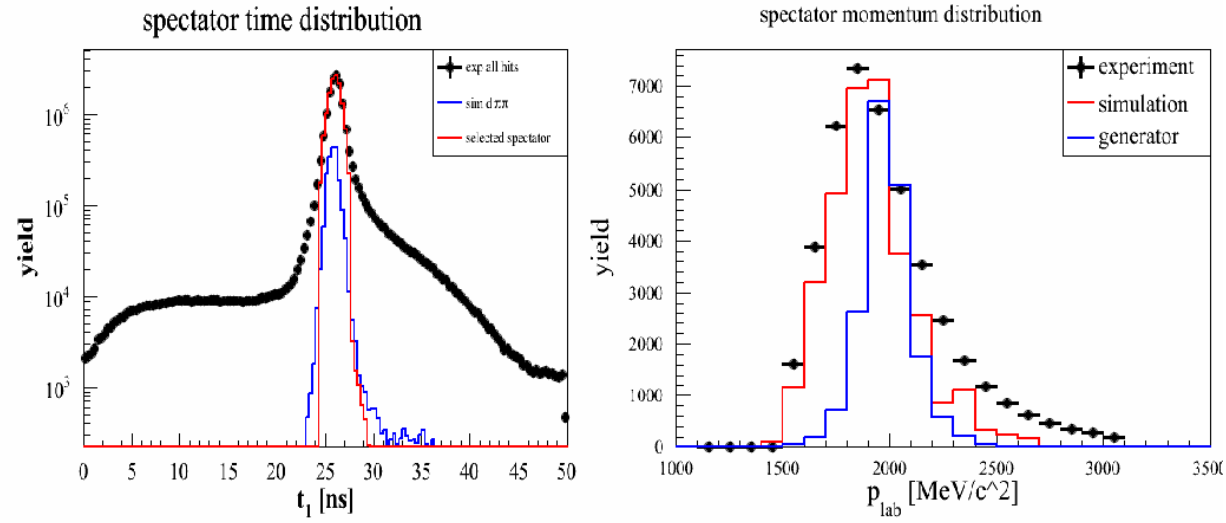

Figure 3.12: Left: Time of flight distribution corresponding to the first hit in FW detector (black dots). The blue line shows the simulation result and the red area shows the selected spectators. Right: Momentum distribution of the spectator proton p_{sp}. Black points represent experimental data, the red line shows PHSP simulation with GEANT package, the blue line shows the result of a simulation without detector influence.

Both time of flight and momentum distributions corresponding to the first hit in FW detector are presented in figure 3.12 for events with a $\pi^+\pi^-$ pair detected in HADES. On the left side, the raw time of flight distribution corresponding to the first hit in the Forward-Wall detector is displayed. Black points show experimental data, while the blue line displays the predicted times for the spectator in the PLUTO simulation, assuming phase space distributions (PHSP). Finally, the simulation, shown as a blue line predicts a narrow peak around 26 ns, which is in agreement with experimental data, shown as black points. In the tails of the spectra, the background, coming from random events, is visible. But its yield is 3 orders of magnitude smaller than peak maximum. On the right panel, the proton momentum distribution is shown. Again, black points represent experimental data, red line shows simulation including FW detector response calculated with GEANT package. The blue line shows ideal spectator momentum without detector influence. It can be noticed that the time of flight resolution induces a significant distorsion of the deuteron momentum distribution. Particles with momentum in the range (1.6 - 2.6 GeV/c) are selected as spectator protons. The time-of-flight distribution of the selected events is indicated as the red line in the left panel of Fig. 3.12.

The best way to check if the momentum condition is sufficient to select spectator protons is to calculate the momentum of the corresponding particles in the deuteron projectile rest frame. Correctly selected spectators should have a momentum distribution consistent with the nucleon momentum distribution inside deuteron. Distribution of the spectator momentum transformed to the deuteron rest frame is presented on figure 3.13.

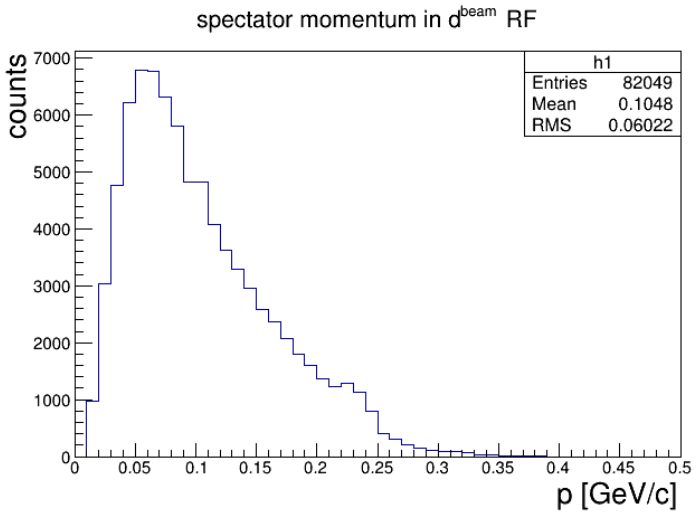

Figure 3.13: Momentum distribution of selected proton spectators in deuteron beam rest frame.

3.4.2 Deuteron identification in FW

Deuteron selection in FW detector is carried out, in a similar manner as spectator selection, based on time of flight selection for the second measured hit. The procedure is similar for the $dp \rightarrow np\pi^+\pi^- + p_{spec}$ and $dp \rightarrow npe^+e^- + p_{spec}$ reactions. It is explained in detail below, taking as an example the case of dipion emission.

Figure 3.14 shows time of flight distribution in FW for the deuteron and proton spectator from $dp \rightarrow d\pi^+\pi^- + p_{spec}$ channel as predicted by the simulation. The respective time of flight distributions from the background process $dp \rightarrow np\pi^+\pi^- + p_{spec}$ is presented, as well. One can see a clear separation between deuteron and spectator, but it can also be seen that the distribution of the proton of the "unbound prcess" overlaps with the one of the deuteron.

The left panel on figure 3.15 shows the distribution of the time of flight t−2 of the second hit in FW when the first hit fulfills the spectator conditions. The presented events

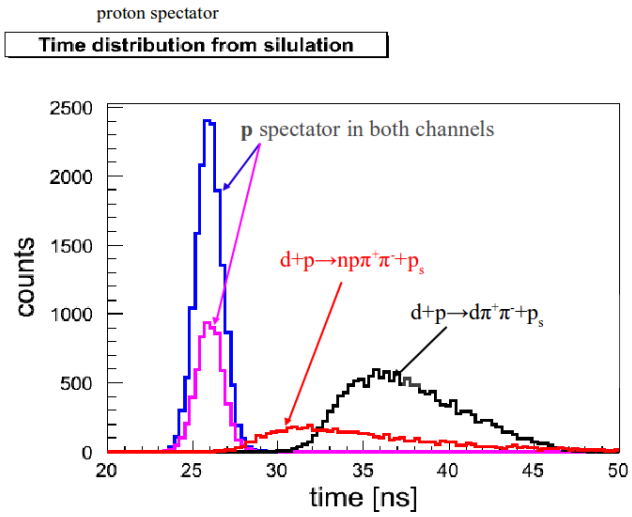

Figure 3.14: Time of flight value for particles in Forward-Wall detector, calculated based on simulations for participant-spectator model

also fullfill the condition that charged pions have been detected in HADES. Data points

show a two hump structure, where the first hump is cut on the left side. This is due to the condition on the first hit momentum, which reflects in a minimum time for the first hit, as shown in fig. 3.12 left, and consequently also on the minimum time for the second hit. Simulations from fig. 3.14 show that deuterons can be expected not before 30 ns. Exactly at this value data points show a minimum and a second peak develops.

To shed more light on the origins of the two peaks in the t_2^{FW} distribution, the differences between the times of the two first hit are presented on the right side of fig. 3.15. From this plot, one can see that the minimum time difference between the spectator proton and the deuteron is 5 ns. It has to be noted that the presented simulation refers to situation when reaction products are distributed according to uniform phase-space coverage. The shape of the distribution can slightly differ in a more realistic model. It is not excluded that the dynamics of the reaction can shift the mean peak position in one or other direction, but the minimal $t_2 - t_1$ value will not change, since it is driven by kinematics.

We can also see that the first peak can not be explained by the contribution of the unbound $dp \to np\pi^+\pi^- p_{spec}$ channel only. A possible explanation of the enhancement at small times of flight is the contamination by the $dp \to dp\pi^+\pi^- p_{spec}$ reaction, where both d and p contribute. Another possible explanation is an effect of cluster splitting inside FW detector. The particles hitting the FW detector often fires few cells at one time. These so-called clusters are considered as one hit as long they are adjacent. If, by chance, one cluster will be split due to unefficient cells, it will be considered as two separate hits with almost the same time of flight and t_2 distribution consistent with the first hump in the experimental spectra.

These effects were however not further investigated, since, as will be seen studied below in more details, the corresponding events can be rejected, using analysis cuts. In a first step, the condition $t_2 - t_1 > 5$ ns is applied.

Nevertheless, from the simulated distributions shown in the right panel of Fig. 3.14, it is clear that the time difference condition can not completely separate protons from the "unbound process" from the deuterons. To remove the proton background, additional kinematic constraint so called "coplanarity cut" is used.

Co-planarity selection.

The FW detector, due to its cellular structure, provides also information about polar and azimuth angles of the detected particles. Using this information together with the momentum calculated from time of flight, the particle track can be reconstructed. Next, starting from the hypothesis that this particle is a deuteron produced in the reactions 3.1 or 3.2, and using the momentum conservation law, an additional kinematic constraints can be formulated as:

$$\overrightarrow{p_d} = \overrightarrow{p_{d'}} + \overrightarrow{p_{\pi^+}} + \overrightarrow{p_{\pi^-}} + \overrightarrow{p_{p_s}};\ \text{or} \quad \overrightarrow{p_d} - \overrightarrow{p_{\pi^+\pi^-}} = \overrightarrow{p_{d'}} + \overrightarrow{p_{p_s}}; \tag{3.14}$$

where $\overrightarrow{p_d}$ is the deuteron beam momentum and $\overrightarrow{p_{\pi^+\pi^-}}$ is the sum of the momenta of the charged pions, which are reconstructed with a very good precision in HADES, $\overrightarrow{p_{d'}}$ and $\overrightarrow{p_{p_s}}$ are momenta of the outgoing deuteron and proton spectator, respectively. However, it can be noted that the relation 3.14 does not depend on the participant-spectator mechanism and only relies on momentum conservation in the $dp \to dp\pi^+\pi^- p_{spec}$ reaction. Now, to simplify the formula, a new vector $\overrightarrow{p_k}$ can be defined as:

$$\overrightarrow{p_k} = \overrightarrow{p_d} - \overrightarrow{p_{\pi^+\pi^-}} \tag{3.15}$$

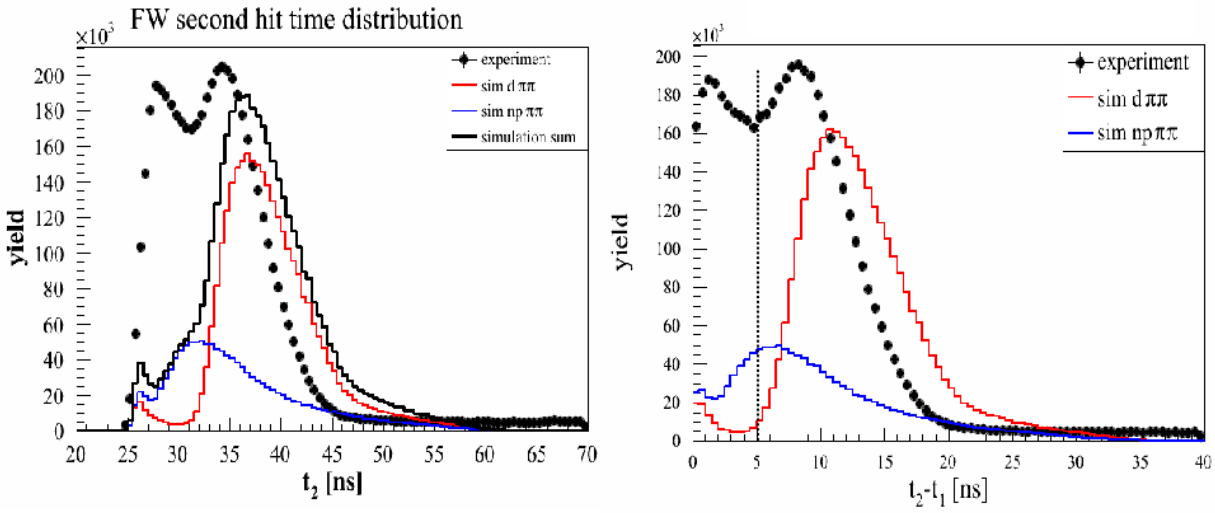

Figure 3.15: **Left:** Time of flight distribution of the second measured hit in the Forward-Wall detector (black dots) compared with simulations for the "fusion" (red histogram) and "unbound" (blue histogram) channels, as well as for the sum of both channels (black histogram). **Right:** Time difference between the second and first hits in Forward-Wall detector. The lines have the same meaning as for the left panel.

and the condition 3.14 becomes:

$$\overrightarrow{p_k} = \overrightarrow{p_{d'}} + \overrightarrow{p_{p_s}} \tag{3.16}$$

The vectors $\overrightarrow{p_k}$, $\overrightarrow{p_{d'}}$, $\overrightarrow{p_{p_s}}$ must lay in one plane and this property can be used as a condition for deuteron selection. For this, a measure of the co-planarity can be defined as the angle between the vector $\overrightarrow{p_k}$ and the cross product of the vectors $\overrightarrow{p_{d'}}$ and $\overrightarrow{p_{p_s}}$:

$$\theta_{coplanarity} = \angle(\overrightarrow{p_k}, \overrightarrow{p_{d'}} \times \overrightarrow{p_{p_s}}) \tag{3.17}$$

For the tracks corresponding to the reaction of interest, the coplanarity $\theta_{coplanarity}$ is expected to be close to 90°. An important advantage of the above definition is that in order to calculate this angle, one only needs to know the directions of the $\overrightarrow{p_{d'}}$ and $\overrightarrow{p_{p_s}}$ vectors and not necessarily the magnitudes. This observable is therefore not affected by the resolution of the FW time-of-flight measurement.

Figure 3.16 shows the coplanarity distributions for both reaction channels $dp \rightarrow d\pi^+\pi^- + p_{spec}$ and $dp \rightarrow np\pi^+\pi^- + p_{spec}$, considered as signal (red line) and background (black line), respectively. Events corresponding to the channel with deuteron in final state shows a narrow peak around 90°, where the width of the peak depends only on the detector resolution. On the other hand, the distribution of events corresponding to background is broad and does not show any peak. Furthermore, considering this distribution in a narrow range around the peak, the background looks almost flat in comparison to the signal. The correlation between the coplanarity and the time of flight distributions of the second FW hit can be studied to further investigate the origin of the two hump structure in the FW time distribution presented in Fig. 3.15. Plotting t_2^{FW} as a function of coplanarity (fig. 3.17) without cut on the time difference, one can see that the first peak in the t_2 time of flight distribution corresponds to a flat distribution of the coplanarity angle. On the other hand, the second peak in time distribution, which has been discussed as a superposition of the deuterons emitted in the fusion process and of the protons emitted in the unbound process, indeed forms a sharp peak on the broad background. Hence, it

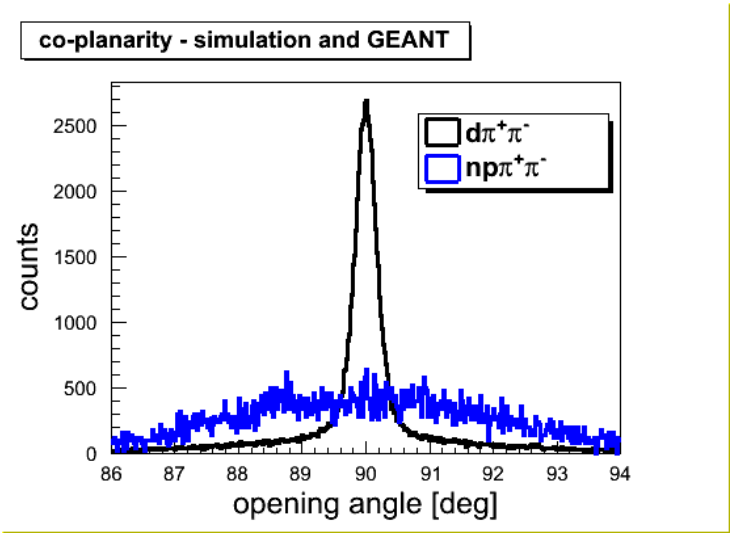

Figure 3.16: coplanarity distribution calculated for both "fusion" and "unbound" reaction channels. The calculations are done based on phase-space simulations including detector models in the GEANT package.

confirms our interpretation of the time of flight spectra.

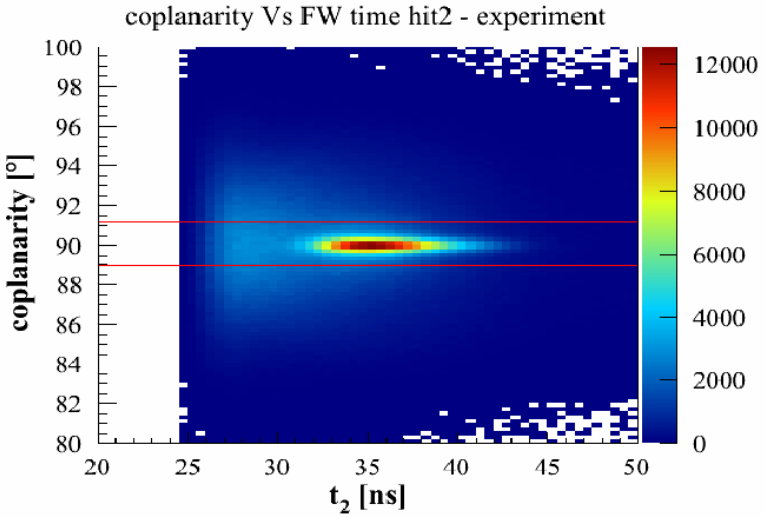

Figure 3.17: Forward-Wall time of the second hit vs. coplanarity. No cut on the t_2-t_1 time difference is applied.

In the case of the dielectron channels, the same time cuts are applied. The coplanarity angle is defined in a similar way as for the dipion channel, by replacing the π^+ and π^- momenta in Eqs. (3.14) to (3.16) by the e^+ and e^- momenta.

Therefore, a selection on the coplanarity can be used to improve the purity of the event selection for both the $d + p \to d\pi^+\pi^- p_{spec}$ and $d + p \to de^+e^- p_{spec}$ when the deuteron is detected in Forward-Wall.

However, in the case of the dielectron channel, the background from the unbound process is much larger than the "fusion" signal, which prevents fr.om a real signal extraction and only an upper limit can be extracted, as will be explained in more details in Sec. 5. We continue in the following with the method of signal extraction for the dipion channel.

In a first attempt to suppress the proton background, the simple following cut has

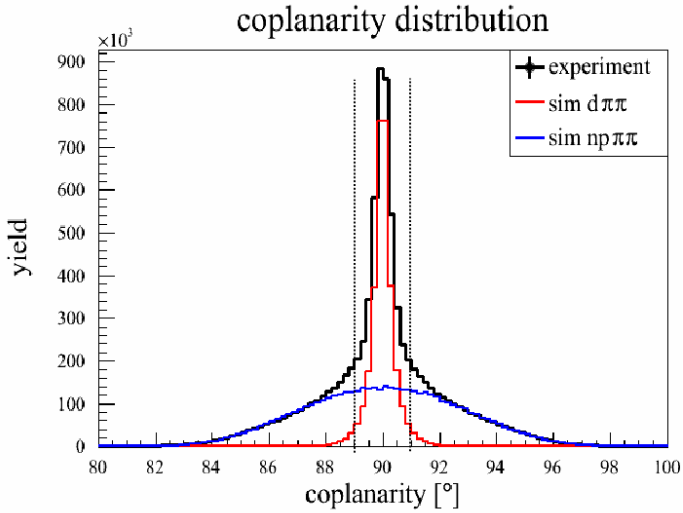

Figure 3.18: Experimental coplanarity distributions for events selected in $d + p \rightarrow d\pi^+\pi^- p_{spec}$ after time of flight cuts. The red and blue lines correspond to GEANT simulations for respectively the "fusion" and "unbound" reaction channels based on a phase-space model and fitted to the experimental distribution.

been used:

$$-1^\circ < \theta_{coplanarity} - 90^\circ < +1^\circ \tag{3.18}$$

This selection is shown as red lines in fig.3.17. However, spectra are still contaminated by the background contributing in the coplanarity range from 89° to 91°. This is illustrated in Figure 3.18 where the experimental coplanarity distribution is compared with GEANT simulations of both $d\pi^+\pi^-$ and $np\pi^+\pi^-$ channels with products distributed according to uniform phase space population.

It can be noticed from this plot that the width of the coplanarity peak is very well reproduced by the simulation, which means that the experimental effects are well under control. The shape of the background is also well reproduced by the simulation, only a weak dependence of this observable with respect to the model used for the unbound process is indeed expected.

The simulated distributions have been fitted to reproduce the experimental yields. One can deduce that, using the selection (3.18), which is displayed as grey lines in Fig. 3.18, there is still around 30% background under the peak. This number is an average, and, as will be seen in the next section, the background contribution has a different distribution from the signal.

3.4.3 Bin by bin background subtraction for the dipion channel

Meanwhile, the high statistics of the two pion production channel allows to subtract the background "bin by bin" for any observable of interest like for example the two-pion invariant mass ($M_{\pi^+\pi^-}$), the total energy in the pn system ($\sqrt{s_{pn}}$), etc.. In this method, for each bin of interest, a corresponding coplanarity distribution is plotted and the background is estimated by the fit procedure described below. Example of the procedure is presented on Fig. 3.19 and Fig. 3.20

In Fig. 3.19, the two-pion invariant mass is presented. Three different colors represent different conditions for event selection. Red points show data where deuterons are selected in Forward-Wall detector only by the condition on the time of flight difference between two registered hits. As was shown in previous sections, this condition is insufficient and

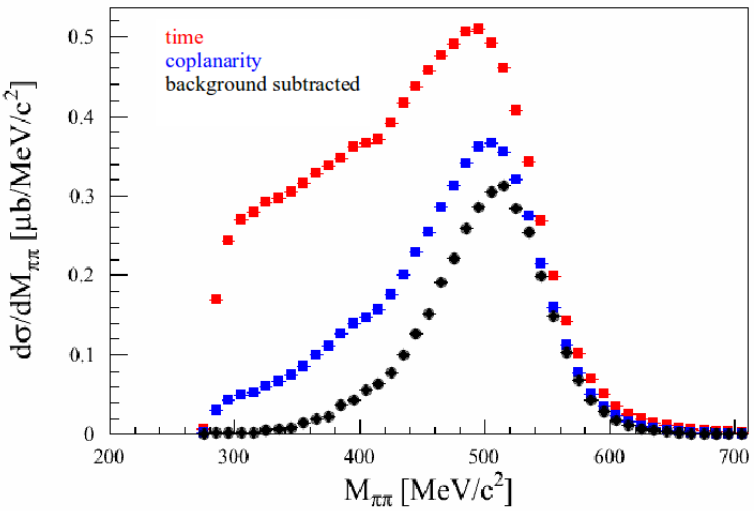

Figure 3.19: Experimental distributions of the two-pion invariant mass from the quasi-free *np* reaction. Red points corresponds to a coarse selection based only on time of flight difference between the deuteron candidate and the spectator proton. Blue points show the influence of the coplanarity cut $\theta = 90° \pm 1°$ in the event selection. Red points represents data after the "bin by bin" background subtraction.

additional steps have to be performed to improve the signal extraction. Blue points show the improvement of the selection by adding a window with a width of 1° around the peak in the coplanarity angle distribution. The effect is especially important in the low $\pi^+\pi^-$ invariant mass region. But, as shown previously, this cut still contains about 30% of proton background.

Next, for each bin of the two pion invariant mass, the coplanarity plots are produced. The plots for different invariant mass regions are shown on Fig. 3.20. The first plot corresponding to $M_{\pi^+\pi^-}$=300-310 MeV/c^2 is completely dominated by the *np* background and no visible peak can be found. The situation starts to change above $M_{\pi^+\pi^-} = 400$ MeV/c^2 , as can be observed in the next plots. In the mass range 410-420 MeV/c^2, already a small coplanarity peak starts to be visible on the still very large background. Finally, in the higher mass region, the peak is dominating the spectra.

The functions fitted to the coplanarity plots have the form:

$$f(x) = \underbrace{A \cdot e^{\left(-\frac{(x-90°)^2}{2\cdot\sigma_1^2}\right)} + B \cdot e^{\left(-\frac{(x-90°)^2}{2\cdot\sigma_2^2}\right)}}_{signal} + \underbrace{C \cdot e^{\left(-\frac{(x-90°)^2}{2\cdot\sigma_3^2}\right)} + D}_{background}, \tag{3.19}$$

where A, B, C, D, σ_1, σ_2, σ_3 are fit parameters. The formula consist of three Gauss functions and a constant part denoted by D letter. A, B, C, are the Gauss function amplitudes and σ_i represents the width of the respective gauss functions. The amplitudes are always restricted by the count number in peak maximum and background region. The two first parts of the formula represent the signal peak, while the last Gaussian and constant terms stand for the flat background contribution. Using the parameters determined for the background from the fit, the signal yield can be calculated as a difference between the total and background yield in the peak region. The final result of this procedure is shown in figure 3.19 (black points).

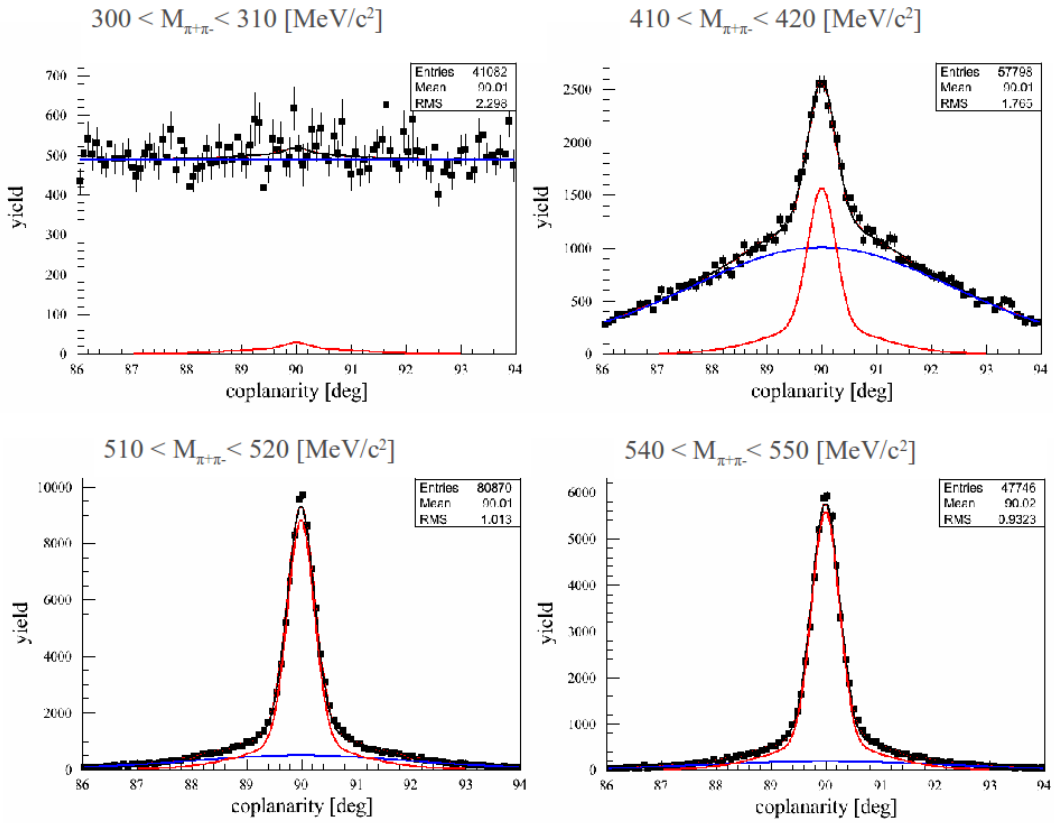

Figure 3.20: Examples of the "bin by bin" background subtraction. On each plot, black points show the experimental coplanarity distribution for four different invariant mass regions. Solid lines shows theoretical distributions fitted to the data. Red and blue lines show the contributions of the signal and background respectively and the total is shown as a black line.

3.5 Forward Wall detector re-calibration

3.5.1 Tests of the particle reconstruction in Forward Wall detector

The calibration of the FW wall had been made previously by adjusting the spectator momentum tot he expected average value $p_{spec} = P_d/2$. This very crude assumption had no influence on the study of inclusive e^+e^- channel, but it is necessary to check it now, since we need to use the deuteron momentum to calculate observables in the exclusive channels, like the $d\pi^+\pi^-$ invariant masses. The quality of the calibration in Forward Wall detector can be tested by missing mass technique. This technique consists of calculating one of the particles from the measurement of other particles in the same event using conservation laws. In these calculations, well defined reaction $d + p$ at $T_k = 2.5GeV/c^2$ and the very good precision of the pion reconstruction inside HADES tracking system is used. First, the proton spectator will be treated as known particle and deuteron will be calculated as missing particle as follows:

$$\underbrace{p_{d'}}_{\text{missing particle}} = \underbrace{p_d}_{\text{beam and target}} - \overbrace{p_{\pi^+\pi^-}}^{\text{pions in HADES}} - \underbrace{p_{p_s}}_{\text{spectator in FW}} \quad ; \tag{3.20}$$

Where p_x represents four-momentum vectors for the respective particles. Figure 3.21

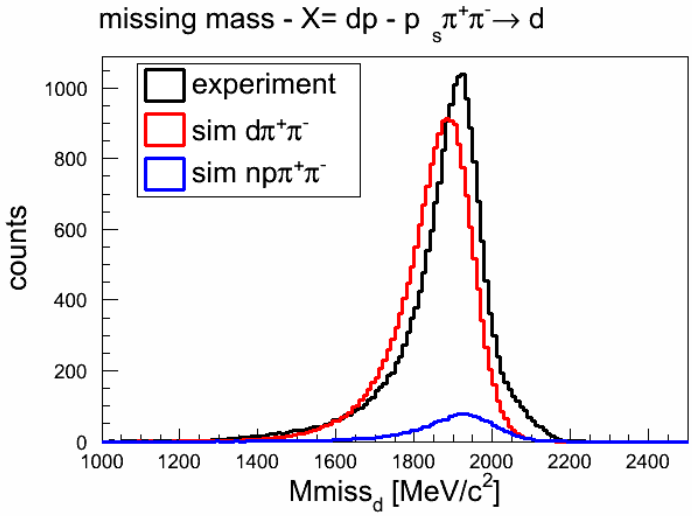

Figure 3.21: Distribution of the missing mass in the $dp \rightarrow p_{spec}\pi^+\pi^- X$ reaction. Data (black histogram) is compared to a simulation of the fusion process (red histogram) and unbound process (blue histogram)

shows the mass distribution of the missing deuteron determined by formula 3.20. On this figure, one can see experimental data marked with black solid line and phase-space simulation channels shown as blue and red lines. All distributions are plotted within coplanarity cut ($90° \pm 1$) but without bin by bin background subtraction. It can be easily observed that the experimental distribution is shifted by around $50 MeV/c^2$ with respect to the simulated $d\pi^+\pi^-$ channel and nominal deuteron mass value which is $M_d = 1875.6 MeV/c^2$. Bigger mass of the object reconstructed as a missing particle can mean that in fact we reconstruct an object with higher mass than deuteron for example unbound $np\pi^+\pi^-$ process where neutron and proton moves with a small relative momentum. However, closer studies of this issue indicated a problem with the Forward Wall time calibration. Similar problem can be indeed observed when the proton spectator is being reconstructed as a missing particle. The above expression can be transformed to calculated missing proton as follows.

$$\underbrace{p_s}_{\text{missing particle}} = \underbrace{p_d}_{\text{beam and target}} - \overbrace{p_{\pi^+\pi^-}}^{\text{pions in HADES}} - \underbrace{p_{p_{d'}}}_{\text{deuteron in FW}} \quad ; \tag{3.21}$$

Here a deuteron is used in calculations to plot missing proton spectator mass as shown in figure 3.22. Again, experimental data shown as black line shows a shift of about $80 MeV/c^2$ with respect to the expected proton mass and the simulation (red line). The bump on the right side of the peak in the data corresponds to the unbound np system what is illustrated on the picture by the simulation of this channel (blue line). Both missing mass plots show necessity of a re-examination of Forward Wall time calibration.

3.5.2 Spectator time re-calibration

Problem of the wrong time calibration of the Forward Wall detector can be observed on left panel of figure 3.23 showing spectator momentum distribution. The blue solid line shows expected spectator momentum distribution coming from the simulation, without effects of the detector resolution (ideal simulation). While black line stands for experimental distribution. From this picture one can see that experimental data has been calibrated in such a way that the average momentum value is equal to the average expected value

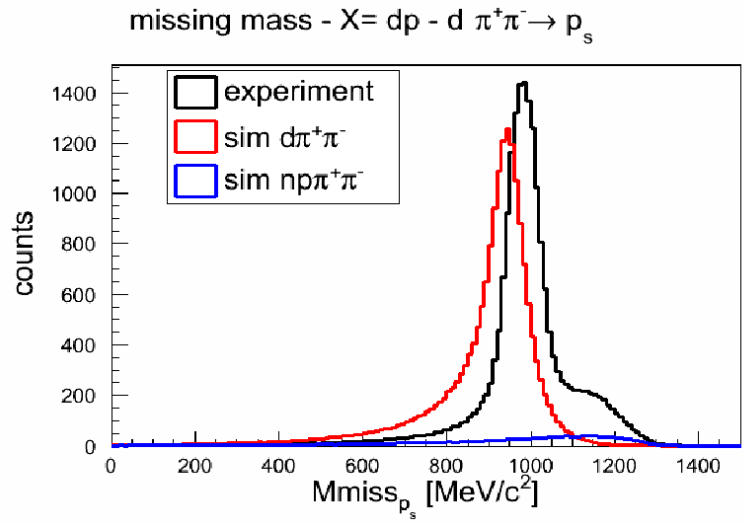

Figure 3.22: Distribution of the missing mass in the $dp \rightarrow p_d\pi^+\pi^-X$ reaction. Data (black histogram) is compared to a simulation of the fusion process (red histogram) and unbound process (blue histogram)

from the ideal model. However, the resolution effects induce a non symmetric shape of the experimental distributions. As a consequence, this procedure is not accurate and data should be equal in peak maximum not in average value as shown by red solid sine (experimental data with global offset $-0.3ns$) which was adjusted to a simulation including all the experimental effects. Right panel of the figure 3.21 shows the effect of the recalibra-

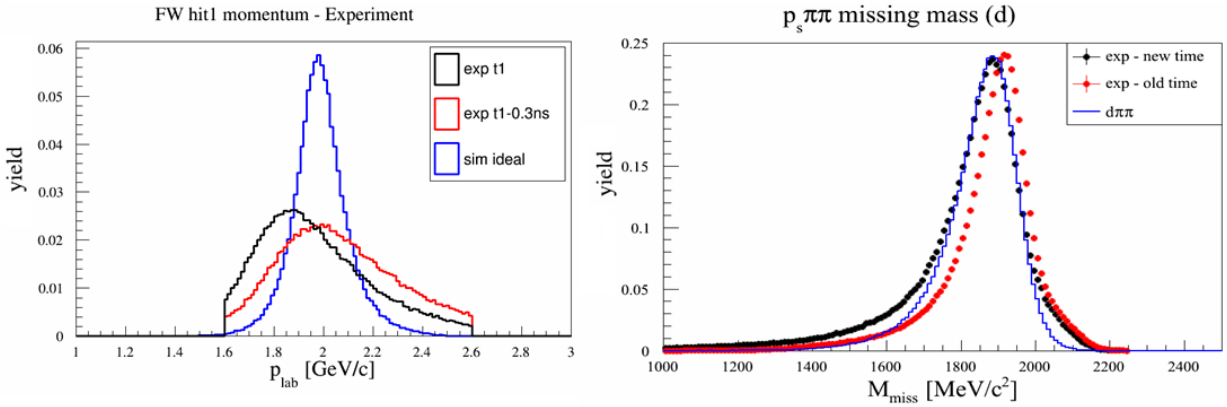

Figure 3.23: Left: Distribution of spectator momentum before (black) and after (red) recallbration) compared to a simple simulation (blue). Right: Distribution of the missing mass in the $dp \rightarrow p_{spec}\pi^+\pi^-X$ reaction after recalibration. Data (black histogram) is compared to a simulation of the fusion process (red histogram) and unbound process (blue histogram)

tion procedure on the deuteron missing mass. Here red points shows experimental data before recalibration and black points stands for experiment with time offset. Blue solid line shows expected missing mass peak from phase-space simulation. One can see that after spectator recalibration procedure, data peak fits simulation very well.

3.5.3 Deuteron time re-calibration

Applying the same offset to the case of the deuteron time of flight in FW does not fix the problem of the missing spectator mass from fig. 3.22. The situation concerning the second hit in forward wall detector identified as deuteron is more complex. Picture 3.24 shows distribution of the spectator missing mass on left panel as a function of the polar angle and on the right panel as a function of the forward Wall cell number. One can see that missing mass is shifted for higher theta angle what corresponds to cells with numbers above 200. In general detector has been calibrated for spectator tagging as discussed previously. At theta angles above 4° spectator-participant model is not valid anymore. In this case events used to calibrate higher detector cells where deuterons or protons participating in the reaction rather than spectators, thus shifting these particles towards expected spectator distributions gave wrong calibration. In this case, again the missing

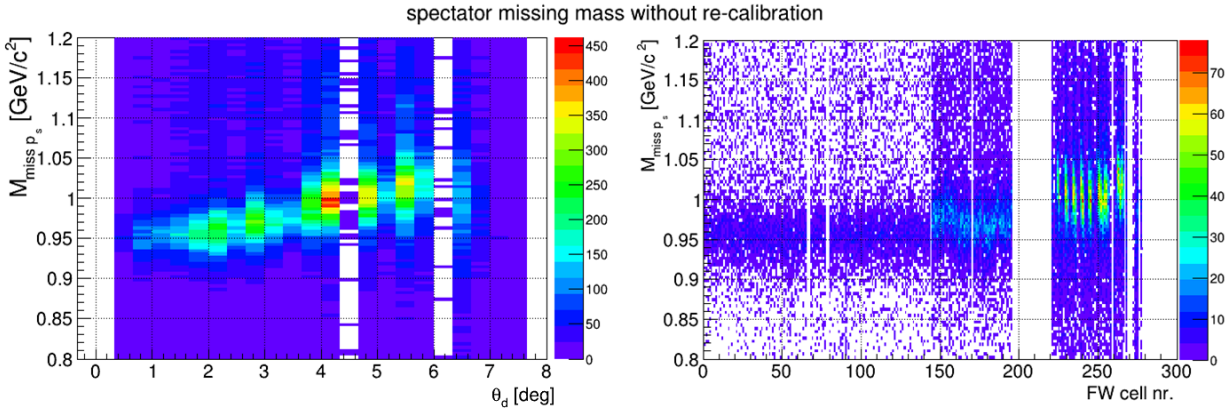

Figure 3.24: Spectator missing mass vs deuteron theta and missing mass vs FW cell number

mass technique can be used. Using 3.20 the proper time of flight of the deuteron has been backward calculated, Next having the new calculated from missing mass time and original time from the detector the time difference ΔT has been plotted for faulty detector cells. This method have been first cross checked on the phase space simulation as shown on figure 3.25. Top panel shows the time difference between calculated time from missing mass and measured time of flight from detector as a function of the cell number. On bottom part of the picture one dimensional histograms of the ΔT for a few example cells are presented. One can see that the ΔT distributions are peaked around 0. What of course is expected in case of the simulation not affected by detector calibration.

The same procedure has been used in case of the experimental data as shown on figure 3.26. Again top part of the picture shows two dimensional histogram of the ΔT as a function of a detector cell number and bottom part shows ΔT distributions for examples cells. Already two dimensional histogram shows clear shift of the ΔT distributions. To precisely determine the mean time difference value for every affected cell a Gauss function have been fitted. As can be seen extracted $\overline{\Delta T}$ parameters are of the order of $+2ns$ for the highest theta regions, these values will be applied as re-calibration parameters.

Results of the data analysis after applying recalibration parameters can be observed on figure 3.27. One can see that the missing mass now are in much better position than before, although some deviations can still be seen. Parameters achieved this way are used in further data analysis. Time manipulations for FWall detector affects the results uncertainty by increasing experimental data error. Discussion on this topic will be done in Sec. 4.2.4.

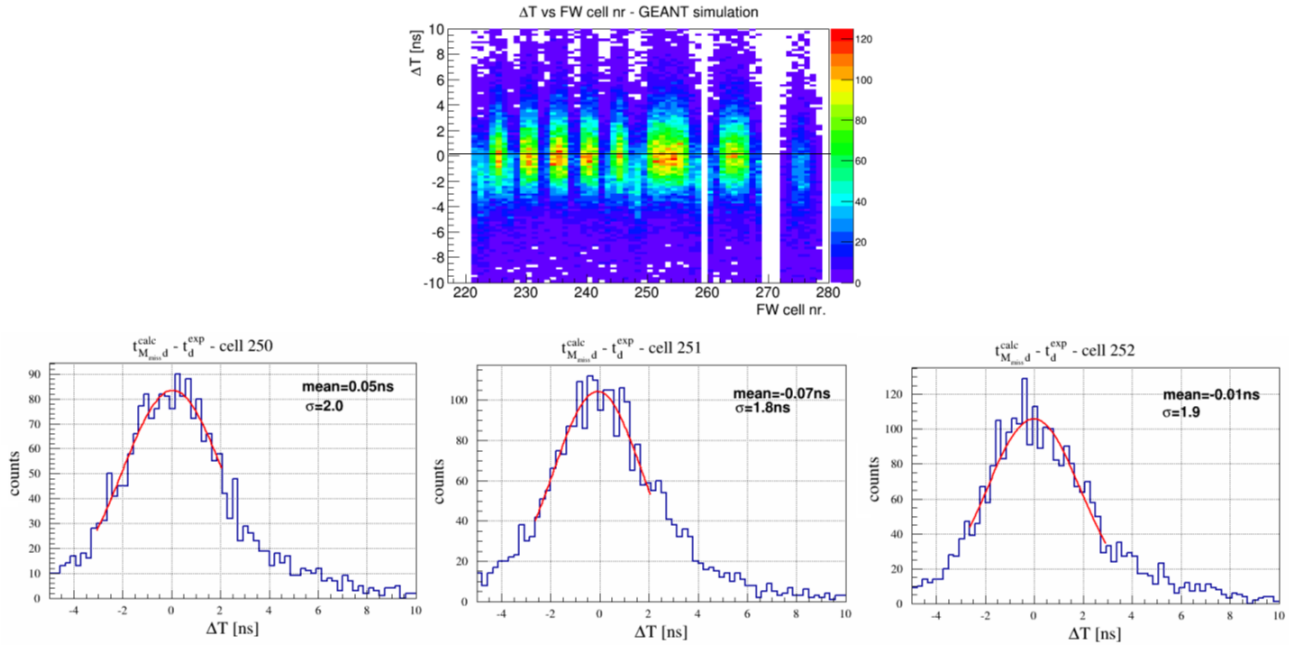

Figure 3.25: Simulatin results Top: difference between calculated (see text) and measured time for the second hit in the FW detector as a function of cell number. Bottom: Distributions of time differences are displayed for three different cells.

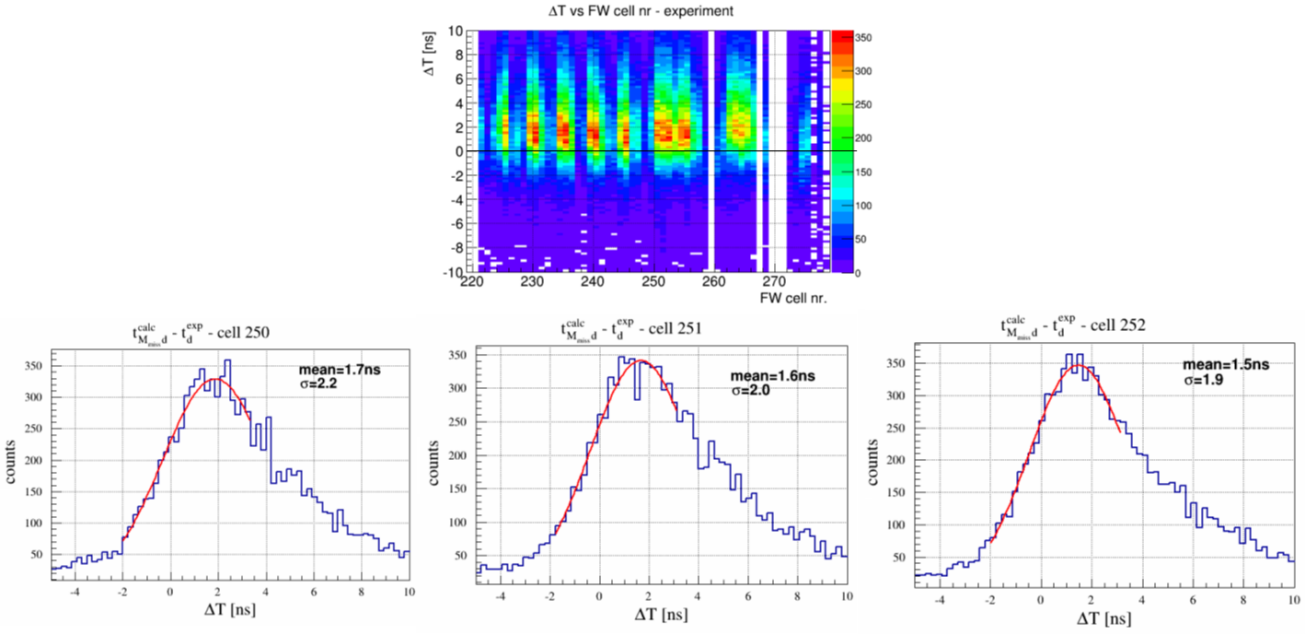

Figure 3.26: Experimental results Top: difference between calculated (see text) and measured time for the second hit in the FW detector as a function of cell number. Bottom: Distributions of time differences are displayed for three different cells.

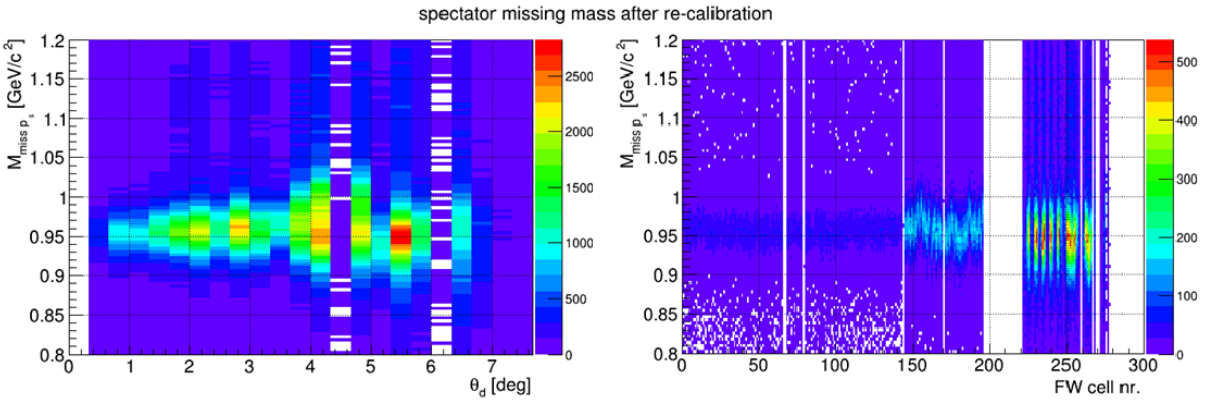

Figure 3.27: Spectator missing mass vs deuteron theta and missing mass vs FW cell number after recalibration

3.6 Elastic pp scattering and data normalization

The number of $p-p$ elastic scattering events from the quasi-free scattering $d+p \rightarrow ppn_{spec}$ collected during the experimental beamtime was used to normalize the experimental spectra and calculate the cross sections, as follows:

$$\frac{\sigma_R}{N_R} = \frac{\sigma_{el}}{N_{el}} \Longrightarrow \sigma_R = N_R \cdot \frac{\sigma_{el}}{N_{el}} \tag{3.22}$$

where:
N_R - yield of reaction channel of interest
σ_R - cross section of reaction channel of interest

The energy and momentum conservation laws provide the following conditions for quasi elastic pp pairs selection from $d+p$ collisions:
i) coplanarity:

$$\mid \phi_1 - \phi_2 \mid \sim 180^\circ \tag{3.23}$$

ii) kinematical constraint:

$$tan(\theta_{p1}) \cdot tan(\theta_{p2}) \sim \frac{1}{\gamma_{cm}^2} = 0.596 \tag{3.24}$$

where ϕ_1, ϕ_2, θ_{p1}, θ_{p2} are azimuthal (ϕ) and polar (θ) angles for measured protons p_1 and p_1; γ_{cm} is the γ Lorentz factor calculated in the center of mass frame. For a fixed kinetic beam energy, one has:

$$E_k = 2\gamma m_{pr} - 2m_{pr} \tag{3.25}$$

where m_{pr} is the mass of the proton.

In the d + p reaction, the incident proton momenta and hence γ are smeared, due to the finite momentum distribution of nucleons known from the wave function describing the nucleons inside the deuterium. Dedicated Monte Carlo simulations with the PLUTO generator show that the observed smearing is well reproduced. The two dimensional distribution of $1/\gamma^2$ vs the difference of proton azimuthal angles, corrected for proton reconstruction efficiency, as will be explained in sec. 3.7, is shown in Fig. 3.28. A two dimensional condition on this distribution (shown as a black square) was set with a width of $2\sigma_{\phi,1/\gamma^2}$, where $\sigma_{\phi,1/\gamma^2}$ was derived from a Gaussian fit to the azimuthal $(\phi_1 - \phi_2)$ and $1/\gamma^2$ distributions.

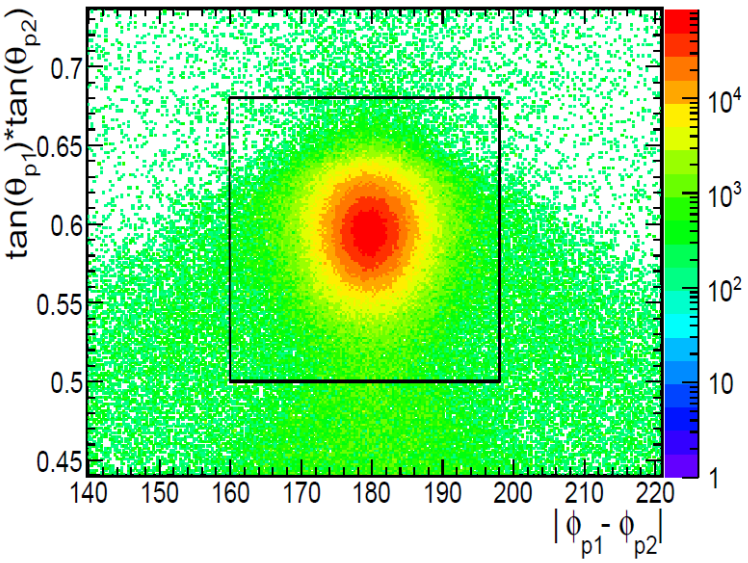

Figure 3.28: $\mid \phi_1 - \phi_2 \mid$ vs. $tan(\theta_{p1}) \cdot tan(\theta_{p2})$. The events placed inside a black square were accepted as coming from elastic scattering collisions.

The elastic scattering yield in HADES acceptance can be easily extracted from experimental data using the kinematical constraints, described above. Then, this yield is corrected for efficiency and acceptance, using the matrices introduced in sec.3.7.

The cross section for the elastic process at kinetic beam energy $E_k = 1.25 GeV/c$ has been taken from the measurement of the EDDA collaboration at COSY synchrotron [65]. In addition, the slight energy dependence of the elastic scattering on center of mass energy spanned by the varying neutron momentum has been included in the simulations.

To perform all these steps, dedicated PLUTO simulations have been performed. This work is described in detail in the PHD of R. Trebacz [54] who estimated the normalization factor and the corresponding uncertainty:

$$\frac{\sigma_{el}}{N_{el}} = (3.84 \pm 0.25) \cdot 10^{-12} \text{ mb} \tag{3.26}$$

where the error includes both: the EDDA measurement error and the error of reconstructed elastic events inside the HADES acceptance.

3.7 Acceptance and Efficiency matrices

Acceptance and Efficiency matrices are mathematical objects which describe the geometrical spectrometer acceptance and the particle reconstruction efficiency. Such objects are generated, separately for every particle of interest (eg. $e^+, e^-, p, d, \pi^+, \pi^-$) via Monte Carlo simulations including precise detector response, track reconstruction and particle identification. Matrices are calculated in functions of the particle momentum, polar and azimuthal emission angles. To create them, "white tracks" are generated in the simulation, which are uniformly distributed over all degrees of freedom in a given range. In addition every event is embedded into a realistic background given by the one measured in the experiment. This procedure allows for a fast comparison of experimental data with different theoretical models, which are usually generated in the full solid angle. To check the correctness of the filtering procedure, self consistency checks are perforems, where the distributions of "white tracks" , used for the calculations, are filtered by the acceptance

and efficiency matrices and compared with the full chain simulation.

3.7.1 Acceptance matrices

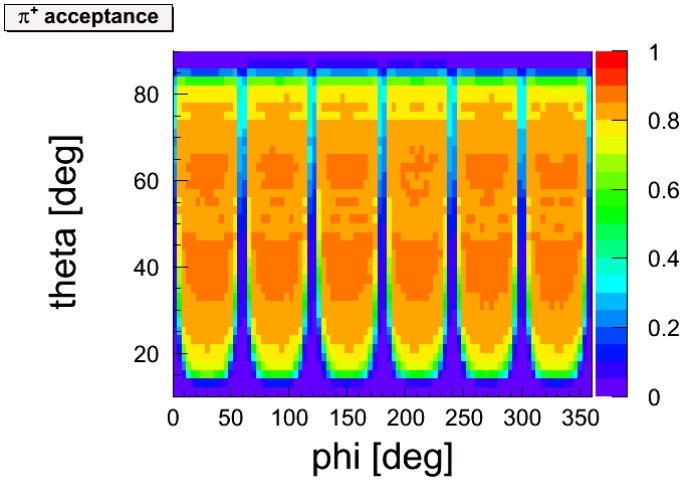

Figure 3.29: Two-dimensional plot of the HADES acceptance for π^+ as a function of polar and azimuthal angle averaged over the momentum.

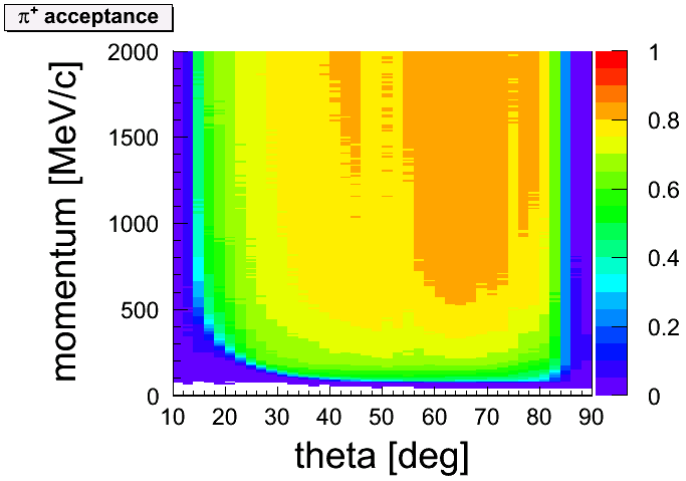

Figure 3.30: Two-dimensional plot of the HADES acceptance for π^+ as a function of the polar angel vs particle averaged over the azimuthal angle

Acceptance matrices account for the effect of HADES acceptance. They are calculated as a ratio between the number of particles which fall into the detector active volume to the number of all simulated particles in the full solid angle. They are calculated as follows:

$$Acc(p,\theta,\phi) = \frac{N_{accepted}(p,\theta,\phi)}{N_{4\pi}(p,\theta,\phi)} \tag{3.27}$$

where:
$N_{accepted}(p,\theta,\phi)$ - number of tracks accepted in the HADES and $N_{4pi}(p,\theta,\phi)$ - number of all simulated tracks, p - particle momentum, θ - particle polar angle, ϕ - particle azimuthal angle.

Acceptance matrices used for the protons, pions and deuterons were calculated by the author of this thesis while the matrices for the electrons and positrons were obtained by

T. Galatyuk [10]. Figures below present, as an example, 2D projections of the acceptance matrices for positive pions.

3.7.2 Efficiency matrices

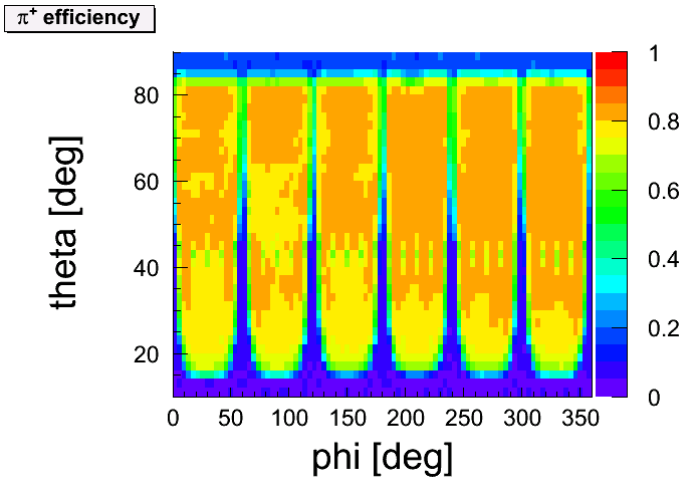

Figure 3.31: Two-dimensional plot of the reconstruction efficiency for positive pions as a function of polar and azimuthal angle averaged over momenta momentum

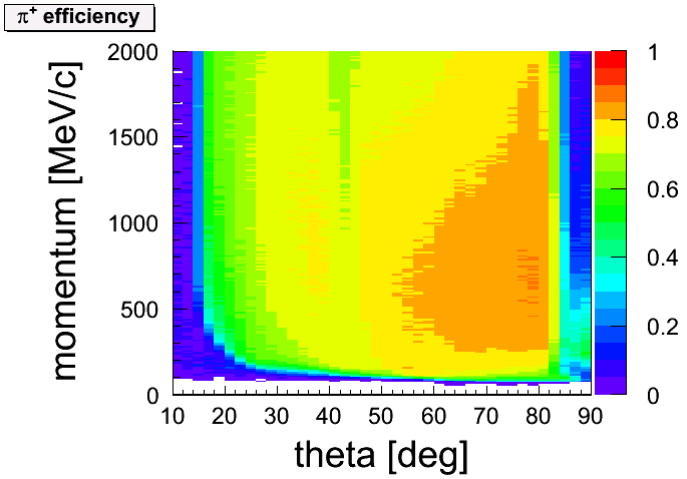

Figure 3.32: Two-dimensional distribution of the reconstruction efficiency for pions as a function of polar angle and momentum integrated over azimuthal emission angle

$$Eff(p,\theta,\phi) = \frac{N_{reconstructed}(p,\theta,\phi)}{N_{accepted}(p,\theta,\phi)} \tag{3.28}$$

where:
$N_{reconstructed}(p,\theta,\phi)$ - number of reconstructed tracks in the HADES detector, $N_{accepted}(p,\theta,\phi)$ - number of accepted tracks. p - particle momentum, θ - particle polar angle, ϕ - particle azimuthal angle.

Using the $Eff(p,\Theta,\Phi)$, the experimental events are corrected for the detector efficiency and track reconstruction efficiency. Result of this corrections are shown for the inclusive e^+e^- invariant mass distribution in Fig 3.33. It can be seen that the average pair efficiency is of the order of 10%.

The uncorrected and corrected invariant mass distributions are shown on the left, while the efficiency correction factor is plotted as a function of the invariant mass in the right part of the figure. The probability that a particle track is fully reconstructed and identified is determined using the ratio of the number of reconstructed particles to the number of particles within the geometrical acceptance of the HADES spectrometer as a function of particle momentum and emission angles:

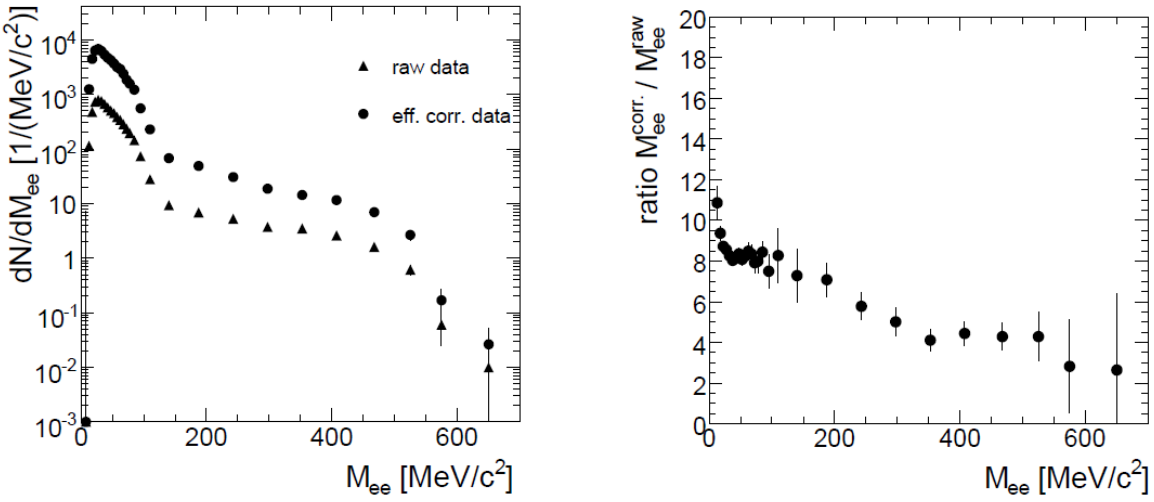

Figure 3.33: **Left:** Invariant mass spectra of signal electron-positron pairs measured in n+p interactions. Black triangles: uncorrected data points, black circles: efficiency corrected data. **Right:** ratio of efficiency corrected to raw data.

Chapter 4

Results for the two-pion production

This chapter describes the analysis results for the exclusive quasi-free $np \to d\pi^+\pi^-$ channel at the $T_k = 1.25 GeV/c^2$ beam kinetic energy. As mentioned in the introduction, the main aim of this analysis is to bring independent experimental constraints to the observations of a dibaryon resonance by the WASA collaboration in the same channel. This work is also complementary to other ongoing analysis in different two-pion production channels in NN collisions with the HADES spectrometer (i.e. $np \to np\pi^+\pi^-$ and $pp \to pp\pi^+\pi^-$).

4.1 Simulation inputs for the $d\pi^+\pi^-$ channel

4.1.1 Theoretical model

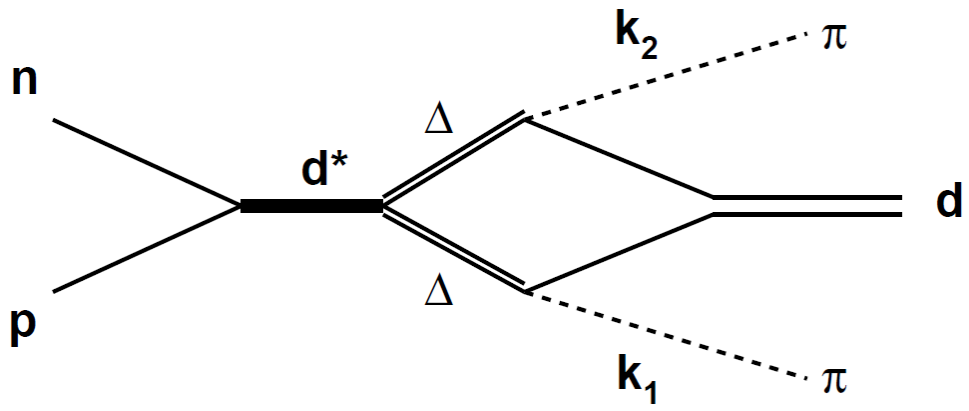

Figure 4.1: Feynman diagram of excitation and decay of the s-channel resonance d^* in the $pn \to d\pi\pi$ reaction.

For the analysis of our data, we will use the dedicated model developped by the WASA collaboration [49] to describe the different isospin channels of the quasi-free $pn \to d\pi\pi$ reaction. Four contributions are taken into account:

- The N(1440) excitation, followed by the decay $N(1440) \to N\pi\pi$
- The N(1520) excitation, followed by the decay $N(1520) \to N\pi\pi$
- The Double $\Delta(1232)$ excitation, followed by the $\Delta(1232) \to N\pi$ decay.

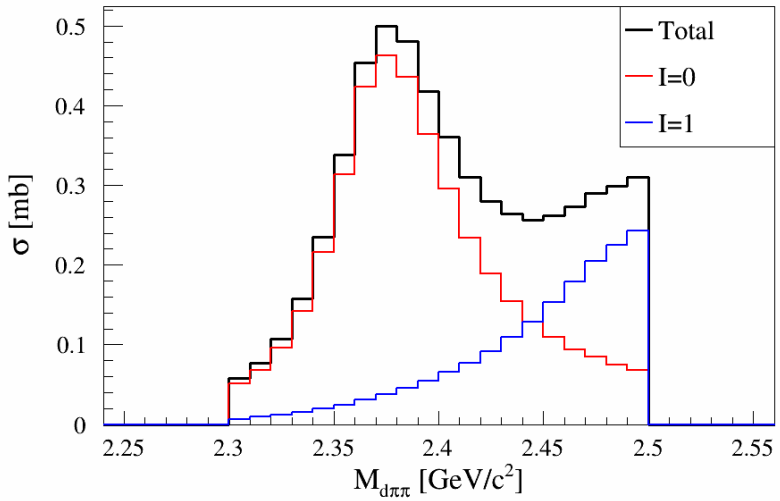

Figure 4.2: ABC resonance toy model decomposed to isospin channel I=0 and I=1. Picture shows relative sum between both channels.

- The excitation of the isoscalar d* resonance, with mass M=2.38 GeV/c^2 and width Γ=70 MeV, which decays as $d^* \rightarrow \Delta(1232)\Delta(1232) \rightarrow NN\pi\pi$

Each process is described using specific propagators and vertex form factors. For the double Δ excitation, the two Δs are considered in relative S-wave. This is justified by the fact that the energy is not far above the $\Delta\Delta$ threshold. The amplitude of this process has been fitted to reproduce the $pn \rightarrow d\pi^0\pi^0$ at $\sqrt{s}$ =2.5 GeV/c^2, where this process is expected to dominate (see fig.1.12).

The N(1440) excitation is assumed to proceed exclusively via σ exchange. For the decay, only the dominant N(1440) decay into the Nσ channel is considered. A S-wave between the N(1440) and the nucleon is assumed, since the reaction is very close to threshold. The amplitude of this process has been ajusted to the calculation of Alvarez-Ruso et al for the $np \rightarrow d\pi^0\pi^0$ reaction [66].

The N(1520) contribution has been added recently to describe the spectra at the highest energies. The double π production proceeds in this case via an intermediate ρ, so it contributes only to channels with the two pions in isospin 1. The d^* included in the model, consists of an s-channel resonance with $I(J^P) = 0(3^+)$, m = 2.37 GeV and Γ = 70 MeV. The Feynman diagram of the $pn \rightarrow d^* \rightarrow \Delta\Delta \rightarrow d\pi\pi$ reaction is presented in fig. 4.1. In the description of the s-channel d* resonance excitation, the two Δs are considered in a s-wave as suggested by the isotropic angular distribution observed in the $np \rightarrow d\pi^0\pi^0$ reaction [49]. A crucial ingredient for this process is the form factor for the $d^* \rightarrow \Delta\Delta$ decay.

$$F(q_{\Delta\Delta}) = \frac{\Lambda^2}{\Lambda^2 + q^2_{\Delta\Delta}/4} \tag{4.1}$$

The cut-off parameter Λ is adjusted to describe the $\pi\pi$ invariant mass. Indeed, the experimental observation of an enhancement at small $\pi\pi$ invariant masses, the so-called ABC effect, associated with the peak of the resonance, as shown in fig.1.13 requires the use of a small form factor (Λ= 0.16 GeV/c^2). Next, reasonable estimates on the different partial widths of this resonance are made to estimate the energy dependence of its contribution in the channel $pn \rightarrow d^* \rightarrow \Delta\Delta$.

The relative phases of the N(1440) and double Δ excitations with respect to the d* resonance process were also fitted to better reproduce the data. This led to difference of phases equal to 0 for the double $\Delta(1232)$ process and equal to 180° for the N(1440)

excitation.

Finally, the neutron momentum in the quasi-free np reaction is taken into account with a deuteron wavefunction based on the CD Bonn potential [67].

In the following, we will call this model "ABC resonance model".

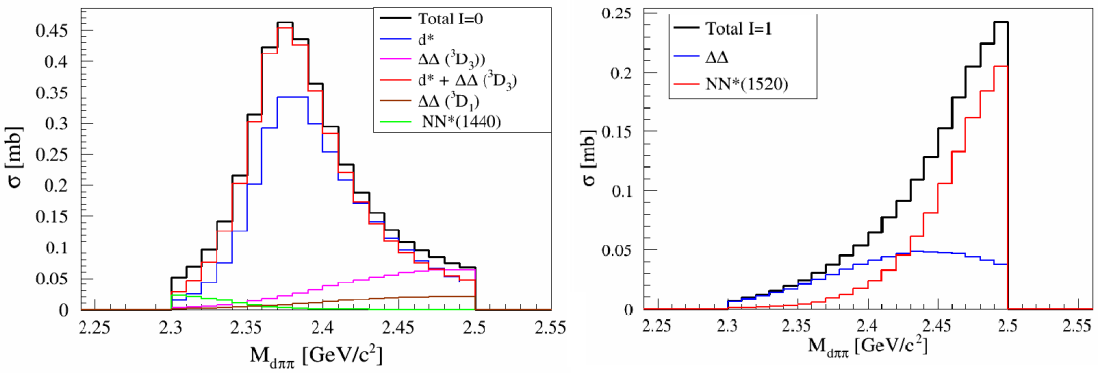

Figure 4.3: Different contributions to the ABC resonance model **Left panel:** isospin channel I=0.**Right panel:** isospin channel I=1

The contributions in the different isospin chanels result from simple isospin relations. In the isospin 1 NN channels, only the double Δ and N(1440) process contribute, while in the isospin 0 channels, the d* resonance is also contributing.

In the case of the pn channel, both isospin 1 and isospin 0 are present. The decomposition of the cross-section of the $pn \to d\pi^+\pi^-$ channel into both isospin components is shown in Figure 4.2 as a function of the pn center of mass energy (or equivalently ($d\pi\pi$ invariant mass). As expected, the isospin 0 component presents a prominent resonant behaviour, due to the dominant contribution of the d* resonance, while the I=1 component is smoothly increasing with increasing available energy.

In fig.4.3, the different contributions can be studied for each isospin case. The case I=1 is simpler since only the double $\Delta(1232)$ and N(1520) excitations have a significant contribution. The respective shapes of these contributions is due to the fact that the N(1520) is excited with a mass below its pole mass, while the two δs can be excited on-shell.

For the I=0 case, the d* resonance contribution strongly dominates in the model and the double $\Delta(1232)$ contribution is significant only for total center of mass energies above 2.47 GeV/c. The contributions of the two different NN partial waves ($^3D_3$ and $^3D_1$) considered for the double Delta process are shown in the pictures. As can be seen on the picture, the former is the most important. One can also notice the constructive interference between the double Δ and d* contributions which has a sizeable effect.

In fig. 4.4, the correlation between the deuterium angle and $\pi\pi$ invariant mass is displayed for simulated events simulated using the ABC model. As already mentioned in sec. 3.2, the deuterons are emitted with angles smaller than 15°. There is a striking difference between the I=1 and I=0 cases. For I=1, which is dominated by the double $\Delta(1232)$ and N(1520) channels, the two pions are emitted with a large invariant mass, close to the kinematical limit for a given deuterium angle. For I=0, there is a strong contribution for the small $\pi\pi$ invariant masses. This is the direct effect of the cut-off in the vertex form factor mentioned above.

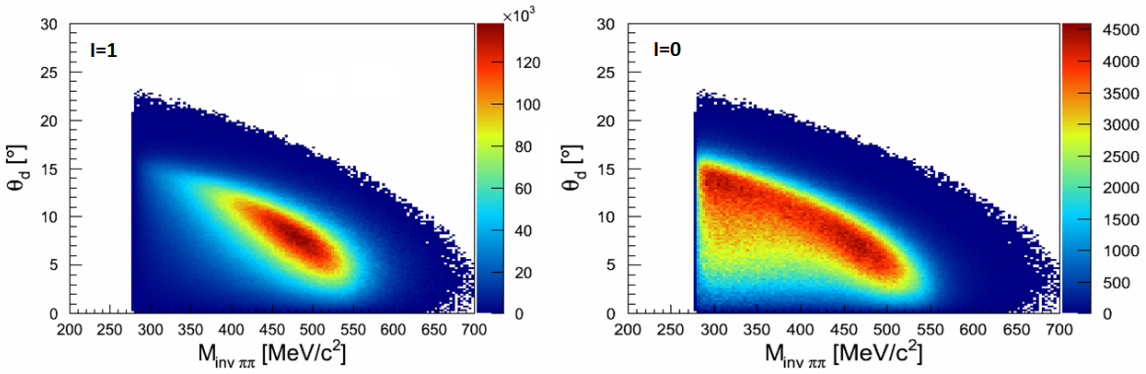

Figure 4.4: Distribution of the pion invariant mass vs deuteron theta from ABC model. Left: I=1. Right I=0

4.1.2 Extraction of cross section for the quasi-free np reaction from the measurement in the dp reaction

Using a deuterium beam allows for the investigation of the np reaction at different center of mass energies, depending on the momentum of the neutron in the deuterium. To extract the dependence of the np cross section as a function of the energy, a transformation (or unfolding) from the dp reaction to the np process has to be applied. The cross section σ_{dp} of a given channel in the dp reaction at a given incident deuteron energy can be related to the cross section in the np reaction using the participant-spectator model.

$$\sigma_{dp} = \int \sigma_{pn}(\sqrt{s_{pn}})\rho(\sqrt{s_{pn}})d\sqrt{s_{pn}} \tag{4.2}$$

where $\rho(\sqrt{s_{pn}})$ is the probability density function to find a pn pair with the total center of mass energy $\sqrt{s_{pn}}$, with normalization

$$\int \rho(\sqrt{s_{pn}})d\sqrt{s_{pn}} = 1 \tag{4.3}$$

and $\sigma_{pn}(\sqrt{s_{pn}})$ is the cross section of the pn reaction at the corresponding center of mass energy.

The dp cross section can then be divided in narrow bins in $\sqrt{s_{pn}}$ of width $\Delta\sqrt{s_{pn}}$ such that one can consider $\sigma_{pn}(\sqrt{s_{pn}})$ to be constant. The dp cross section in the given bin can be written as follows:

$$\frac{\Delta\sigma_{dp}(\sqrt{s_{pn}})}{\Delta\sqrt{s_{pn}}}\Delta\sqrt{s_{pn}} = \sigma_{pn}(\sqrt{s_{pn}})P(s_{pn}, \Delta\sqrt{s_{pn}}) \tag{4.4}$$

where

$$P(s_{pn}, \Delta\sqrt{s_{pn}}) = \int_{\Delta\sqrt{s_{pn}}} \rho(\sqrt{s_{pn}})d\sqrt{s_{pn}} \tag{4.5}$$

is the probability of the pn center of mass energy to be in a bin of width $\Delta\sqrt{s_{pn}}$ around $\sqrt{s_{pn}}$. This probability can be deduced, as shown later, from the $\sqrt{s_{pn}}$ distribution in the simulation of the $d+p$ process in the participant-spectator model.
If the bin in $\sqrt{s_{pn}}$ is small enough and $\rho(\sqrt{s_{pn}})$ can be considered constant inside the bin, one has

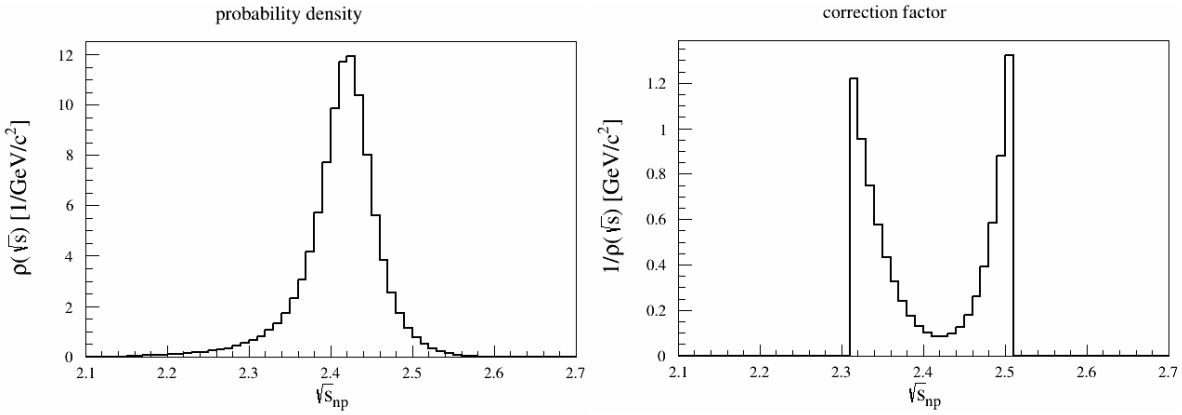

Figure 4.5: Left panel:Probability density $\rho(\sqrt{s_{pn}})$ of the np center of mass energy in the dp collisions at an incident energy of 2.5 GeV. Right panel: Correction factor $f(\sqrt{s_{pn}})$ taking into account the neutron momentum distribution and used for the calculation of the corss section for the np reaction.

$$P(s_{pn}, \Delta\sqrt{s_{pn}}) = \rho(\sqrt{s_{pn}}) \times \Delta\sqrt{s_{pn}} \tag{4.6}$$

and Eq. 4.4 can be re-written as:

$$\Delta\sigma_{dp}(\sqrt{s_{pn}}) = \sigma_{pn}(\sqrt{s_{pn}}) \times \rho(\sqrt{s_{pn}}) \times \Delta\sqrt{s_{pn}} \tag{4.7}$$

or

$$\sigma_{pn}(\sqrt{s_{pn}}) = f(\sqrt{s_{pn}}) \times \frac{\Delta\sigma_{dp}(\sqrt{s_{pn}})}{\Delta\sqrt{s_{pn}}} \tag{4.8}$$

where

$$f(\sqrt{s_{pn}}) = \frac{1}{\rho(\sqrt{s_{pn}})} \tag{4.9}$$

is the correction factor to be applied to the differential cross-section measured in the dp reaction at a pn center of mass energy $\sqrt{s_{pn}}$ to obtain the corresponding cross section in the pn reaction.

In fig. 4.5, both the probability density (left) and the correction factor (right) are shown as a function of the pn center of mass energy. The distributions for the $dp \to d\pi^+\pi^- + p_{spec}$ reaction, have been obtained using the participant-spectator model+phase space, including nucleon momentum distributions inside the deuterium nucleus. The probability density function is peaked at the most probable value of the pn center of mass energy, which is slightly below the maximum of the resonance. The transformation given by Eq. 4.8 can be tested using the simulation of the resonance production provided by the WASA collaboration which is presented in the next section.

Finally, we would like to mention that the procedure described above was also used for the extraction of the np cross sections in the case of the WASA experiment, where a deuterium target was used.

4.1.3 Model normalization

The results shown in the Fig. 4.6 present the distribution of the total center of mass energy of the pn system obtained from dp reaction (left) at an incident energy 2.5 GeV. The right panel shows the unfolded excitation function of the pn reaction obtained by the transformation 4.8. One should note that the distribution of the total center of mass

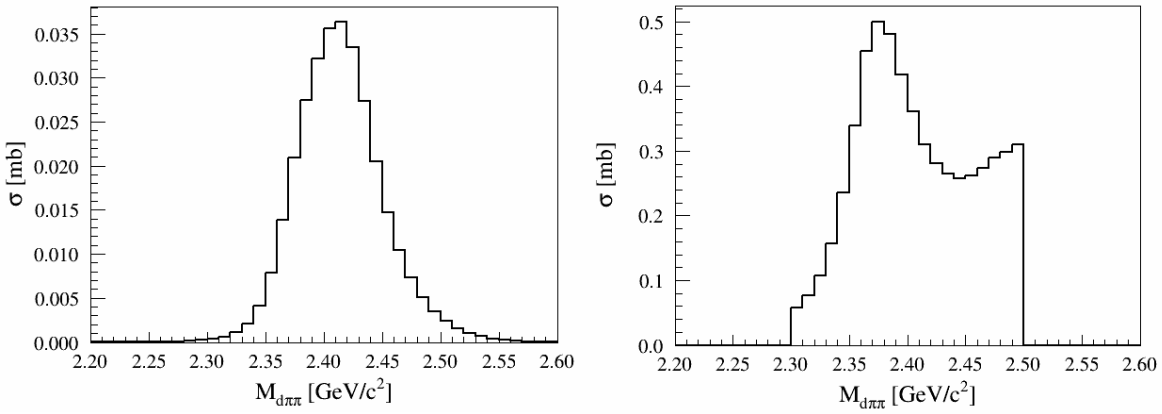

Figure 4.6: Left: Distribution of pn center of mass energy $\sqrt{s_{pn}}$ obtained from the simulation with the ABC-resonance. Right: Cross-section value for the pn reaction as a function of the pn center of mass energy, as derived from the unfolding procedure (see text).

energy is nothing else than the invariant mass of the final state deuteron-dipion system. The prominent peak signaling the resonance excitation is, as expected, clearly visible in the unfolded distribution. The shape of this distribution is identical to the one shown in the bottom panel of Fig. 1.14 and in fig.4.2. This result can be taken as a consistency check of the unfolding procedure. The cross sections of the ABC-resonance model are normalized to reproduce the WASA data. The events are simulated in the full solid angle with a total yield N_{sim}. The relative normalization between isospin I=0 and I=1 channels by means of dedicated weight factors propagated in the event files. The global normalization of the simulation can be easily obtained using the bottom panel of Fig. 1.14. The normalization factor K is simply deduced by

$$K = \frac{\sigma_{pn}(\sqrt{s_{pn}})}{N_{corr}^{sim}(\sqrt{s_{pn}})} \tag{4.10}$$

,where $\sigma_{pn}(\sqrt{s_{pn}})$ is the value of the cross section at a given $\sqrt{s_{pn}}$.

4.2 Experimental data results in comparison to the theoretical model

In this section, experimental data will be compared with the simulation including ABC-resonance model. In addition phase-space simulation will be used as a reference to the presented spectra.

Following event selection procedure described in sec. 3.3 and sec.3.4, a quasi-free $np \rightarrow d\pi^+\pi^-$ reaction channel can be selected by conditions on FW hits. The most technical part of the procedure is the bin by bin subtraction of the background inthe case of detection of deuteron in FW, using the coplanarity criterium form Eq.3.4.3. The efficiency corrections and normalization of the experimental spectra have been discussed in sec.3.7 and 3.6, respectively, whereas the simulation normalization was the topic of previous section (4.1.3).

All the spectra shown in the following are within HADES acceptance.

4.2.1 Kinematical considerations

As already mentioned before, there are two different cases for the deuteron detection. The first, correponding to the deuterons emitted at low polar angles i.e. $\theta < 7°$, detected in

FW, and the second when deuterons are emitted at $\theta > 15°$, and are detected in HADES. One should mention that HADES acceptance is complementary to the acceptance of WASA detector, where deuterons are detected in the angular region between 18° and 3°.

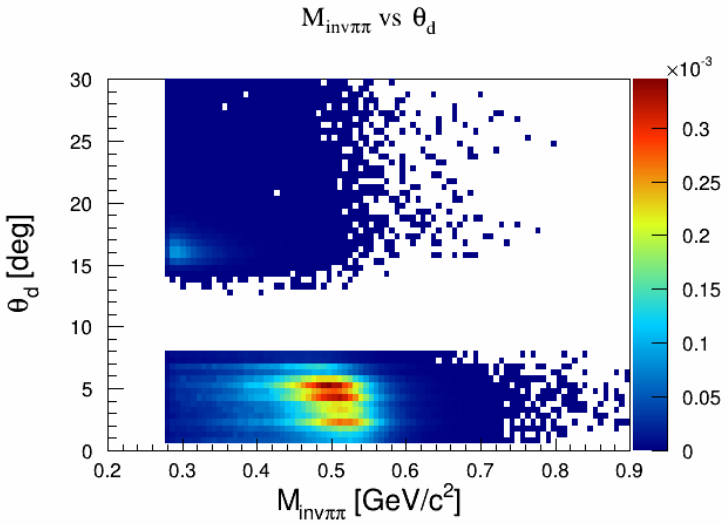

Figure 4.7: Two-pion invariant mass vs. deuteron polar angle θ_d distribution. The two separated regions correspond to the two analysis scenarii with deuteron in HADES $\theta_d > 15°$ and in Forward-Wall $\theta_d < 7°$.

The figure 4.7 shows the distribution of invariant mass as a function of the $\pi\pi$ invariant mass for the two analysis regions. It has to be compared to the similar picture obtained for the simulation in 4π (Fig. 4.4). As can be seen, our acceptance is more suited to detect the highest $\pi\pi$ invariant masses, for which the deuteron is emitted at forward angles. For smaller invariant masses, a broader region of deuterium angles is allowed kinematically, a large part of which can not be seen by our experimental set-up. The detection of the deuteron in HADES corresponds to the very end of the kinematically allowed region, but still some yield is observed, which will motivate further investigations, as shown below.

However, it is expected that more information will come from the detection of the deuteron in HADES. Since our main goal is to check the contribution from the hypothetical dibaryon, one relevant question is the effect of the acceptance cuts on this contribution. Indeeed, since the dibaryon contribution produces $\pi^+\pi^-$ pairs with small invariant masses, i.e. with a broad deuteron angular distribution, a fraction will be cut by the condition of detection of the deuteron in FW (see Fig. 4.4). To show more quantitatively the effect of the acceptance cuts, we present in fig. 4.8, the different contributions to the total np cross section, after acceptance cuts. This picture has to be compared to fig. 4.3, where a similar information was given in 4π. It can be observed that the relative contribution of the d* resonance is much lower than in the original distribution in 4π. However, the resonant peak is still very clear at the smallest $\sqrt{s}$. At large $\sqrt{s}$, the yield is dominated by the N(1520) contribution.

4.2.2 Distributions of *np* center of mass energies

Detecting all final state particles one can reconstruct total energy $\sqrt{s_{pn}}$ of the incident *np* system. Simple estimations, coming from the known masses of the proton and neutron and known incident beam energy, gives $\sqrt{s_{pn}} = 2.42$ GeV. However, due to the extra momentum carried by the neutron inside deuteron (quasi-free reaction) the observed total energy is being smeared around this nominal value. Since we detect all particles from the

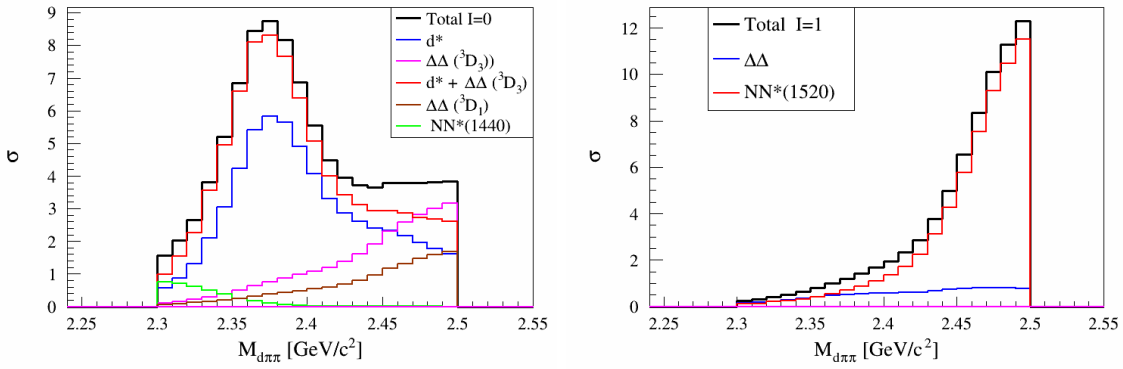

Figure 4.8: Cross section for the np→ $d\pi^+\pi^-$ reaction inside the acceptance, in the case of detection of deuteron in FW. Left part: the different contributions to the I=0 channel are compared to the data. Right part: same for the I=1 channel

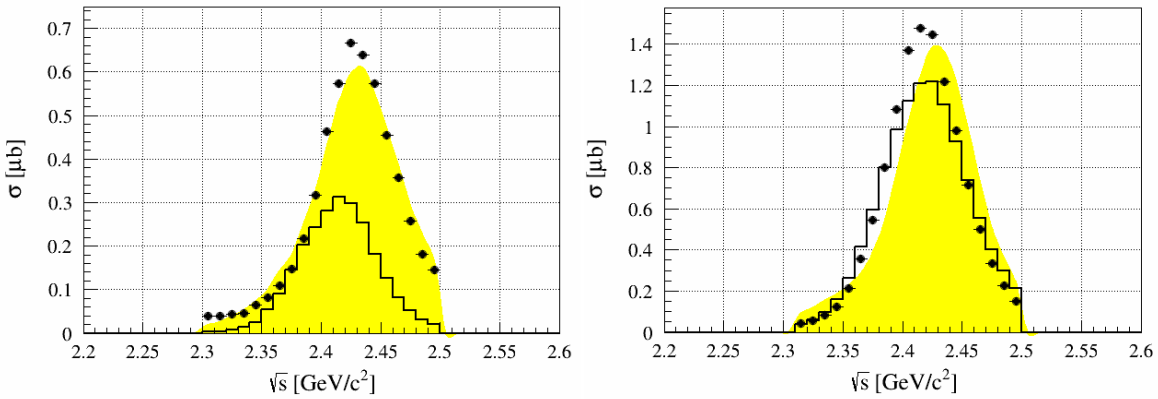

Figure 4.9: Total energy $\sqrt{s_{pn}}$ distribution of the quasi-free np reaction. Left panel: The scenario with deuteron detection together with pions in HADES acceptance. Right panel: The scenario where pions are detected in HADES and deuteron is being reconstructed in the Forward-Wall hodoscope. Black points represents experimental data, solid black line shows ABC resonance model and yellow area is a $dp \rightarrow d\pi^+\pi^- p_{spectator}$ phase-space simulation. Presented results are corrected for the reconstruction efficiency, but inside detector acceptance. Experimental points are normalized to the pp elastic scattering.

final state, a $\sqrt{s}$ for the pn initial state can be deduced as an invariant mass of all outgoing particles, except spectator proton (i.e $d\pi^+\pi^-$ invariant mass).

The $\sqrt{s}$ distribution is shown on the fig. 4.9. Experimental data are presented as black points, simulated ABC-resonance model is shown as black solid line and yellow area represents phase-space simulation. The left panel shows the case when the deuterons are detected in HADES and the right panel presents the situation when the deuteron s are detected in the Forward-Wall detector. Experimental data are normalized to the pp elastic scattering and the cross section in the model is normalized to the WASA data as previously explained.

As explained in sec. 4.1.2, in the general case, this distribution is a convolution of the pn cross section, which is a function of the np center of mass energy $\sqrt{s}$, with the distribution of the $\sqrt{s}$, due to the neutron momentum inside the deuteron. In the case of the model, one can observe a small shift towards smaller $\sqrt{s}$ values.

We start the discussion with the case when all particles are detected inside HADES (fig. 4.9 left panel). In this situation, the experimental is in good agreement with phase

space simulation. On the other hand, the data seem to disfavour the resonance model. Indeed the yield is underestimated by the model. In addition, the maximum of the predicted distribution is shifted to lower $\sqrt{s}$ values. However, one should keep in mind that these data are obtained for a very narrow angular region, corresponding to the edge of the phase space and that this angular region was not covered by the WASA detector, so the model is probably not optimized for this region. In addition, since this region is at the kinematical limit for the quasi-free $np \rightarrow d\pi^+\pi^-$ process (see fig. 4.4). Despite the fact that we apply strict kinematical conditions to the "spectator" proton, the yield in this region is probably very sensitive to the contribution of "dissipative processes", where the "spectator" proton has lost part of his energy. to the benefit of the pn system. In this case, the phase space for the deuteron emission is indeed expected to be broader and larger deuteron emission angles can be reached. It is therefore difficult to draw conclusions about the ABC resonance model from the detection of the deuteron in HADES.

The second case, when the deuteron is detected in the Forward-Wall hodoscope (fig. 4.9 right panel) shows a different situation. In this case, the experimental distribution agrees both in shape and in magnitude with the ABC model. On the other hand, the data are slightly shifted towards lower center of mass energies (or $d\pi^+\pi^-$ invariant masses) with respect to the phase space model. Since, there is no energy-dependence of the amplitude in the phase space model, this small shift could be interpreted as a higher cross section for the smallest pn center of mass energies, as predicted by the ABC model. It is tempting to conclude that this an indication of the resonance formation, as observed by WASA, however, the shift is very small and one should investigate all possible origins of this shift before drawing such a conclusion.

4.2.3 Extraction of the cross section for the np reaction

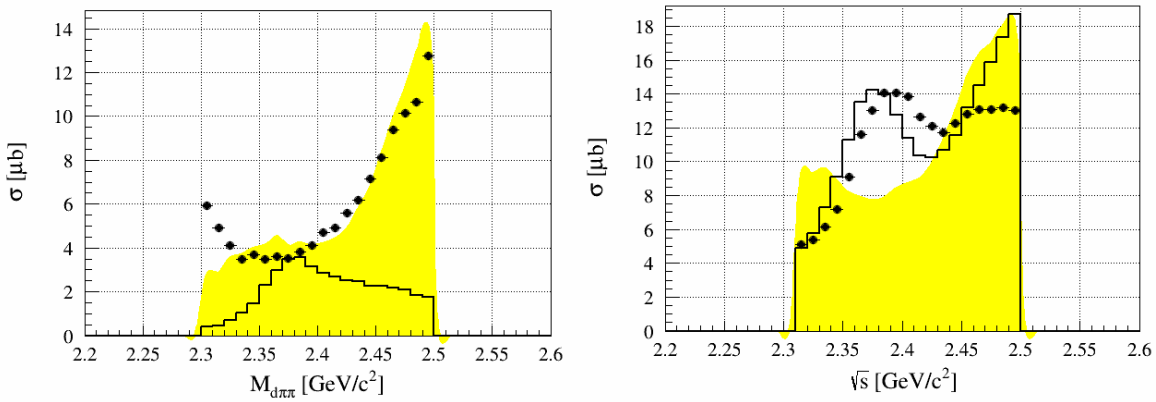

Figure 4.10: Result of the unfolding procedure for the total energy $\sqrt{s}$ distribution of the np reaction. Left panel: The scenario with deuteron detection together with pions in HADES acceptance. Right panel: The scenario where pions are detected in HADES with high precision and deuteron is being reconstructed in Forward-Wall hodoscope. Black points represents experimental data and solid black line shows ABC resonance model.

We continue our study and perform the unfolding procedure expressed by Eq.4.8 in order to obtain the cross section for the np process. Figure 4.10 shows the result after applying the correction factor on the quasi-free spectra. Again, the black points represent the experimental results, the black solid line shows the model prediction and the yellow area stands for phase-space simulations. The left and right panels present the two cases with deuteron detected at high and low polar angles, respectively. As one can see from

both left and right parts of fig. 4.10, the shapes of the phase space and ABC model distributions are completely different. The ABC model shows a peak due to the di-baryon resonance, while experimental data show a shallow minimum at the resonance position.

One should first realize that the specific shape of the phase space distribution is just an artefact of the unfolding procedure. Indeed, for the phase space model, we expect constant cross sections as a function of the *pn* energy. This means that this unfolding procedure, which was validated for ideal 4π simulation, is sesnsitive to experimental effects (mainly resolution) and does not allow to retrieve a *pn* cross section. This could already be noticed by comparing the $\sqrt{s}$ distribution resulting from the simulated events from the phase space model in the detector acceptance fig.4.9 to the initial distribution, due only to the deuteron wave function (yellow areas in Figs.4.9 left and right). Indeed the first one peaks at about 2.43 GeV/c^2, while the second one peaks at about 2.415 GeV/c^2. One can also notice that the distributions are slightly different when all particles are detected in HADES (left part of Fig.4.9) and when the deuteron is detected in the FW (left part of Fig.4.9).

A more reliable method to extract this "pn cross section" would be to adopt an iterative procedure, where the pn cross section used as an input to the simulation would be fitted to reproduce the data. Such a procedure could not be realized during the time scale of this PhD

However, although the procedure that was followed here cannot really extract a "pn cross section", this transformation can still be used to compare the data to the simulation. The advantage is that the dibaryon peak shows up in the simulation using the ABC model and it is interesting to see if the data present a similar behavior.

This is checked in Fig. 4.10, where the data are shown as black points. When all particles are detected in HADES, the data present the same shallow minimum as the phase space simulation, while when the deuteron is detected in HADES, a peak appears at a $\sqrt{s}$ value equal to 2.37 GeV/c^2, slightly below the peak of the structure obtained for the ABC simulation model, which peaks at about 2.385 GeV/c^2.

The presence of the peak in our data after the deconvolution procedure is striking. However, if we go back to the right part of fig. 4.9, we then have to remind that this peak is just the reflect of a very small shift in the $d\pi^+\pi^-$ invariant mass distribution. We would therefore like to stay cautious and conclude that, although our data are in reasonable agreement with the model including the dibaryon resonance, we cannot unambiguously conclude on its existence and that further checks of the sensitivity of the $\sqrt{s}$ distribution would be needed before drawing conclusions.

In the next section, we test the sensitivity of this distribution to the FW calibration

4.2.4 Uncertainty of the results induced by Forward Wall recalibration.

Since the interpretation of the data measured in the quasi-free pn reaction in terms of *pn* cross section rely on the $\sqrt{s}$ differential cross-section, it is important to check the sensitivity of this spectrum to different experimental effects. It seems natural that this spectrum could be sensitive to the FW calibration, which was performed, as described in sec. 3.5 with a precision of about $\pm$ 0.5 ns, since the deuteron momentum is used to calculate the $\sqrt{s}$ variable. The easiest way to study the effect of possible FW detector time offsets on the total *pn* energy (or $d\pi^+\pi^-$ invariant mass) is to apply similar offsets to the simulated model.

For this purpose, the ABC resonance model has been again used, and offsets were added to the deuteron time of flight. The deuteron momentum was then recalculated

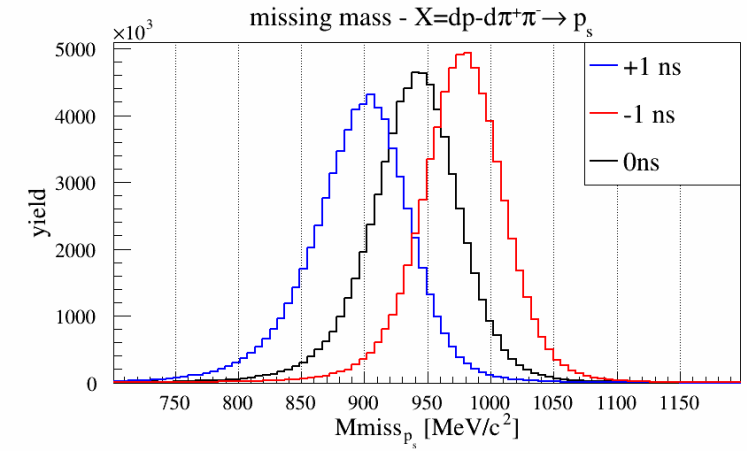

Figure 4.11: difference in $\sqrt{s}$

based on this changed time. The applied time offsets were equal to $+1ns$ and $-1ns$. The results of these tests are presented below. First, figure 4.11 shows the $d\pi^+\pi^-$ missing mass (i.e. mass of the missing particle in the $dp \to d\pi^+\pi^- X$ reaction) following different time offsets. This plot shows that these time manipulations have a significant effect on this missing mass, which in the case of a perfect calibration is peaked at the proton mass (see the histogram labeled 0 ns). This confirms the good sensitivity of the FW calibration method based on the missing mass (see Sec. 3.5). However, the influence on the total energy of the system is very small, as shown in fig. 4.12, where the difference in $\sqrt{s}$ induced by the time modifications are plotted. As one can see, for most events, the $\Delta T = 1$ ns case, which is larger than our uncertainty by a factor 2, corresponds to an error on the total energy $\Delta\sqrt{s}$ smaller than a few MeV/c^2. The effect on the $\sqrt{s}$ distribution, after the deconvolution procedure is not significant, as shown in fig. 4.13.

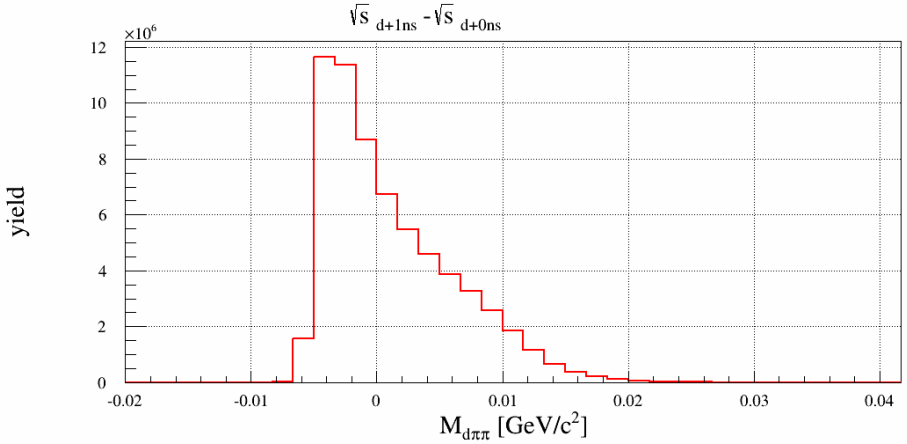

Figure 4.12: difference in $\sqrt{s}$ (reconstructed as a $d\pi^+\pi^-$ invariant mass) induced by a time off-set of +1ns on the FW time-of-flight.

4.2.5 Two-pion invariant mass distribution

Next, the $M_{\pi\pi}$ invariant mass distributions are studied for both experimental situations (deuteron detected in HADES or in FW).

First, on Fig. 4.14, the total $\pi^+\pi^-$ invariant mass distribution, corresponding to the deuterons detected in HADES is presented. As previously, black points correspond to

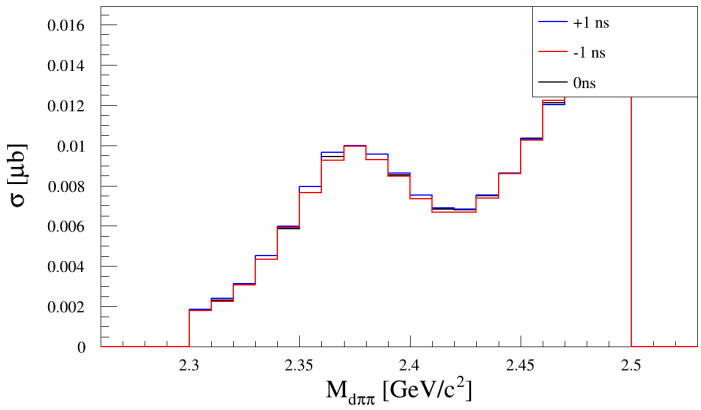

Figure 4.13: Comparison of $\sqrt{s}$ distributions after the unfolding procedure for different off-sets of the FW time-of-flight

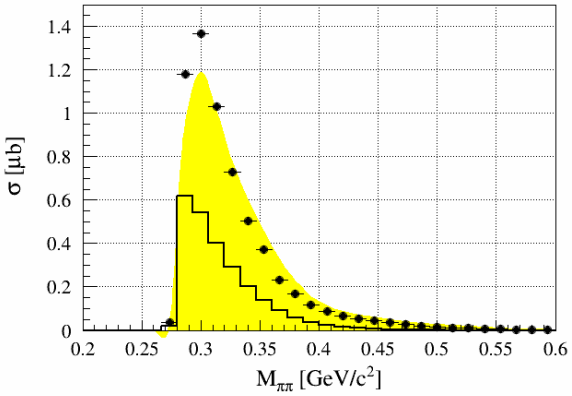

Figure 4.14: Total $\pi\pi$ invariant mass distribution from quasi-free np reaction. Black points represents experimental data, solid black line shows ABC resonance model and yellow area is a $dp \rightarrow d\pi^+\pi^- p_{spectator}$ phase-space simulation. Results corresponds to the case with deuteron detected at high θ_d inside HADES. Data are corrected for efficiency and presented in units of cross section

the experimental data, black solid line shows ABC resonance model and the yellow area stands for the phase-space simulation. Due to the acceptance of HADES and the reaction kinematics, deuterons detected at such high polar angles needed to reach the HADEs detector (i.e. about 15° are associated with di-pions with low invariant mass (see fig. 4.4). This is very clear for the simulated events, which show a peak-like structure just at the kinematical limit. The experimental distribution is a bit broader, and is in better agreement with the phase space distribution.

The next picture (Fig. 4.15) shows the two-pion invariant mass for three different slices in the total center of mass energy of the pn system. The top picture corresponds to an energy bin located on the left side of resonance, the bottom left corresponds to the region where the d^* peak is situated and the bottom right picture is obtained for an energy bin in the right side, where the simulated model completely underestimates the data (see left part of fig. 4.9). In all three slices, the ABC model is peaked at too small values, while the phase-space simulation agrees very well with experiment, except for the first one, where an enhancement at large $\pi^+\pi^-$ is observed. The origin of this contribution was not investigated in this work, it represents anyway a very small fraction of the events.

The total two-pion invariant mass distribution is shown on figure 4.14, for the case

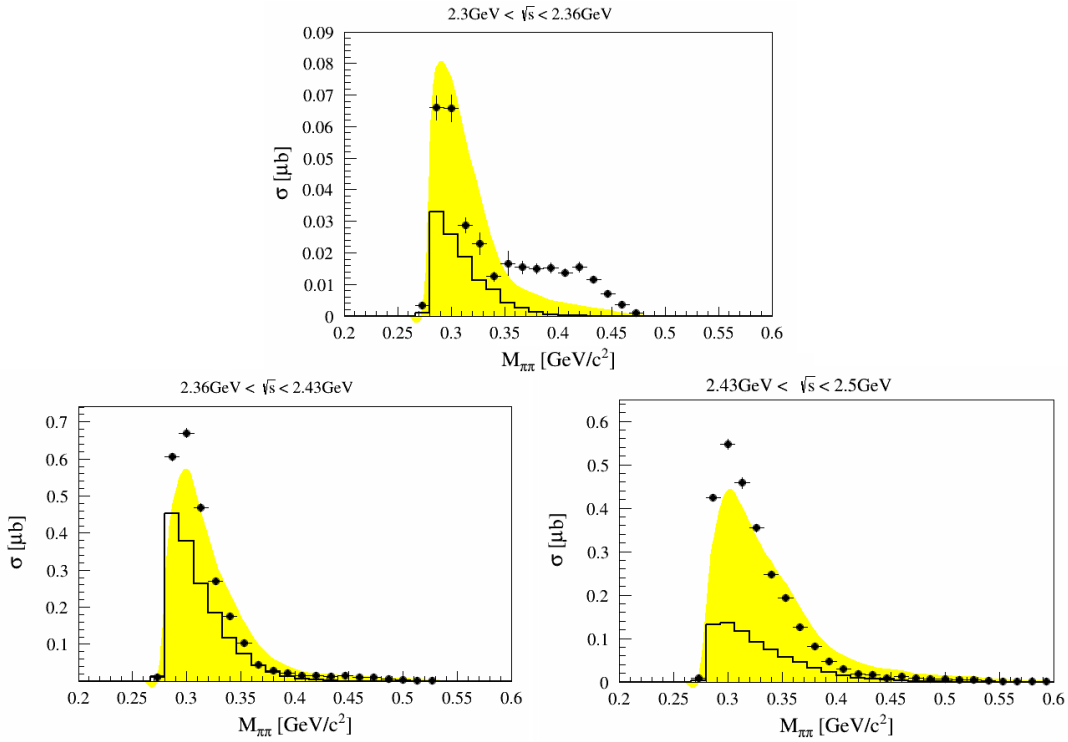

Figure 4.15: Two-pion invariant mass distribution from quasi-free np reaction as a function for three different bins in $\sqrt{s}$ in the scenario with deuteron detected at high θ_d inside HADES.

when deuteron is emitted at low angles and detected in Forward-Wall. The simulated channels and data points are represented in the same way as above. These spectra are very different from the case of deuteron detected in HADES. Indeed, when the deuteron is emitted at forward angles, the small $\pi^+\pi^-$ invariant masses are suppressed (see fig. 4.4), in contrast to the case when it is detected in HADES. This means that the detection of the deuteron in FW is also not very favorable to investigate the possible contribution of the dibaryon resonance, since the latter is expected to produce a dipion pair with small invariant mass.

However, one can still look at the comparison of the data with the simulations using the ABC resonance model. The yields are rather well reproduced by this model. However, the theoretical distribution and the phase space distributions as well, are shifted towards the smallest invariant masses.

This can be seen in more details in Fig.4.15, where the distributions are shown for three different bins in $\sqrt{s}$. The shift between the theoretical and measured $\pi^+\pi^-$ invariant mass distributions can be seen for the three bins, but is larger for the two first bins, which are in the region of the resonance. The description could probably be improved by a better adjustment of vertex form factors, since the latter are controlling the four-momentum transfer between the baryonic resonance and the nucleon or the dibaryonic resonance and the deuteron, which directly influences the $\pi^+\pi^-$ invariant mass.

4.3 Conclusion on dipion analysis

The reaction quasi-free $np \to d\pi^+\pi^-$ was studied for two different experimental situations: in the first case, the deuteron is detected in HADES and in the second case, it is detected in the FW detector. The two cases correspond to two very different kinemati-

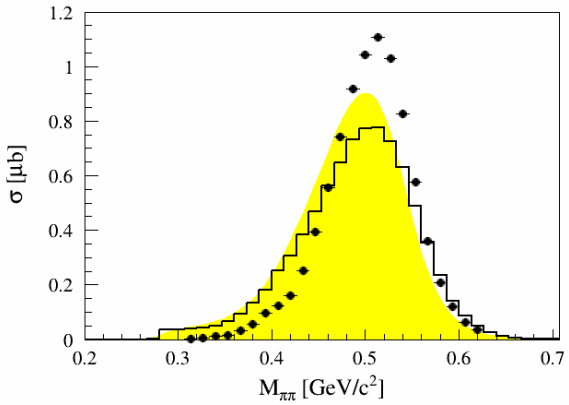

Figure 4.16: Total $\pi\pi$ invariant mass distribution from quasi-free np reaction for the scenario with deuteron detected at forward θ_d angles in Forward-Wall detector. The black points represent experimental data, solid black line shows ABC resonance model and yellow area is the $dp \rightarrow d\pi^+\pi^- p_{spectator}$ phase-space simulation.

cal situations, corresponding respectively to deuterium angles larger than 15° and smaller than 7°. None of this case is very well adapted for the investigation of the possible dibaryon resonance, which is supposed to contribute at the smallest $\pi^+\pi^-$ invariant masses. When the deuterium is detected in the FW, i.e. at small angles, the contribution of the smallest invariant masses is suppressed. The detection at large angles, in the HADES detector is in principle more favourable, but it is at the limit of the kinematically allowed region, which is very sensitive to small distortions, in particular with respect to the quasi-free model.

The signal for the reaction quasi-free $np \rightarrow d\pi^+\pi^-$ could be extracted in both cases as a function of $\pi^+\pi^-$ invariant mass and $d\pi^+\pi^-$ invariant masses. In the quasi-free picture, the latter observable stands for the pn pair energy. The experimental spectra are compared to the ABC model predictions of [49], which includes conventional t-channel processes (double $\Delta(1232)$, N(1440), N(1520) excitations), as well as a more exotic dibaryon contribution. The latter is based on the observation of the WASA collaboration. The model underestimates the yield measured in the case of the deuteron detected in HADES. As mentioned above, this region is too close to the kinematical limit for the quasi-free reaction to draw conclusions. The model gives a reasonable description of the data when the deuteron is detected in the FW. In particular, the yields are well reproduced, which can be taken as a success of the model. However, the experimental $\pi^+\pi^-$ invariant mass distributions are shifted towards higher values with respect to the model, which calls for some refinement of the description of the different processes.

A procedure was used to unfold the neutron momentum distribution and extract the quasi-free $np \rightarrow d\pi^+\pi^-$ cross section. Due to the experimental effects, the extracted observable cannot be directly used as a cross section. The procedure could be improved in future works by extracting the pn cross sections from an iterative process based on simulations. However, the present method can be used to compare the data to the model predictions. Following this procedure, a peak is observed in our experimental data, very similar to the one predicted by the ABC model, even though peaked at a pn center of mass energy slightly lower than the one corresponding to the WASA dibaryon. However, further investigations are needed in order to understand the origin of the peak. The effect of the calibration of the FW detector was investigated and found to be small. However, other effects, like the sensitivity to small deviations from the participant-spectator model might play a role.

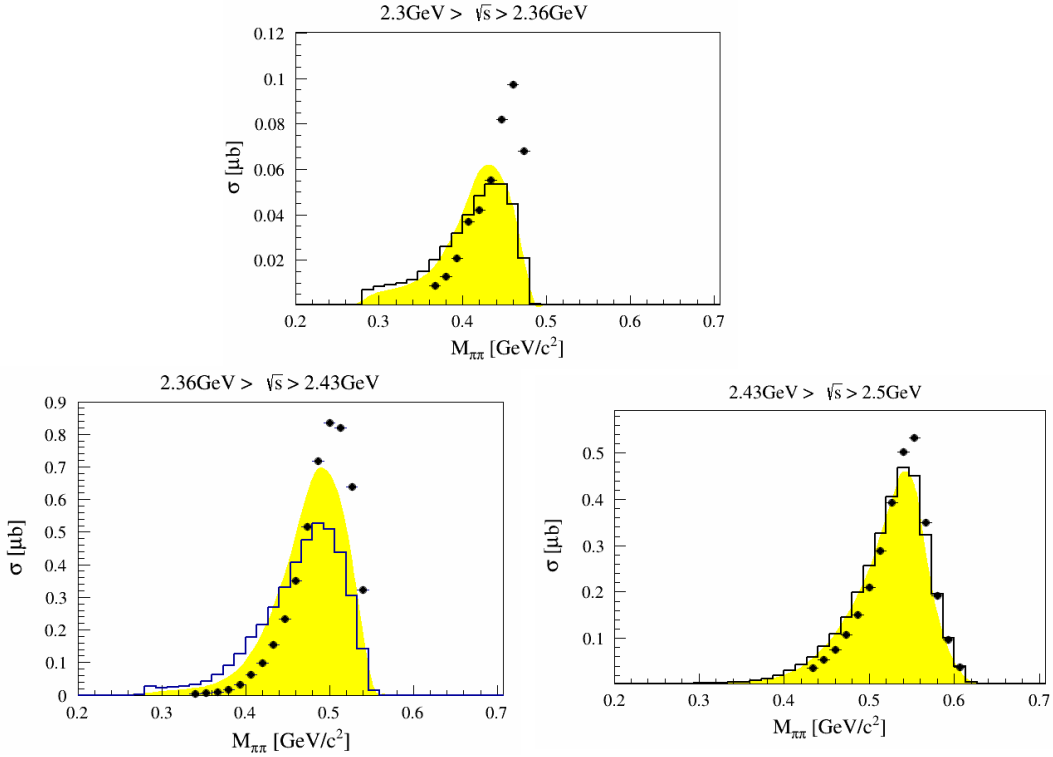

Figure 4.17: Two-pion invariant mass distribution from quasi-free np reaction for three different bins in $\sqrt{s}$. Scenario with deuteron detected at forward θ_d angles in Forward-Wall detector.

Chapter 5

Results for the dilepton production

In this chapter, the results from the analysis of the exclusive quasi-free $np \to de^+e^-$ channel are presented. As discussed in more details in Sec.1.4, it is important to estimate the contribution of this channel to the inclusive $pn \to e^+e^-X$ reaction, due to the unexplained excess of the yield at high dielectron invariant masses, in comparison with the pp reaction. In particular, such an exclusive analysis allows to check the predictions of the model of [53].

This work can be considered as a complement to the studies on inclusive dilepton production from quasi-free np reaction with HADES [16, 10] as well as the studies of the $np \to npe^+e^-$ investigated in another PhD thesis from the HADES collaboration [54].

We first introduce the ingredients of the simulation, which is used to compare to the data. We first present results obtained with the condition of one charged particle measured in FW, in addition to the spectator proton, corresponding either to the quasi-free $pn \to pe^+e^-$ reaction , or to the quasi-free $pn \to de^+e^-$ reaction, then we exploit the coplanarity condition, which was introduced in Sec. 3.4.2, to extract an upper limit for the $pn \to de^+e^-$ channel cross section.

5.1 Simulation inputs for the dilepton production and acceptance effects

5.1.1 simulation inputs

In the analysis of the quasi-free $np \to de^+e^-$ channel, a very important aspect of the simulation is the treatment of the background channels, with a unbound pn pair in the exit channel. This is due to the very small yield of the de^+e^- and the difficulty to identify the deuterons, as explained in sec.3.4.

The different channels which have been considered are listed in Table 5.1. The simulation inputs have already been discussed in details in ref. [54] and are summarized below.

As can be seen from this list, the simulation takes into account the contribution from channels with a spectator neutron. In pratice, their contribution is negligible, due to the "spectator" condition (see Sec. 3.4.1). The dominant dielectron channel is the π^0 meson Dalitz decay ($\pi^0 \to e^+e^-\gamma$). π^0s can be produced in two ways: either directly in nucleon-nucleon collisions or by the decay of baryonic resonances, but the production mode of the $\pi 0$ does not influence much the e^+e^- yield. In the present simulation, the π^0s are simulated exlusively via the $\Delta(1232)$ decay, which is by far the dominant contribution (processes 1-3 in Table 5.1).

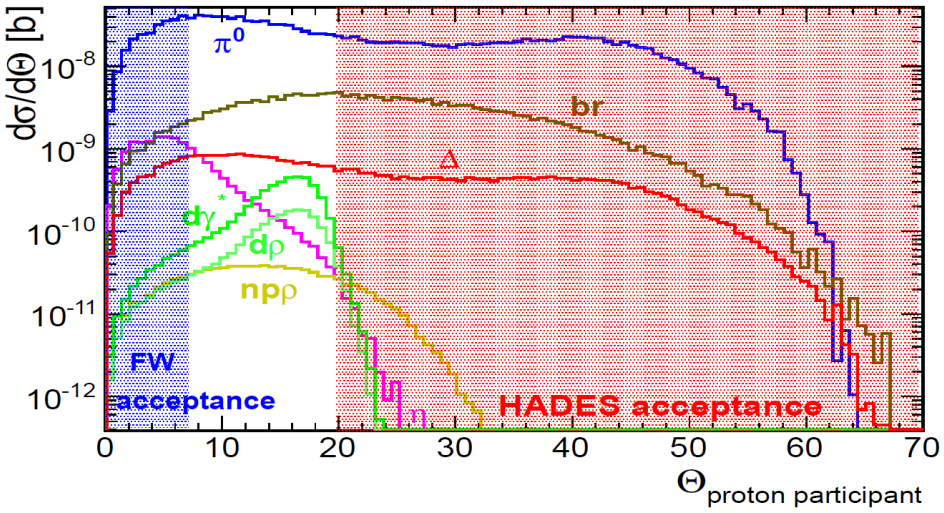

Figure 5.1: Polar angle distribution of the proton participating in the reaction for the main simulated channels listed in Table 5.1. The blue line corresponds to all channels with a π^0 Dalitz decay (processes 1-3), the brown line corresponds to the OBE model (process 10), the red line to the $\Delta(1232)$ Dalitz decay (processes 4-6) , the pink line to the η Dalitz decay contribution (processes 7-9), the dark green to the dγ^* channel with VDM form factor (process 14) and the light green to the ρ production via N(1520) (process 11-13). Blue and red regions represent the Forward Wall and the HADES acceptance region. [54]

For the treatment of the $\Delta(1232)$ Dalitz decay of baryonic resonances, two different models have been used in [54]. The first one is based on the OBE model [21], where resonant (corresponding to $\Delta(1232)$ excitation) and non-resonant contributions were added coherently (process 10). In the second one, only the $\Delta(1232)$ Dalitz decay ($\Delta \rightarrow Ne^+e^-$) is considered (processes 4-6). The case of the N(1520) resonance is treated via an off-shell ρ production, as explained later. The Dalitz decay of other baryonic resonances is negligible.

Another important source, which should be included is the η meson. Since the kinetic beam energy $E_k = 1.25$ AGeV is below η threshold, this source can only contribute in quasi-free np reaction by additional energy gained from the motion of the nucleons inside the deuteron nucleous. As it is known from former experiments, the η production proceeds mainly via the excitation of $N(1535)$ which subsequently decays into the nucleon-η channel. The cross sections for the respective channels $np \rightarrow d\eta$, $np \rightarrow np\eta$ are known from WASA measurements - H. Calen [68] work and COSY11 [69] (processes 7-9).

In the simulation cocktail, a "sub-threshold" ρ production is also included. This is performed, in two steps, via decay of the $N(1520)$ (N(1520)$\rightarrow \rho N \rightarrow e^+e^-N$). Here, the $dp \rightarrow d\rho$ channel has been introduced using the same differential cross sections as for the pp$\rightarrow ppp$ (and $pn \rightarrow pn\rho$ as well). The difference in the cross-sections for the $dp \rightarrow d\rho + p_{spec} \rightarrow de^+e^-p_{spec}$ (process number 13) and $dp \rightarrow pn\rho + p_{spec} \rightarrow pne^+e^-p_{spec}$ (process number 11) or $dp \rightarrow pp\rho + n_{spec} \rightarrow ppe^+e^-n_{spec}$ (process number 12) is just due to the different phase-spaces.

As already mentioned, the aim of this work is to test the predictions of [53] for the $dp \rightarrow de^+e^-$. This channel, which has been included as process number 14, can also be considered as a "ρ-like" process, due to the VMD form factor, used in the model.

lp.	channel	cr. sect.	br. ratio
1.	$d\,p \Rightarrow\ p_{sp}\,n\,\Delta^+ \ \Rightarrow\ p_{sp}\,n\,p\,\pi^0 \ \rightarrow\ p_{sp}\,n\,p\,\gamma\,e^+\,e^-$	$3.67mb$ [70]	0.012
2.	$d\,p \Rightarrow\ p_{sp}\,p\,\Delta^0 \ \Rightarrow\ p_{sp}\,p\,n\,\pi^0 \ \rightarrow\ p_{sp}\,p\,n\,\gamma\,e^+\,e^-$	$3.67mb$ [70]	0.012
3.	$d\,p \Rightarrow\ n_{sp}\,p\,\Delta^+ \ \Rightarrow\ n_{sp}\,p\,p\,\pi^0 \ \rightarrow\ n_{sp}\,n\,p\,\gamma\,e^+\,e^-$	$3.67mb$ [70]	0.012
4.	$d\,p \Rightarrow\ p_{sp}\,p\,\Delta^0 \ \rightarrow\ p_{sp}\,p\,n\,e^+\,e^-$	$5.54mb$ [70]	$4.82 \cdot 10^{-5}$
5.	$d\,p \Rightarrow\ p_{sp}\,n\,\Delta^+ \ \rightarrow\ p_{sp}\,n\,p\,e^+\,e^-$	$5.54mb$ [70]	$4.93 \cdot 10^{-5}$
6.	$d\,p \Rightarrow\ n_{sp}\,p\,\Delta^+ \ \rightarrow\ n_{sp}\,p\,p\,e^+\,e^-$	$5.54mb$ [70]	$4.94 \cdot 10^{-5}$
7.	$d\,p \Rightarrow\ p_{sp}\,n\,p\,\eta \ \rightarrow\ p_{sp}\,n\,p\,\gamma\,e^+\,e^-$	$13.4\mu b$ [68]	$5.96 \cdot 10^{-3}$
8.	$d\,p \Rightarrow\ p_{sp}\,d\,\eta \ \rightarrow\ p_{sp}\,d\,\gamma\,e^+\,e^-$	$22.8\mu b$ [68]	$6.10 \cdot 10^{-3}$
9.	$d\,p \Rightarrow\ n_{sp}\,p\,p\,\eta \ \rightarrow\ n_{sp}\,p\,p\,\gamma\,e^+\,e^-$	$2.41\mu b$ [68]	$5.64 \cdot 10^{-3}$
10.	$d\,p \Rightarrow\ p_{sp}\,n\,p\,e^+\,e^-$	$1.48\mu b$ [21]	1
11.	$d\,p \Rightarrow\ p_{sp}\,p\,N^0(1520) \Rightarrow\ p_{sp}\,p\,n\,\rho \ \rightarrow\ p_{sp}\,p\,n\,e^+\,e^-$	$8.91\mu b$ [71]	$8.12 \cdot 10^{-4}$
12.	$d\,p \Rightarrow\ n_{sp}\,p\,N^+(1520) \Rightarrow\ n_{sp}\,p\,p\,\rho \ \rightarrow\ n_{sp}\,p\,p\,e^+\,e^-$	$8.91\mu b$ [71]	$8.12 \cdot 10^{-4}$
13.	$d\,p \Rightarrow\ p_{sp}\,d\,\rho \ \rightarrow\ p_{sp}\,d\,e^+\,e^-$	$6.40\mu b$ [71]	$8.12 \cdot 10^{-4}$
14.	$d\,p \Rightarrow\ p_{sp}\,d\,\gamma^* \ \Rightarrow\ p_{sp}\,d\,e^+\,e^-$	$41.7nb$ [53]	1

Table 5.1: List of channels included in the simulation. The cross sections correspond to the first step of the reaction (meson or baryonic resonance production) and are taken from the references mentioned in brackets. The third column indicates the branching ratio to the e^+e^- channel.

5.1.2 acceptance effects

The angular distributions of protons or deuterons emitted in the main simulated channels are shown in fig. 5.1. It confirms that, as already mentionned in Sec.3.2, the channels with deuteron in final state, which are interesting for this work, have a very small contribution inside HADES acceptance. Therefore, in our analysis, the deuterons are identified in the Forward-Wall hodoscope.

Asking for the detection of a particle in the FW detector, the contribution of reaction channels with a deuteron in the final state is strongly enhanced, however, its contribution is still much smaller than for channels with an unbound pn pair.

One can also notice that the condition of detection of the charged particle in FW enhances the η and ρ contributions.

5.2 Results for the quasi-free $np \rightarrow p/d\ e^+e^-$ reaction

We start the study of the dilepton exclusive channels by looking at events with two hits detected in the FW detector. Using this simple condition, there is no possibility to distinguish deuterons from protons and one therefore selects events corresponding both to the $np \rightarrow pe^+e^-$ and to $np \rightarrow de^+e^-$ channels.

• The e^+e^- invariant mass spectra obtained for such events are displayed in Fig. 5.2 after correction for efficiency and normalization, as described in Secs. 3.7 and 3.6, respectively. The experimental data are compared with the results of the simulation described in Sec. 5.1. Here, the calculation uses the resonance model for the $\Delta(1232)$ Dalitz decay and the dγ^* model for the channel with d in final state. However, the off-shell ρ contribution following the N(1520) excitation is also shown for comparison.

The π^0 region is perfectly well described, but the simulation fails to reproduce the intermediate invariant mass region $0.12GeV/c^2 < M_{ee} < 0.5GeV/c^2$. This effect has been studied in detail in [54], in particular by analyzing the kinematics of the missing particle.

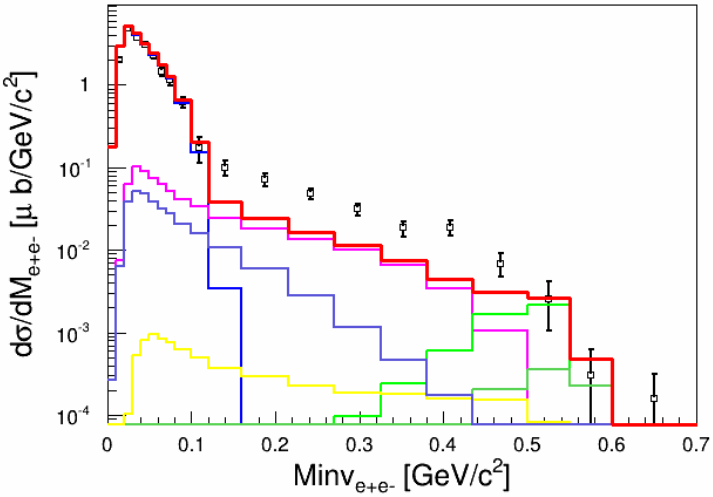

Figure 5.2: Invariant mass distribution of e^+e^- from quasi-free np reaction, obtained for events with two hits in FW, where the first hit is a proton spectator and the second hit is a emitted p or d. Black points show experimental results. The thick red solid line is the sum of all simulated channels, i.e. π^0 Dalitz decay (processes 1-3 in Table 5.1, , the dark blue line), $\Delta(1232)$ Dalitz decay (processes 4-6, pink line), $np\rho$ contribution (processes 11-12, yellow line), η meson Dalitz decay (processes 7-9,light blue line), $d\gamma^*$ contribution (process 14, light green line). The $d\rho$ contribution (process 13, dark green line) is also shown for comparison. Data are presented inside HADES acceptance and are corrected for the efficiency. Data normalized to the pp elastic scattering.

The conclusion was that the dilepton excess could not be due to a higher η or off-shell ρ production (channels 11-13), but had rather to be attributed to the $\Delta(1232)$ Dalitz decay. More precisely, the data were favoring the description by the resonance model rather the one based on the OBE model [21], including the non-resonant cross-section.

Another result of this exclusive analysis is that the channels with a deuterium in final state can not be responsible for the excess in the intermediate mass region, since these contributions are peaked for M_{ee} around 0.55 GeV/c^2. This shape is different from the one obtained in simulations of the inclusive dilepton production in the same process (see fig. 1.17). This is due to the condition of detection of the deuteron in FW wall, which suppresses the smallest e^+e^- invariant masses, for which the deuterium angular distribution is broader. This kinematical effect is very similar to the one observed for the two-pion channel (see Fig. 4.7).

The channels with a deuterium in final state are important, since, as can be seen respectively for the inclusive and exclusive dilepton production in Fig. 1.17 and Fig. 5.2, they can improve the description of the data at the highest invariant masses. It can be observed in Fig. 5.2 that the experimental yield in this region clearly favors the dγ^* model with respect to the model based on the N(1520) excitation. However, due to the limitation of this analysis, the experimental yield in the high invariant mass region cannot be unambiguously attributed to the quasi-free $np \rightarrow de^+e^-$. In the next step, we will try to suppress the contribution of these channels, considered as a background, and extract an upper limit for the cross-section of the channel with a deuteron in final state.

5.3 Study of the quasi-free $np \to de^+e^-$ reaction

5.3.1 Extraction of an upper limit for the cross section

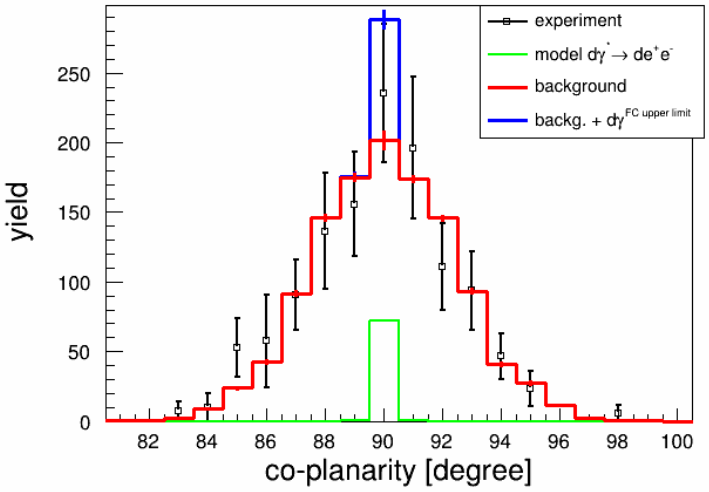

Figure 5.3: Co-planarity distribution for events with two hits in the FW with a time difference larger than 5 ns. Experimental data are represented by black points; The red solid line shows the result of the simulation of all $dp \to npe^+e^- + p_{spec}$ channels, also including $npe^+e^-\gamma$ from eta meson decay; the green line shows the $d\gamma^*$ contribution predicted by B.V. Martemyanov [53]; the blue line shows the experimental upper limit estimated using the Feldman-Cousins method [72].

To suppress the contribution of events with an unbound pn pair in the exit channel, we use a similar procedure as in the case of $\pi^+\pi^-$ production, as discused in Sec. 3.4.2.

First, a lower limit of 5 ns on the time difference between the two hits has been applied. In addition, one can use the fact that in the reaction $dp \to pde^+e^-$, the plane defined by the momenta of the incident deuteron and of the e^+e^- systems should be the same as the one defined by the momenta of the spectator proton and deuteron detected in FW.

The distribution of coplanarity angle, as defined in Eq **??** is displayed in fig. 5.3 for events with two hits in FW wall with time difference larger than 5 ns. *Explain how the errors have been calculated* Here, only events with an e^+e^- invariant mass larger than 0.25 GeV/c^2 are considered, since the contribution of events with deuterium in final state is expected only at high invariant masses. No clear structure appears around 90°, in contrast with the case of dipion production where a prominent narrow peak could be seen (see Fig. 3.18). However, this distribution can still be used to extract an upper limit for the cross section of the $np \to de^+e^-$ reaction.

One of the approaches for an upper limit determination was described by G. Feldman and R. Cousins [72]. It is a method for small signal statistical analysis. This method has been originally developed in 1997 for analysis of experiments searching for neutrino oscillations.

The Feldman & Cousins method requires a precise background description. In our case, this background is due to the reactions with an unbound pn pair in the exit channel. As discussed in Sec. 5.2, the simulation of such channels fails in experimental yield reproduction in the region of e^+e^- invariant masses below 0.4 GeV/c^2, where our signal (i.e. channels with a deuteron in final state) is expected to have a negligible contribution (see Fig. 5.2). However, the simulation of the "background" channels nicely describes the

shape of the coplanarity distribution. This is checked in fig. 5.3, where the distribution corresponding to the simulation of the background channels was scaled to reproduce the experimental yield in the region where no signal is expected, i.e. for coplanarity angles smaller than 89° or larger than 90°. The small contribution of the dilepton production from the channels dp→ $pnp\eta$ (processes 7 and 9) was also taken into account. This simulation was therefore used for the background description in the Feldman & Cousins method.

In practice, an upper limit for the signal events is therefore extracted using the experimental yield and its error integrated for coplanarity angles between 89° and 91°. The number of background events was taken from the simulated yield in this region, normalized as described above.

The result for this upper limit is 88 counts on the 90% confidence level. This estimate can be cross checked by summing the yield from the simulated background and the extracted signal, as shown in fig. 5.3. The result is contained within the error bars associated to the experimental data. The sum of the scaled background and signal is indeed around 290 counts, in agreement with the upper limit of the experimental yield.
The experimental upper limit on the signal is compatible with the 73 counts deduced from the simulation of the dγ^* channel (radiative capture model) which are also displayed in Fig. 5.3, as a green line.

After normalizing the experimental yields using the *pp* elastic scattering, as described in Sec. 3.6, one gets an upper limit for the quasi-free $np \rightarrow de^+e^-$ of 0.33 nb measured in the HADES acceptance, while the corresponding cross section is σ=0.28 nb in the radiative capture model. The upper limit on the cross section in 4π can only be obtained using a model dependent extrapolation. From the simulations with the radiative capture model, one can deduce an acceptance factor $\epsilon = 6.7\ 10^{-3}$. Using this factor to correct the experimental yields, one deduces an upper limit for the quasi-free $np \rightarrow de^+e^-$ of 49 nb in 4π, to be compared with the theoretical prediction of 41.7 nb.

5.3.2 Investigation of the invariant mass spectra

The procedure to extract the upper limit on the total cross section described above, has been applied in each bin of e^+e^- invariant mass. First, events with the simple condition of two hits in the FW have been considered. The extracted upper limit is shown as a function of the e^+e^- invariant mass, as a blue histograms in the left part of Fig. 5.4 in comparison with the total experimental yield (black open dots) which were already shown in fig. 5.2. This experimental upper limit is very close to the prediction from the radiative capture model, which is shown in the picture as a dash-dotted line.

In a second step, the procedure was applied to events with a time difference between the two hits in FW larger than 5 ns, and a coplanarity angle between 89° and 91°, in order to suppress the contribution from events with an unbound *pn* pair. The results are shown in the right part of fig. 5.4. It can be observed, by comparing the simulated yield for the dγ^* channel to the total simulated yield in both parts of fig. 5.4, that the additionnal conditions indeed reduce efficiently the contribution of background channels, without affecting the yield of the signal. The results of the extraction of the upper limit are also displayed. They are again in very good agreement with the radiative capture model.

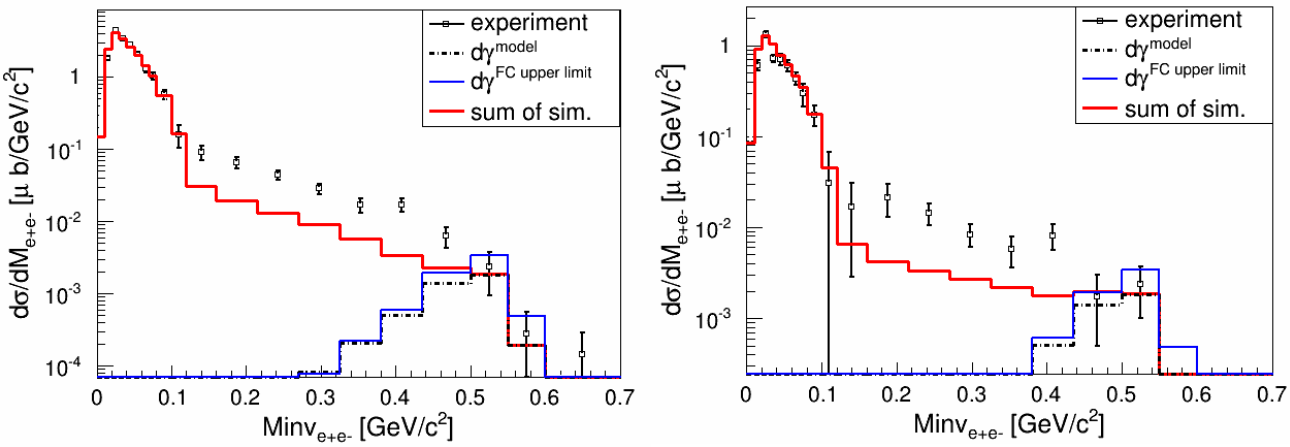

Figure 5.4: Exclusive di-electron invariant mass from quasi-free np collisions. Left panel: General condition for two charged hadrons in FWall detector. The first hit is a proton spectator and the second hit is an emitted proton or deuteron. Right panel: A lower limit of 5 ns on the time difference between the two hits and a co-planarity condition $90° \pm 1°$ has been applied. Both panels present results of the upper limit calculations for the de^+e^- decay channel (blue solid line). The red line shows the sum of all simulated channels, as described in the text. Black points show experimental data inside HADES acceptance, normalized to the pp elastic scattering.

5.4 Di-lepton yield linked with di-pion production

Recently, a connection between the production of $\pi^+\pi^-$ pairs in ρ channel (i.e. isospin 1) and e^+e^- pairs has been pointed out by M. Bashkanov and H. Clement [52]. As discussed in chap.1.3 and in chap.4, the double Δ contribution plays a major role in the double pion production in pp or pn collisions. The t-channel double Δ excitation is known since a long time, but recently a s-channel production via an intermediate dibaryon resonance has been advocated. The analysis of two-pion production in the quasi-free $pn \to d\pi^+\pi^-$ shown in the previous chapter is compatible with this interpretation, although it is not able to confirm it unambiguously.

The double Δ production in the t-channel is taken into account for the e^+e^- production in resonance models [17], as a contribution to the $\Delta(1232)$ and π^0 Dalitz decays, in addition to the one coming from a single $\Delta(1232)$ and single π^0 production. There are two completely new aspects in the approach by Bashkanov and Clement. The first one is the dilepton production by $\Delta\Delta$ Final State Interaction (Fig. 1.15), which proceeds via an off-shell $\pi^+\pi^- \to \rho \to e^+e^-$ process. The second aspect is to consider the double Δ production with the intermediate s-channel d* resonance (bottom part of fig. 1.15).

As explained in more details in Sec. 1.4, in the case of pp, the two pions can be produced only in isospin 0, which excludes the annihilation into a ρ meson. This is why this process is an interesting candidate for explaining the excess of dielectrom yield observed in np reaction in comparison with pp.

M. Bashkanov and H. Clement have compared their model to the inclusive e^+e^- production in the quasi-free np reaction (see fig. 1.16) and have shown that a significant improvement of the description of the dilepton spectra could be achieved. Our goal here is to check the predictions for the exclusive channels that were analyzed in this PHD work.

In addition, we tried to introduce a modification in the model. Indeed, in the original model, the $\pi^+\pi^- \to \rho \to e^+e^-$ process is described using Eq.1.3, which holds for on-shell pions. This reflects as a cut of the e^+e^- invariant mass spectrum at the two pion mass,

which is clearly visible in fig. 1.16. However, in the dielectron production process, the pions might well be off-shell and the region of low invariant masses should be populated. The shape of the dilepton invariant mass spectrum is very sensitive to this off-shell production. This is shown for example, in the simulation of the $np \to NN(1520) \to np\rho \to npe^+e^-$ channel (see yellow line in fig. 5.2). We expect such a shape to be closer to a realistic dilepton spectrum from the process $np \to \Delta(1232)\Delta(1232) \to pn\rho \to pne^+e^-$. As a very crude attempt to treat this problem, we therefore used the shape of the simulated e^+e^- invariant mass spectrum for the N(1520) channel in our simulation and scaled it by the theoretical cross section for the $np \to np\rho$ process from [52] (210 μb, as given in Sec. 1.4).

The situation is very similar for the $np \to d\rho$ channel and in this case, we used the shape of the simulated $d\gamma^*$ channel and the cross section for dρ production from Bashknaov model (100 μb), as well as the branching ratio of 8.1 10^{-4}, which is related to the specific shape of the dilepton spectrum.

Such contributions have then been used in our simulation for the $np \to np\rho$ and $np \to d\gamma^*$, in replacement to the previous inputs. The predictions of this new simulation are compared to the results of the analysis of the exclusive e^+e^- analysis in fig. 5.5. The left side of the figure corresponds to the selection of two hits in FW. In comparison to fig. 5.4, a significant improvement in the description of the intermediate mass region ($0.2 < M_{ee} < 0.5 GeV/c^2$) can be observed. This is due to the much larger cross section for the $np \to npe^+e^-$ cross section in the Bashkanov model (81 nb instead of 42 nb). The cross section for the $np \to d\gamma^*$ process is also increased (100 μb instead of 51 μb), which results in this case in a worse description of the high invariant mass region, which was well described using the radiative capture model. The cross section for the $np \to npe^+e^-$ process in Bashkanov's model is indeed larger by 60% than the experimental upper limit that we estimated to be 49 nb (see Sec. 5.3.1).

These effects are studied in more details when additional conditions on the time difference between the two hits in FW and on the coplanarity are applied (see Sec.5.3.1) to suppress the channels with an unbound pn pair (right part of fig. 5.5). Again, the improvement for the intermediate mass region can be observed by comparing to the right part of fig. 5.4. The excess in the high invariant mass region, due to the too large $np \to d\rho$ cross section can be observed as well.

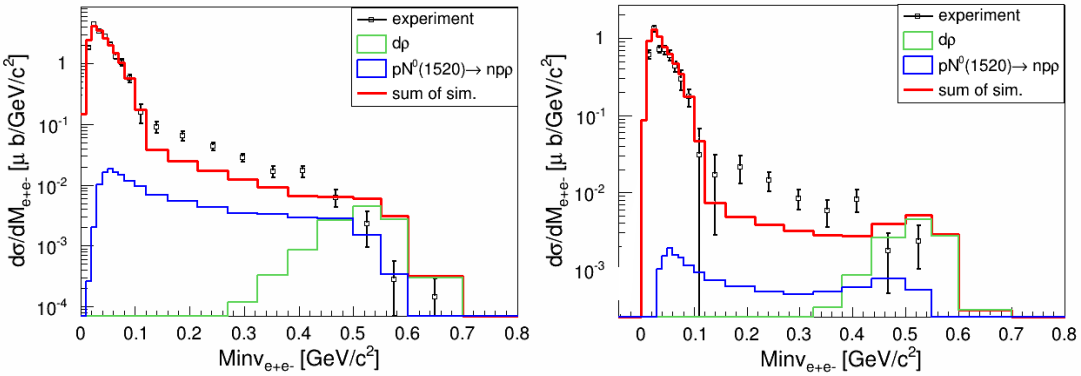

Figure 5.5: The data (black points) are the same in both panels as in fig.5.4. The simulations use the cross section of the $pn \to np\rho$ and $pn \to d\rho$ channels from [52] but a different dielectron shape (see text).

It has to be mentioned that, in [52], the cross sections are calculated at a fixed $T_k = 1.25 GeV$ neutron energy. However, as was shown for the dipion analysis, it might be important to take into account the dependence of the cross section as a function of the pn

center of mass energy for processes involving the d^* resonance. This should be the subject of future work.

Another open issue is the contribution of the direct electromagnetic decay of the d* resonance. The process $pn \to d^* \to [np]_{I=0}e^+e^-$ or $pn \to d^* \to de^+e^-$ could indeed be a non-negligible source of dileptons, but the branching ratio of this process, which is related to the electromagnetic structure of this object is completely unknown. In addition, this decay should be treated coherently with the $d \to \Delta\Delta \to npe^+e^-$ process.

5.5 Conclusion on dilepton analysis

In this chapter, we have analysed exclusive dielectron production channels of the quasi-free pn reaction at an average neutron energy of 1.25 GeV. The goal was to study the $np \to de^+e^-$ reaction. The suppression of the other channels was done in two steps. First a selection of two hits in the FW wall was applied, then a lower limit on the time difference and a coplanarity condition were applied. We have shown that these conditions reduce the contribution of channels with a unbound pn pair. However, the remaining background is too large and only an upper limit for the $np \to de^+e^-$ reaction cross section could be extracted. This upper limit was studied, as a function of the invariant mass. The results have been compared to simulations to test the theoretical predictions of [53]. The extracted upper limit is compatible with the predictions of this model.

We also compared our data to the model of [52] which includes a significant dilepton yield from an intermediate double Δ excitation leading either to a unbound pn pair or to a deuteron. This model is very interesting for our study, since it connects the two-pion and dielectron production. The double Delta excitation is indeed both a source of dipion and dielectron. In addition, one of the channels involves the dibaryon resonance, which is also seen in our dipion analysis.

We first modified the model to take into account the off-shell pion annihilation into a ρ meson. With this new simulation, the dilepton yield in the intermediate mass region, which is related to the processes with an unbound pn pair is closer to the data, but the yield for channels with emission of a deuteron exceeds by a factor 2 our experimental upper limit for these channels. Further refinements to this model would be necessary, like the consideration of the neutron momentum in the deuterium. In addition, it would be needed to consider the direct electromagnetic decay of the d* resonance, which is related to its electromagnetic structure. This can be done only in a full model where all the channels would be considered in a coherent way.

Chapter 6

Summary

In this thesis, the exclusive di-pion and di-electron production channels in quasi-free $n + p$ interactions at about $E_k = 1.25GeV/u$ were presented. First the exclusive $d\pi^+\pi^-$ channel and new deuteron selection method named coplanarity have been discussed. Next, applying this new procedure to the existing inclusive e^+e^- results, the exclusive de^+e^- channel has been investigated.

In general, analysis of the channels with deuteron in final state with HADES spectrometer are technical challenge due to d angular distributions. Presented results are divided to the two scenarios: in the first case, the deuteron is detected in HADES and in the second case, it is detected in the FW detector. The two cases correspond to two very different kinematical situations, corresponding respectively to deuteron angles larger than 15° and smaller than 7°. In case of the deuteron detected inside HADES tracking system, the reaction phase-space is very limited however the data quality is very good. On the other hand, in case of detecting deuteron in Forward Wall detector the count rates are much bigger but the event selection requires much bigger effort and accuired data have much worse quality.

The main goal of the quasi-free $np \to d\pi^+\pi^-$ exclusive channel studies was to complement the studies of the $\pi^+\pi^-$ production processes (i.e. double $\Delta(1232)$, N(1440), N(1520) excitations) which are performed with $np \to np\pi^+\pi^-$ and $pp \to pp\pi^+\pi^-$ analysis within HADES collaboration. Furthermore, recent WASA collaboration results [73, 49] indicated a big enhancement in $\pi\pi$ yield due to new di-baryon resonance. The HADES results in details described in sec. 4, indeed shows that conventional sources fail to reproduce both the $\pi\pi$ yield and the shape of the spectra within HADES acceptance. Our results are consistent with the WASA observations. On the other hand, presented results are not sensitive enough to give a satisfying proof for the di-baryon resonance existence. However, the differential spectra provided by our experiment could motivate theoretical studies. Fully consistent theoretical calculation of the quasi-free $pn \to d\pi^+\pi^-$ are indeed missing.

As the last part of this thesis, the analysis of the exclusive $np \to de^+e^-$ channel has been presented. This work should be treated as a continuation of the still unresolved e^+e^- production enhancement in $n+p$ over $p+p$ collisions. To fully explain this issue, specially dedicated analysis of the $np \to npe^+e^-$ exclusive channel have been started and are topic of separate PhD thesis. However using new techniques, based on kinematical constraints developed during two-pion analysis, allowed the exclusive de^+e^- analysis. Obtained results (presented in sec. 5) allowed to check proposed by B.V. Martemyanov [53] model concerning the $d\gamma^*$ contribution. Using the Feldman-Cousins method the upper limit for such a process have been estimated in sec. 5.3.1. On the other hand, the HADES data has been compared to the model of [52] which includes a significant dilepton yield from

an intermediate double Δ excitation. This model is very interesting for our study, since it connects the two-pion and dielectron production. The double Delta excitation is indeed both a source of dipion and dielectron. In addition, one of the channels involves the di-baryon resonance, which is consistent with the di-pion analysis.

Obtained results puts more constraints on the theoretical calculations and suggests further refinements to models in both di-electron and di-pion analysis.

Bibliography

[1] P. Koch, *Low mass lepton pair production and pion dynamics in ultrarelativistic heavy ion collisions*, *Z.Phys.* **C57** (1993) 283–304.

[2] Y. Nambu and G. Jona-Lasinio, *Dynamical model of elementary particles based on an analogy with superconductivity. ii*, *Phys. Rev.* **124** (Oct, 1961) 246–254.

[3] S. Klimt, M. Lutz and W. Weise, *Chiral phase transition in the su(3) nambu and jona-lasinio model*, *Physics Letters B* **249** (1990), no. 3–4 386 – 390.

[4] S. Leupold, V. Metag and U. Mosel, *Hadrons in strongly interacting matter*, *Int.J.Mod.Phys.* **E19** (2010) 147–224 [0907.2388].

[5] K. Nakamura and P. D. Group, *Review of particle physics*, *Journal of Physics G: Nuclear and Particle Physics* **37** (2010), no. 7A 075021.

[6] J. Sakurai, *Theory of strong interactions*, *Annals Phys.* **11** (1960) 1–48.

[7] F. V. Murphy and D. Yount, *PHOTONS AS HADRONS*, *Sci.Am.* **224** (1971) 93.

[8] M. Harada and K. Yamawaki, *Wilsonian matching of effective field theory with underlying QCD*, *Phys.Rev.* **D64** (2001) 014023 [hep-ph/0009163].

[9] L. Barkov, A. Chilingarov, S. Eidelman, B. Khazin, M. Y. Lelchuk *et al.*, *Electromagnetic Pion Form-Factor in the Timelike Region*, *Nucl.Phys.* **B256** (1985) 365–384.

[10] T. Galatyuk, *Di-electron spectroscopy in HADES and CBM : from $p+p$ and $n+p$ collisions at GSI to $Au+Au$ collisions at FAIR*. PhD thesis, Johann Wolfgang Goethe-Universität, Frankfurt am Main, 2009.

[11] G. E. Brown and M. Rho, *Scaling effective lagrangians in a dense medium*, *Phys. Rev. Lett.* **66** (May, 1991) 2720–2723.

[12] R. Rapp and J. Wambach, *Chiral symmetry restoration and dileptons in relativistic heavy ion collisions*, *Adv.Nucl.Phys.* **25** (2000) 1 [hep-ph/9909229].

[13] **HADES** Collaboration, G. Agakichiev *et al.*, *The High-Acceptance Dielectron Spectrometer HADES*, *Eur. Phys. J.* **A41** (2009) 243 [nucl-ex/0902.3478].

[14] **HADES Collaboration** Collaboration, P. Salabura *et al.*, *Hades experiments: investigation of hadron in-medium properties*, *J.Phys.Conf.Ser.* **420** (2013) 012013.

[15] **HADES Collaboration** Collaboration, G. Agakishiev *et al.*, *Inclusive dielectron production in proton-proton collisions at 2.2 GeV beam energy*, *Phys.Rev.* **C85** (2012) 054005 [1203.2549].

[16] **HADES** Collaboration, G. Agakichiev and others, *Origin of the low-mass electron pair excess in light nucleus-nucleus collisions*, *Phys. Lett.* **B690** (2010) 118.

[17] J. Weil, H. van Hees and U. Mosel, *Dilepton production in proton-induced reactions at SIS energies with the GiBUU transport model*, *Eur.Phys.J.* **A48** (2012) 111 [1203.3557].

[18] K. Schmidt, E. Santini, S. Vogel, C. Sturm, M. Bleicher *et al.*, *Production and evolution path of dileptons at energies accessible to the HADES detector*, *Phys.Rev.* **C79** (2009) 064908 [0811.4073].

[19] A. Faessler, C. Fuchs, M. Krivoruchenko and B. Martemyanov, *Vector meson angular distributions in proton-proton collisions*, *Phys.Rev.* **C70** (2004) 035211 [nucl-th/0407075].

[20] **DLS Collaboration** Collaboration, W. Wilson *et al.*, *Inclusive dielectron cross-sections in p + p and p + d interactions at beam energies from 1.04-GeV to 4.88-GeV*, *Phys.Rev.* **C57** (1998) 1865–1878 [nucl-ex/9708002].

[21] L. P. Kaptari and B. Kämpfer, *Di-electron bremsstrahlung in intermediate-energy p n and d p collisions*, *Nucl. Phys.* **A764** (2006) 338 [nucl-th/0504072].

[22] R. Shyam and U. Mosel, *Dilepton production in proton-proton and quasifree proton-neutron reactions at 1.25 GeV*, *Phys. Rev.* **C82** (2010) 062201 [hep-ph/1006.3873].

[23] Q. Wan and F. Iachello, *A unified description of baryon electromagnetic form factors*, *Int.J.Mod.Phys.* **A20** (2005) 1846–1849.

[24] **HADES Collaboration** Collaboration, G. Agakishiev *et al.*, *Study of dielectron production in C+C collisions at 1-A-GeV*, *Phys.Lett.* **B663** (2008) 43–48 [0711.4281].

[25] **HADES** Collaboration, G. Agakishiev *et al.*, *Dielectron production in Ar+KCl collisions at 1.76A GeV*, *Phys. Rev.* **C84** (2011) 014902 [nucl-ex/1103.0876].

[26] **TAPS Collaboration** Collaboration, R. Averbeck *et al.*, *Production of pi0 and eta mesons in carbon-induced relativistic heavy ion collisions*, *Z.Phys.* **A359** (1997) 65–73.

[27] W. Cassing and E. Bratkovskaya, *Hadronic and electromagnetic probes of hot and dense nuclear matter*, *Phys.Rept.* **308** (1999) 65–233.

[28] **HADES Collaboration** Collaboration, G. Agakishiev *et al.*, *Study of exclusive one-pion and one-eta production using hadron and dielectron channels in pp reactions at kinetic beam energies of 1.25 GeV and 2.2 GeV with HADES*, *Eur.Phys.J.* **A48** (2012) 74 [1203.1333].

[29] **HADES** Collaboration, A. Kurilkin *et al.*, *Double pion production in np and pp collisions at 1.25 GeV with HADES*, *PoS* **Baldin-ISHEPP-XXI** (2012) 041.

[30] G. Agakishiev, A. Balanda, D. Belver, A. Belyaev, J. Berger-Chen *et al.*, *Baryon resonance production and dielectron decays in proton-proton collisions at 3.5 GeV*, *Eur.Phys.J.* **A50** (2014) 82 [1403.3054].

[31] J. Johanson, R. Bilger, W. Brodowski, H. Calen, H. Clement *et al.*, *Two-pion production in proton proton collisions near threshold*, *Nucl.Phys.* **A712** (2002) 75–94.

[32] **COSY-TOF Collaboration** Collaboration, S. Abd El-Bary *et al.*, *Two-Pion Production in Proton-Proton Collisions with Polarized Beam*, *Eur.Phys.J.* **A37** (2008) 267–277 [0806.3870].

[33] T. Tsuboyama, F. Sai, N. Katayama, T. Kishida and S. S. Yamamoto, *Double-pion production induced by deuteron-proton collisions in the incident deuteron momentum range 2.1-3.8 GeV/c*, *Phys.Rev.* **C62** (2000) 034001.

[34] **WASA-at-COSY Collaboration** Collaboration, P. Adlarson *et al.*, *Measurement of the $pn \to pp\pi^0\pi^-$ reaction in search for the recently observed resonance structure in $d\pi^0\pi^0$ and $d\pi^+\pi^-$ systems*, *Phys.Rev.* **C88** (2013), no. 5 055208 [1306.5130].

[35] **WASA-at-COSY Collaboration** Collaboration, P. Adlarson *et al.*, *Measurement of the $np \to np\pi^0\pi^0$ Reaction in Search for the Recently Observed $d^*(2380)$ Resonance*, 1409.2659.

[36] L. Alvarez-Ruso, E. Oset and E. Hernandez, *Theoretical study of the N N → N N pi pi reaction*, *Nucl. Phys.* **A633** (1998) 519 [nucl-th/9706046].

[37] X. Cao, B.-S. Zou and H.-S. Xu, *Phenomenological analysis of the double pion production in nucleon-nucleon collisions up to 2.2 GeV*, *Phys. Rev.* **C81** (2010) 065201 [nucl-th/1004.0140].

[38] T. Skorodko, M. Bashkanov, D. Bogoslawsky, H. Calen, H. Clement *et al.*, *$\Delta\Delta$ Excitation in Proton-Proton Induced $\pi^0\pi^0$ Production*, *Phys. Lett.* **B695** (2011) 115 [nucl-ex/1007.0405].

[39] A. Jerusalimov, *Analysis of the Reaction: $np \to np\pi^+\pi^-$ from the Point of View of Oper-Model*, nucl-th/1203.3330.

[40] N. E. Booth, A. Abashian and K. M. Crowe, *Anomaly in Meson Production in p+d Collisions*, *Phys.Rev.Lett.* **7** (1961) 35–39.

[41] J. Hall, T. Murray and L. Riddiford, *Evidence for a low-energy S wave pi pi interaction and a possible doubly charged dibaryon enhancement*, *Nucl.Phys.* **B12** (1969) 573–585.

[42] J. Banaigs, J. Berger, J. Duflo, L. Goldzahl, M. Cottereau *et al.*, *Observation of the abc effect and of a structure at 450 mev in mesonic missing-mass spectra. (in french)*, *Nucl.Phys.* **B28** (1971) 509–527.

[43] J. Banaigs, J. Berger, L. Goldzahl, T. Risser, L. Vu-Hai *et al.*, **abc* and *def* effects in the reaction d p → he3 (mm)0 - position, width, isospin, angular and energy distributions*, *Nucl.Phys.* **B67** (1973) 1–36.

[44] F. Plouin, J. Duflo, L. Goldzahl, G. Bizard, F. Bonthonneau *et al.*, *Observation of the ABC Effect in the Reaction n p → d (Mm) 0 with a 1.88GeV/c Neutron Beam*, *Nucl.Phys.* **A302** (1978) 413–422.

[45] J. Banaigs, J. Berger, M. Cottereau, F. Fabbri, L. Goldzahl *et al.*, *Production of I = 0 Mesonic States in the Reaction d d → He4 x*, *Nucl.Phys.* **B105** (1976) 52.

[46] T. Risser and M. Shuster, *Anomalous enhancements in multiple-pion production with deuterons*, *Phys.Lett.* **B43** (1973) 68–72.

[47] M. Bashkanov, *Double Pionic Fusion: Towards an Understanding of the ABC Puzzle by Exclusive Measurements*. PhD thesis, Eberhard-Karls Universittät ,Tübingen, 2006.

[48] O. Khakimova, *The ABC Effect in the Double-Pionic Fusion to Deuterium*. PhD thesis, Eberhard-Karls Universittät ,Tübingen.

[49] **WASA-at-COSY Collaboration** Collaboration, P. Adlarson *et al.*, *ABC Effect in Basic Double-Pionic Fusion — Observation of a new resonance?*, *Phys.Rev.Lett.* **106** (2011) 242302 [1104.0123].

[50] Pricking, A., Bashkanov, M., Clement, H., Doroshkevich, E., Perez del Rio, E., Skorodko, T. and Wagner, G. J., *Abc effect in double-pionic fusion – a new resonance?*, *EPJ Web of Conferences* **37** (2012) 01024.

[51] **WASA-AT-COSY Collaboration** Collaboration, P. Adlarson *et al.*, *Isospin Decomposition of the Basic Double-Pionic Fusion in the Region of the ABC Effect*, *Phys.Lett.* **B721** (2013) 229–236 [1212.2881].

[52] M. Bashkanov and H. Clement, *On a Possible Explanation of the DLS Puzzle*, *Eur.Phys.J.* **A50** (2014) 107 [1312.2810].

[53] B. Martemyanov, M. Krivoruchenko and A. Faessler, *Dilepton production in pp and np collisions at 1.25 GeV*, *Phys. Rev.* **C84** (2011) 047601 [nucl-th/1108.4265].

[54] R. Trebacz, *Investigation of dielectron production in quasi-free pn scattering at 1.25GeV with HADES*. PhD thesis, Jagiellonian University, Cracow, 2012.

[55] T. Bretz, *Magnetfeldeigenschaften des Spektrometers HADES*. PhD thesis, Technische Universität München, Germany, 1999.

[56] J. Markert, *Untersuchung zum Ansprechverhalten der Vieldraht-Driftkammern niedriger Massenbelegung des HADES-Experiments*. PhD thesis, Institut für Kernphysik, Goethe-Universität Frankfurt, Germany, 2005.

[57] M. Sanchez, *Momentum reconstruction and pion production analysis in the HADES spectrometer at GSI*. PhD thesis, University of Santiago de Compostela, 2003.

[58] I. Antcheva, M. Ballintijn, B. Bellenot, M. Biskup, R. Brun *et al.*, *ROOT: A C++ framework for petabyte data storage, statistical analysis and visualization*, *Comput.Phys.Commun.* **182** (2011) 1384–1385.

[59] I. Frohlich, L. Cazon, T. Galatyuk, V. Hejny, R. Holzmann *et al.*, *Pluto: A Monte Carlo Simulation Tool for Hadronic Physics*, *PoS* **ACAT2007** (2007) 076 [0708.2382].

[60] I. Frohlich, T. Galatyuk, R. Holzmann, J. Markert, B. Ramstein *et al.*, *Design of the Pluto Event Generator*, *J.Phys.Conf.Ser.* **219** (2010) 032039 [0905.2568].

[61] "Geant3 detector description and simulation tool." CERN long writeup W5013, 1993.

[62] H. Wind, *Momentum analysis by using a quintic spline model for the track*, *Nuclear Instruments and Methods* **115** (1974), no. 2 431 – 434.

[63] P. W. H. Vetterling William T., Flannery Brian P. and T. S. A., *Numerical Recipes, 3rd Edition*. Cambridge University Press, 2007.

[64] *Study of spectator tagging in the reaction $np \to pp\pi$ with a deuteron beam*, *The European Physical Journal A - Hadrons and Nuclei* **29** (2006), no. 3 353–361.

[65] D. A. et al., *A precision measurement of pp elastic scattering cross sections at intermediate energies*, *Eur. Phys. J.* **A22** (2004) 125–148.

[66] L. Alvarez-Ruso, *The role of the Roper resonance in $np \to d\pi^0\pi^0$*, *Phys.Lett.* **B452** (1999) 207–213 [nucl-th/9811058].

[67] R. Machleidt, *The High precision, charge dependent Bonn nucleon-nucleon potential (CD-Bonn)*, *Phys.Rev.* **C63** (2001) 024001 [nucl-th/0006014].

[68] H. Calen, J. Dyring, K. Fransson, L. Gustafsson, S. Haeggstroem *et al.*, *Measurement of the quasifree $p + n \to p + n + eta$ reaction near threshold*, *Phys.Rev.* **C58** (1998) 2667–2670.

[69] P. Moskal, R. Czyzykiewicz, H.-H. Adam, S. Bass, A. Budzanowski *et al.*, *Near threshold production of the eta meson via the quasi-free $pn \to pneta$ reaction*, *Phys.Rev.* **C79** (2009) 015208 [0807.0722].

[70] S. Teis *et al.*, *Pion-production in heavy-ion collisions at SIS energies*, *Z. Phys.* **A356** (1997) 421.

[71] D. R. O. M. V. Flaminio, W. G. Moorhead and N. Rivoire, *Compilation of cross sections iii: p and $\overline{p}$ induced reactions*, .

[72] G. J. Feldman and R. D. Cousins, *Unified approach to the classical statistical analysis of small signals*, *Phys. Rev. D* **57** (Apr, 1998) 3873–3889.

[73] M. Bashkanov, C. Bargholtz, M. Berlowski, D. Bogoslawsky, H. Calen *et al.*, *Double-Pionic Fusion of Nuclear Systems and the ABC Effect: Aproaching a Puzzle by Exclusive and Kinematically Complete Measurements*, *Phys. Rev. Lett.* **102** (2009) 052301 [nucl-ex/0806.4942].